Investigation of Static Interfacial Fracture in Orthotropic-Orthotropic Composite Bimaterials Using Photoelasticity

---

A Dissertation
Presented to
the Faculty of the Graduate School
University of Missouri

In Partial Fulfillment
of the Requirements for the Degree

Doctor of Philosophy

---

by

MARIUS DANIEL ELLINGSEN

Dr. Sanjeev K. Khanna, Dissertation Supervisor

JULY 2009

The undersigned, appointed by the dean of the Graduate School, have examined the dissertation entitled

INVESTIGATION OF STATIC INTERFACIAL FRACTURE IN ORTHOTROPIC-ORTHOTROPIC COMPOSITE BIMATERIALS USING PHOTOELASTICITY

presented by Marius Daniel Ellingsen,

a candidate for the degree of Doctor of Philosophy,

and hereby certify that, in their opinion, it is worthy of acceptance.

Professor Sanjeev K. Khanna

Professor Sherif El-Gizawy

Professor R. Andrew Winholtz

Professor Vellore S. Gopalaratnam

Professor Carmen Chicone

ACKNOWLEDGEMENTS

First and foremost, I want to thank Dr. Sanjeev K. Khanna for offering me several great opportunities. Dr. Khanna first approached me in 1999 about doing an M.Sc. under his supervision. I was then finishing my B.Sc. and was glad to accept his offer. Since then I have remained in graduate school under his supervision, first transferring with him to the University of Missouri to finish my M.Sc., and then moving on to a Doctorate. Under his tutelage I have developed a large set of experimental and theoretical skills. I also received extensive training and developed good experience with nanoindentation and atomic force microscopy, an opportunity that very few people ever get.

Next, I am thankful for the unending support from my parents and siblings. They always encouraged me. I have been away from them for a very long time, but they were always there for me with love, kindness, and moral and financial support.

The technical staff at the Engineering School always provided invaluable help, insights, and practical training. Brian Samuels taught me how to use the milling machine and the lathe, and taught me every useful trick of the trade that would help me machine my specimens. O.S. “Rex” Gish was another source of advice, help, and technical insights. Rich Oberto, Mike Klote, and Mike Absheer have also helped in a great many ways.

Finally, I want to thank my friends, too numerous to name, for being there for me. It was of immeasurable benefit to have someone to talk to when nothing seemed like it was going to work, and to then receive their encouragement and support.

TABLE OF CONTENTS

Investigation of Static Interfacial Fracture in Orthotropic-Orthotropic Composite Bimaterials Using Photoelasticity i
ACKNOWLEDGEMENTS ii
TABLE OF CONTENTS iii
LIST OF FIGURES vi
LIST OF TABLES ix
ABSTRACT x

1 INTRODUCTION 1

1.1 Problem Statement 1

1.2 Literature Review - Theoretical Work 3
1.2.1 Analytical Approaches 3
1.2.2 Numerical Methods and Simulations 9

1.3 Literature Review - Experimental work 13
1.3.1 Specimen Types 13
1.3.2 Experimental Work 13
1.3.3 Ancillary Experimental Methods 16

1.4 Literature Review – Summary 18

2 EXPERIMENTAL METHODS 20

2.1 A Word about Units 20

2.2 Photoelasticity 21

2.3 The Circular Polariscope 26
2.3.1 Working Principle of the Circular Polariscope 26
2.3.2 The Circular Polariscope and Digital Imaging System 31

2.4 Specimen Configurations 36
2.4.1 Specimen Configurations Used 36

2.5 The Transparent Composite Material 45
2.5.1 Specifications 45
2.5.2 Fabrication Technique 47
2.5.3 Fiber Volume Fraction of the Composite Material 49
2.5.4 Photoelastic Properties of the Composite Material 50

2.6 Mechanical Properties of the Composite Material 62
2.6.1 Young's Modulus 62
2.6.2 Shear modulus 65

2.7 Fabricating the Bimaterial Specimens 67

3 ANALYTICAL METHODS 74

3.1 General Methodology 74

3.2 Data Acquisition 75

3.3 Fringe Multiplication 77

3.4 Stress Field and Stress-Optic Law 82

3.5 Overdeterministic Analysis 90
3.5.1 Determining the Stress-Intensity Factors 90
3.5.2 Fringe Regeneration 92

4 RESULTS AND DISCUSSION 98

4.1 Mode-I Fracture (Horizontal Interface) 98
4.1.1 Fracture Surface Topographic Examination of Horizontal Interface Bimaterial Specimens ... 114

4.2 Mixed-Mode Fracture (Angled Interface) 117
4.2.1 Fringe Asymmetries 121
4.2.2 Angled Interface Specimen Tests and Results 123
4.2.3 Discussion of Numerical Results 155
4.2.4 Discussion of False-Color Fringe Multiplication Results 157
4.2.5 Fracture Surface Topographic Examination of Angled Interface Bimaterial Specimens 158

5 CONCLUSIONS 164

6 FUTURE WORK 166

6.1 Dynamic Fracture 166

6.2 Airy Stress Function – Westergaard Facture Analysis 167

6.3 Sensitivities, Annular Regions, and Interactions 168

6.4 Automated Fringe Data Collection and Fringe Comparison 169

REFERENCES 171

APPENDIX A 180
Maple Code for Overdeterministic Analysis and Fringe Regeneration, Single Analysis Run 180

APPENDIX B 193
Maple Code for Overdeterministic Analysis and Fringe Regeneration, Multiple Analysis Run (Stepping Through Grid Surrounding Crack Tip) 193

APPENDIX C 207
MathCad Worksheet for False-Color Fringe Multiplication 207

APPENDIX D 211

Machining Parameters and Practical Tips for Machining The Transparent Composite 211

VITA 212

LIST OF FIGURES

Figure 2.2.1 Stress and Index Ellipsoids 23
Figure 2.3.1 A Stressed Model in the Circular Polariscope 27
Figure 2.3.2 Isochromatic Fringes Surrounding the Crack Tips in an Orthotropic-Orthotropic Bimaterial with Horizontal Interface 30
Figure 2.3.3 Polariscope, Loading Frame, and Digital Imaging System 33
Figure 2.3.4 Homalite-100 Disc Under Compression in a Vise, Seen in Normal Light 34
Figure 2.3.5 Homalite-100 Disc in Compression in Dark-Field Circular Polariscope 35
Figure 2.4.1 Specimen Configurations 37
Figure 2.4.2 Orthotropic-Orthotropic Horizontal Interface Bimaterial Specimen under Load 38
Figure 2.4.3 Orthotropic-Orthotropic Angled Interface Bimaterial under Load 38
Figure 2.4.4 Definitions of Specimen Dimensions 39
Figure 2.4.5 Absolute vs. Relative Crack Length 40
Figure 2.4.6 Schematic of Double-Cantilever Beam Interface Specimen 42
Figure 2.4.7 Schematic of Brazilian Disc Specimen 43
Figure 2.4.8 Composite-Composite Brazilian Disc Specimen Under 0.7 kN (160 lb) Compressive Load in Polariscope. Fringes Emanating from Loading Points even at this Very Low Load 43
Figure 2.4.9 Schematic of Four-Point Bend Specimen 44
Figure 2.4.10 Composite-Composite Four-Point Bend Specimen Under 5.8 kN (1300 lb) Load in Polariscope 44
Figure 2.5.1 Author Partially Seen Through Composite Used in Investigation. 46
Figure 2.5.2 Mold for Making Composite Material 48
Figure 2.5.3 Specimens for Determining Composite Properties, in SI and US Customary Units 51
Figure 2.5.4 Machining Jig for "Dogbone" Composite Specimens 52
Figure 2.5.5 Tube and Mask Arrangement for Photoelastic Property Tests 54
Figure 2.5.6 Intensity vs. Load for 0/90 Degree Reinforcement Angle Tensile Specimen 56
Figure 2.5.7 Load vs. Fringe Order for 0/90 Degree Reinforcement Angle Tensile Specimen 58
Figure 2.5.8 Intensity vs. Load for +/- 45 Degree Reinforcement Angle Tensile Specimen 60
Figure 2.5.9 Load vs. Fringe Order for +/- 45 Degree Reinforcement Angle Specimen 60
Figure 2.6.1 Stress vs. Strain Plot for 0/90 Degree Composite Tensile Specimen 64
Figure 2.6.2 Shear Stress vs. Shear Strain Plot for Composite 66
Figure 2.7.1 Silane-Treated Bimaterial Halves Hanging to Dry 69
Figure 2.7.2 Preparatory Wrapping of Bimaterial Halves 70
Figure 2.7.3 Aluminum Bimaterial Half with Mating Surface Partially Covered with Teflon 71
Figure 2.7.4 Principle Sketch of Bimaterial Mating Setup 72
Figure 2.7.5 Photograph of Actual Bimaterial Mating Setup 73
Figure 3.2.1 Data Points Collected from Annular Region Surrounding Crack Tip (First Quadrant) 76
Figure 3.2.2 Specification of Bimaterial Quadrants 76
Figure 3.3.1 False-Color Fringe Multiplication of Isochromatic Fringes in 0º/90º Composite - 0º/90º Composite Bimaterial with Interface Angle 45º, Load 2.7 kN (600 lb), a/w =0.33, w = 127 mm (5 in.) 80
Figure 3.5.1 Effect of Increasing the Number of Terms in Stress-Field Equations 94
Figure 3.5.2 Effect of Incorrectly Locating Crack Tip 97
Figure 4.1.1 Aluminum –30°/60° Composite Bimaterial, 2 kN (450 lb) Load, a/w = 0.33, w = 76 mm (3.0 in) 99
Figure 4.1.2 0°/90° Composite - 0°/90° Composite Bimaterial, 2.7 kN (600 lb) Load, a/w = 0.17, w = 76 mm (3.0 in) 100
Figure 4.1.3 0°/90° Composite - 0°/90° Composite Bimaterial, 2.7 kN (600 lb) Load, a/w = 0.25, w = 76 mm (3.0 in) 101
Figure 4.1.4 0°/90° Composite - 0°/90° Composite Bimaterial, 2.7 kN (600 lb) Load, a/w = 0.33, w = 76 mm (3.0 in) 102
Figure 4.1.5 0°/90° Composite - 0°/90° Composite Bimaterial, 2.7 kN (600 lb) Load, a/w = 0.5, w = 121 mm (4.75 in) 103

Figure 4.1.6 0°/90° Composite - 15°/75° Composite Bimaterial, 2.7 kN (600 lb) Load, a/w = 0.33, w = 76 mm (3.0 in)....104
Figure 4.1.7 0°/90° Composite - 30°/60° Composite Bimaterial, 2.7 kN (600 lb) Load, a/w = 0.33, w = 76 mm (3.0 in)....105
Figure 4.1.8 0°/90° Composite - 45°/45° Composite Bimaterial, 3.3 kN (750 lb) Load, a/w = 0.33, w = 152 mm (6.0 in)....106
Figure 4.1.9 Energy Release Rate G vs. a/w for Specimens with Reinforcement Directions 0°/90° in Both Halves. Values are averaged for all four....107
Figure 4.1.10 Energy Release Rate vs. Reinforcement Angle for Bimaterial Specimens with Varying Reinforcement Angle in One Half, a/w = 0.33....108
Figure 4.1.11 Mode Mixity vs. a/w Ratio for Specimens with Reinforcement Directions 0°/90° in Both Halves....109
Figure 4.1.12 Mode mixity vs. Reinforcement Angle in Bimaterial Specimens with an Angled Half 110
Figure 4.1.13 Fracture Surface (Viewing Fracture Surface Head-On) of 0º/90º Bimaterial Half at 50x Magnification....115
Figure 4.1.14 Fracture Surface (Viewing Fracture Surface Head-On) of 30º/60º Bimaterial Half at 50x Magnification....116
Figure 4.2.1 Fringe Pattern Progression in Specimen with Interface Angle 30°, 0°/90° Composite - 0°/90° Composite Bimaterial, a/w = 0.33, w = 127 mm (5 in.)....119
Figure 4.2.2 Annular Regions, Fringe Orders, and Data Points Taken from Specimen with Interface Angle 45°, 0°/90° Composite - ±45° Composite Bimaterial, a/w = 0.33, w = 127 mm (5 in.)under 4.0 kN (900 lb) load....120
Figure 4.2.3 Asymmetric Development of Fringes Across Interface....122
Figure 4.2.4 Interface Angle 15°, 0°/90° Composite - 0°/90° Composite Bimaterial, 2.7 kN (600 lb) Load, a/w = 0.33, w = 76 mm (3.0 in), Annular Region ID = 1t, OD = 3t (The only specimen to have OD = 3t)....124
Figure 4.2.5 Annular Regions and Regenerated Fringe Patterns for Specimen Shown in Figure 4.2.4 125
Figure 4.2.6 Interface Angle 30º, 0°/90° Composite - 0°/90° Composite Bimaterial, 4kN (900 lb) load, a/w = 0.33, w = 127 mm (5 in.)....127
Figure 4.2.7 False-Color Fringe Multiplied Image of Specimen Shown in Figure 4.2.6....128
Figure 4.2.8 Annular Regions and Regenerated Fringe Patterns for Specimen Shown in Figure 4.2.6 129
Figure 4.2.9 Interface Angle 45°, 0°/90° Composite - 0°/90° Composite Bimaterial, 2.7kN (600 lb) load, a/w = 0.33, w = 127 mm (5 in.)....131
Figure 4.2.10 Annular Regions and Regenerated Fringe Patterns for Specimen Shown in Figure 4.2.9 132
Figure 4.2.11 Discussion of Fringe Patterns in Figure 4.2.9....133
Figure 4.2.12 Interface Angle 45°, 15°/75° Composite - 0°/90° Composite Bimaterial, 4kN (900 lb) load, a/w = 0.33, w = 127 mm (5 in.)....135
Figure 4.2.13 Annular Regions and Regenerated Fringe Patterns for Specimen Shown in Figure 4.2.12....136
Figure 4.2.14 Interface Angle 45°, 0°/90° Composite - 30°/60° Composite Bimaterial, 4kN (900 lb) load, a/w = 0.33, w = 127 mm (5 in.)....138
Figure 4.2.15 Annular Regions and Regenerated Fringe Patterns for Specimen Shown in Figure 4.2.14....139
Figure 4.2.16 Interface Angle 45°, ±45° Composite - 0°/90° Composite Bimaterial, 4kN (900 lb) load, a/w = 0.33, w = 127 mm (5 in.)....141
Figure 4.2.17 Identification of Fringe Orders, Data Points Taken, from Quadrant 2 and 3 from Specimen in Figure 4.2.16....142
Figure 4.2.18 False-Color Fringe Multiplied Version of Figure 4.2.16....143
Figure 4.2.19 Identification of Fractional Fringe Orders, and Data Points, in Quadrant 2 of the False-Color Fringe Multiplied Specimen in Figure 4.2.16....144
Figure 4.2.20 Annular Regions and Regenerated Fringe Patterns for Specimen Shown in Figure 4.2.16....145

Figure 4.2.21 Interface Angle 45°, 0°/90° Composite – Aluminum Bimaterial, 4kN (900 lb) load, a/w = 0.33, w = 127 mm (5 in.) **147**
Figure 4.2.22 Annular Regions and Regenerated Fringe Patterns for Specimen Shown in Figure 4.2.21 ..... **148**
Figure 4.2.23 Fringe Ordering and Data Points taken from Q2 of Specimen in Figure 4.2.21 ..... **149**
Figure 4.2.24 Interface Angle 45°, 30°/60° Composite – Aluminum Bimaterial, 3.8kN (850 lb) load, a/w = 0.33, w = 127 mm (5 in.) **150**
Figure 4.2.25 Annular Regions and Regenerated Fringe Patterns for Specimen Shown in Figure 4.2.24 ..... **151**
Figure 4.2.26 Energy Release Rate vs. Interface Angle for Bimaterials with Reinforcement Directions of 0/90 Degrees in Both Halves **153**
Figure 4.2.27 Energy Release Rate vs. Angle between Reinforcement and Interface, for Bimaterials with 45 Degree Interface Angle, a/w = 0.33 ..... **154**
Figure 4.2.28 Fracture Surface (Viewing Fracture Surface Head-On) of Angled Interface Bimaterial Specimen. Interface Angle 45º, Reinforcement Directions 0º/90º **159**
Figure 4.2.29 Side View of Crack Formation Shown in Figure 4.2.28 ..... **160**
Figure 4.2.30 Schematic of Specimen View and Typical Crack Growth Patterns in Interface Angle 45º, Reinforcement Directions 0º/90º **161**
Figure 4.2.31 Fracture Surface (Viewing Fracture Surface Head-On) of Angled Interface Specimen. Interface Angle 45º, Reinforcement Directions 30º/60º **162**
Figure 4.2.32 Schematic of Specimen View and Typical Crack Growth Patterns in Interface Angle 45º, Reinforcement Directions 30º/60º **163**
Figure 6.1.1 Specimen Configuration for Dynamic Fracture Studies in Bimaterials **166**

LIST OF TABLES

Table 1 Equipment List for Circular Polariscope and Digital Imaging System 32
Table 2 False Colors and Their Corresponding Fringe Values.....78

ABSTRACT

The effects of static Mode I (opening mode) and mixed-mode (both Mode I - opening mode and Mode II - shear mode present) loading on orthotropic-orthotropic bimaterial interface cracks and isotropic-orthotropic bimaterial interface cracks has been investigated using the experimental technique of transmission photoelasticity. For successful implementation of this experimental technique a transparent and birefringent glass fiber reinforced polyester composite material was developed, enabling the direct observation and recording of photoelastic fringes in the vicinity of the interface crack in the orthotropic bimaterial. Mode I and Mode II stress intensity factors were calculated, as were the strain energy release rates, for various combinations of bimaterial halves, interface properties, and interface orientations. The experimentally obtained fringe patterns were mathematically regenerated for validating the fracture model.

1 Introduction

1.1 Problem Statement

Many high-performance structures utilize composite materials for their relative high strength and stiffness to weight ratio. In addition, the possibility of tailoring the material properties in different directions enables a wider range of application of the composite materials, generally with good results. Some long-term applications have been sports cars, recreational equipment, mountain and road race bicycles, boats, and aircraft. However, both a wide range of possible material anisotropy and a lack of accurate knowledge of the mechanical properties of the fiber-matrix interface make it difficult to predict the mechanical behavior of composite materials. In particular, it is difficult to predict the mechanical behavior of composite materials containing interfaces and especially cracked interfaces.

Examples of interfaces in critical engineering structures are found when considering an airplane whose fuselage is made from composite materials. An example of an interface between two composite materials would be an overlap between two sheets of composite material, such as in composite sheets in the transition between an airplane wing and the airframe proper, or the use of composite patches for repair of composite material based structures. An increasingly common example of an isotropic/orthotropic interface is found in an aluminum airplane structure where composite patches are used on cracks.

An example of a *cracked* interface is seen when two composite panels are glued together and there was either a bubble in the adhesive, or a section failed to bond for some unknown reason (a contaminated mating surface, for instance.)

Thus it is important to achieve a better understanding of interfacial fracture in non-isotropic bimaterials, especially orthotropic-orthotropic bimaterials, as composite materials are increasingly being used where interfacial failure can have severe or catastrophic consequences for the general public.

Such understanding will be sought using transmission photoelasticity to investigate interfacial fracture in orthotropic-orthotropic composite bimaterials. To implement this experimental technique a transparent and birefringent glass fiber reinforced polyester composite material was developed. Such a composite enabled the direct observation and recording of photoelastic fringes in the vicinity of the interface crack in the orthotropic bimaterial.

This investigation focuses on calculating Mode I and Mode II stress intensity factors and strain energy release rates for various combinations of bimaterial halves, interface properties, and interface orientations. The experimentally obtained fringe patterns are then to be mathematically regenerated to validate the fracture model.

1.2 Literature Review - Theoretical Work

In recent years the problem of static and dynamic failure of interfaces has received increased attention. There has been much theoretical work done on determining the stress and displacement fields surrounding the tip of a stationary and propagating bimaterial interface crack, as well as determining fracture criteria for such materials [1-90]. The theoretical work comprises both analytical approaches [1-64] and numerical solutions and simulations [65-90].

1.2.1 Analytical Approaches

The very first investigation was on stress fields surrounding the tip of a crack in a bimaterial interface and was performed by Williams in 1959 [1]. Williams proposed a mathematical description of the stress field surrounding an interface crack in dissimilar isotropic media, noting the occurrence of oscillatory stresses, that is, the presence of sine and cosine terms in the equations.

The oscillatory terms indicate that the stresses are not uniformly distributed around the crack tip, but vary with the angular position relative to the crack tip. Williams did find some agreement between his equations and physical reality in data provided to him on energy release from fault lines, and noted that the strain energy stored in the medium was not uniformly distributed around the crack tip. At a constant radius the strain energy stored was one-third higher at ±70° to the left or right of the direction of crack propagation.

There have been several subsequent analytical and numerical investigations of the cracked bimaterial interface problem and a common issue arises: The occurrence of two sets of solutions, oscillatory and non-oscillatory. England [2] stated that an undesirable

trait of oscillatory solutions is that they imply that the crack surfaces should wrinkle and overlap near the tips of the crack. In other terms, oscillatory solutions are considered not physically admissible or even possible. Williams hypothesized that any pronounced oscillatory character of the stress would be confined to a region very close to the crack tip.

Rice [3] visited the problem, and made two important statements: While oscillatory stress fields do imply physically impossible material overlap very near the crack tip, this region of overlap is extremely small. Also, outside any region of "physical impermissibility" the oscillatory solutions are still valid and correctly describe the stress distribution in the material. Rice also clarified some issues pertaining to the expression of stress-intensity factors. Stress intensity factors in bimaterials are often expressed as a complex stress concentration factor in the form $\boldsymbol{K} = K_{\mathrm{I}} + iK_{\mathrm{II}}$, and Rice discussed some possible ways of expressing the stress intensities in the classical form (that is, as K_{I} and K_{II} separately.)

In 1989, while considering anisotropic bimaterials, Qu and Bassani [4] derived and presented a necessary and sufficient condition for no oscillations in the crack tip fields of bicrystal interfaces. In brief, when the in-plane and anti-plane deformations of each crystal decouple in the interface coordinate system then the interface crack has the standard square-root singularity. Bassani and Qu [5] further obtained explicit solutions for the stress fields when the aforementioned conditions for non-oscillatory stress fields are met.

Wu [8] later followed up on the work of Rice, Bassani, and Qu, and offered some very specific circumstances in isotropic bimaterials where the classical stress intensity factors were valid, but did not offer more general equations where this was possible.

Comninou [10] did some early investigation work on fatigue in interface cracks, and proposed a mathematical elimination of the oscillation problem by allowing partial closure at the crack tips. The partial crack closure approach has been criticized, however. In 1991, Gao [12] more closely examined the oscillatory behavior of interface cracks, and stated that the oscillation is a consequence of lateral displacement mismatch near the crack tip.

Ma and Luo [13] offered simplified stress fields for anisotropic bimaterials that required fewer material constants than what are generally required when considering fully anisotropic materials. Deng [14,16-17] presented complex series expansions for growing cracks in isotropic bimaterials, and later also proposed general crack tip fields for both stationary and growing cracks in anisotropic bimaterials. These stress fields also contain both oscillatory and non-oscillatory solutions, and Deng states that non-oscillatory solutions *can* occur in homogeneous anisotropic bimaterials.

Liu, Huang, and Rosakis [18], analyzed a series of dynamic impact experiments previously performed by Lambros and Rosakis [103]. The analysis was undertaken because the experimental data to some degree contradicted what was expected theoretically, and it was found that in certain velocity regimes there are no oscillations near the crack tip. The overall study focused mainly on determining which velocity regimes are favorable for crack growth and to more accurately predict crack propagation velocities.

Wang [19] examined the near-tip mechanics of interface cracks from a micromechanics perspective, and proposed a stress model for isotropic bimaterials that featured oscillatory behavior but without the interpenetration that other oscillatory solution predict. This was achieved amongst others by introducing a new definition of the stress intensity factor, though there does not seem to be much follow-up on this. In a similar vein, Hurang and Chengping [22] suggested that for isotropic bimaterials, oscillatory fields can be transformed to nonoscillatory fields by adjusting the elastic constants of the materials involved, an approach that also seems to not have seen much follow-up.

Dundurs and Sotiropoulos [23] considered stress conditions and computations at bimaterial interfaces. They demonstrated a method which allows using a reduced set of equations to find the stresses on one side of the interface, if the stresses on the other side of the interface have already been computed using the “full solution”. This approach could be quite useful in multi-layer materials.

Kuang and Wang [26] performed a slightly different bimaterial analysis, starting with a hole in a bi-material plate, then considering the cracks emanating from the hole along the interface. They presented an application of the boundary collocation method for analysis. The reason for this particular investigation was to find out what happens during a common practice for “stress relief”, which is to drill a hole at the ends of a crack. In 1999 Ma and Liao [27] presented the response and dynamic stress intensity factor of a cracked interface in an anisotropic bimaterial subjected to dynamic *body* forces.

An interesting topic was investigated by Chaudhuri and Xie [30]: Does St. Venant’s principle apply to bimaterial problems? The reason for this examination was that while

most isotropic materials fail in the gage section during mechanical testing, many composite laminates and bimaterials fail in the end tab sections. In short, they stated that validity of St. Venant's principle varies, but in the case of homogeneous straight-edged materials it does apply. Having said that, this investigation did not perform any experimental work, but relied on mathematical analysis and numerical simulations for their conclusions.

In 2000, Lee [31] presented four sets of dynamic field equations (which were later augmented with experimental work together with Ricci, Shukla, and Chalivendra [113]). The equations describe the crack tip stress field and the displacement field for both isotropic and orthotropic bimaterials.

Lee's stress field equations have been adapted for this dissertation for three reasons: a) The stress field is given explicitly, b) the equations lend themselves well to use in overdeterministic analyses, and c) the equations allow calculating the Mode I and Mode II stress intensity factors explicitly and separately, rather than using the complex stress intensity factor ($\boldsymbol{K} = K_{\mathrm{I}} + iK_{\mathrm{II}}$) formulation. Though the equations were developed for dynamic crack propagation, they can be applied to static fracture by specifying a very low crack velocity when the dynamic effects are negligible.

Brock [35] presented general exact displacement fields and interface stress fields pertaining to the dynamic interface crack problem in orthotropic bimaterials. Also considered was the nature of oscillatory vs. singular solutions. The general situation concerned two-dimensional steady dynamic crack extension at constant speed. Brock and Hanson [36] expounded theoretically on two examples of this. The first example is sub-

critical crack extension (essentially very slow crack growth), while the second example concerns super-critical crack growth.

Herrmann, Loboda and Komarov [43] assessed the contact zone in a fast-growing crack in anisotropic bimaterials. Amongst others, they found interactions between the crack speed, contact zone length, and shear stress intensity. Kattis, Papanikos, and Providas [44] presented Green's functions for thermally induced stresses in anisotropic bimaterials, thus adding to the work of Ma and Liao.

Brock [46] has more recently added theoretical work on dynamic cracking in transversely isotropic bimaterials, where thermal discontinuities were also accounted for. In 2005 Prasad et al. [47,48] performed analyses similar to that of Kuang and Shen. They first presented a Green's function approach to describing a bimaterial with an elliptical hole on the interface, then performed simulations of interactions between an interfacial cavity and an internal crack. One interesting aspect of the analytical part was the use of conformal mapping to map a half-plane with a semielliptical notch onto a unit circle. However, there no explicit stress field is given, and stress intensity factors are not discussed. The simulation paper does give stress fields. It also gives several plots of the stress intensity factors and their variation with the degree of interaction between the interfacial cavity and internal crack. In 2006 Guo, Dillard, and Nairn [52] investigated the effect residual stress could have on energy release rates, and gave some numerical examples. Wang, Pan, and Feng [56] used a Green's function approach to model an anisotropic bimaterial with a viscous interface, useful in situations where damping layers have been introduced between stiff composite panels. A Green's function approach was also used by Hou, Leung, and He [60], considering thermal stresses in a three-

dimensional bimaterial. Karkamkar et al. [62] suggested improvements to the method of modeling interfaces as interlayers, especially in consideration of which material properties to specify, and gave some numerical examples. Most recently (2009), Ting [63] further expounded on this, considering anisotropic interlayers.

On a final note, the theoretical work has mainly been concerned with Mode I and Mode II fracture, while Mode III (tearing mode) has received rather less attention. One exception is the work of Wang and Karihaloo [64], who visited the matter, though indirectly. They considered Mode-II and Mode-III stress intensities at a crack that terminated on a bimaterial interface, that is, a crack that originated in the bulk material and grew onto the interface, and presented applications of this to composite material laminates.

1.2.2 Numerical Methods and Simulations

Numerical methods are used for a few general reasons: First, a numerical approach might have been intended from the outset for Finite Element Modeling or some other Computational Mechanics approach. Second, the system of equations being considered could be coupled, and thus cannot be solved analytically save for in a few special cases, for instance by coordinate transformation. Thirdly, numerical analysis might be used when no experimental data is available but preliminary theoretical predictions are desired.

Cho et al. [65] provided a numerical model, using the Boundary Element Method, to calculate the stress intensity factors in dissimilar anisotropic materials, and numerically demonstrated the applicability of the method. No experimental data were considered, however. Experimental data was considered by Lo, Nakamura, and Kushner [66]; they

presented a computational method for analyzing dynamic interface cracking in isotropic bimaterials, including an iterative scheme for simulating crack propagation. They also performed some dynamic experiments using metal-polymer bimaterials and found good agreement between the numerical simulations and the experimental data.

Akisanya and Fleck [67] considered free-edge cracks in bimaterials. They derived stress fields and presented numerical analyses of free-edge cracked bimaterials, discussing the mechanical differences between edge-cracked and center-cracked bimaterial interfaces. They defined an intensity H specific to the edge crack, in contrast to the stress intensity factor K, which they said controls the initial crack growth.

Berger and Tewary [68] proposed a boundary integral equation formulation for interface cracks in anisotropic materials. Starting with an exact Green's function, their solution contained both inverse square root and oscillatory singularities; if there was no Young's modulus mismatch between the two bimaterials then no oscillation occurred.

Sun and Qian [69] considered the strain energy release rates for different mechanical models of isotropic bimaterials and concluded that the contact model and the oscillatory model are essentially identical when disregarding the (small-scale) interpenetration. They also demonstrated how to use finite element analysis to obtain the strain energy release rates. In 1998 Qian and Sun [71] revisited strain energy release rates in bimaterials, this time considering orthotropic bimaterials. They presented finite element methods for calculating the stress intensity factors and proposed alternate definitions for Mode I and Mode II related energy release rates.

Xu, Liu, and Wang [74] presented a numerical approach for dealing with any presence of multiple mathematical singularities. Nagashima, et al. [76] gave an application of extended finite element analysis (X-FEM) to the interfacial crack problem.

Mahanta, Chakraborty, and Dutta [77] considered composite laminate crack propagation and presented an adaptive FEA method to predict delamination in layered materials due to impact.

Citing the increased use of bonded composite patches to repair aircraft, Kaye and Heller [78] presented a FEM-based three-dimensional stress analysis of the stress-concentrating effect of such a patch. Though not directly related to interfacial fracture, the paper did present interesting aspects of mechanical interactions between composites and metals.

A paper that did perform a direct numerical analysis of interfacial fracture between a composite patch on an aluminum panel was published by Hosseini-Toudeshky, et al. [79]. They presented mesh generation procedures, analyzed the effects of fiber orientations on the crack growth path, and calculated the optimum patch layer angle for certain crack configurations. Some fatigue experiments were conducted and the numerical results agreed reasonably well.

Xu, Qin, and Noda [81] numerically considered three-dimensional bimaterials (generally bimaterials that have greater thickness than height), remarking that most bimaterial investigations restrict themselves to two-dimensional bimaterials (where the thickness is much smaller than other dimensions).

Ayatollahi and Hashemi [83] revisited the composite patch problem, and added numerical methods to calculate the stresses acting parallel to the crack, and calculated the effects of the composite patches thereupon.

Another emerging trend is the use of piezoelectric materials in “intelligent” structures and systems. Zhao and Fan [84] notably presented numerical methods to find stress intensity factors for interface cracks in transversely isotropic piezoelectric three-dimensional bimaterials.

Recently revisiting the geological aspect of bimaterial interface mechanics, Ma and Beroza [87] numerically modeled dynamic crack propagation in faults with varying dip angles and some degree of material mismatch. The aim was to yield improved models of some earthquake-producing geological processes.

Menshykov et al. [89] have expanded on the numerical modeling of three-dimensional bimaterial cracks, including elastodynamics in their modeling.

1.3 Literature Review - Experimental work

1.3.1 Specimen Types

Several different specimen geometries are used to investigate interface bimaterial cracks. Suo [91] presented some types of delamination specimens for orthotropic materials and gave some representations of the stress intensity factors. However, this was not quite a bimaterial analysis; rather it studied layer separation in monolithic materials.

In contrast, O'Dowd et al. [92] described several different specimen geometries intended for measuring interfacial fracture toughness. They were symmetric and asymmetric four-point bend bars, three-point bend bars, and the Brazilian disc. The different geometries were used to vary the mode mixity (the ratio between Mode I and Mode II). This made it possible to determine the interface fracture toughness as a function of mode mixity.

Hutchinson and Suo [93] then presented several specimen geometries and discussions on mixed-mode cracking in layered materials. Much attention was given to various forms of fracture of films upon substrates, such as blistering, substrate cracking, and debonding.

A mixed-mode specimen geometry used in this dissertation was first encountered in an investigation by Shukla and Kavaturu [106], where an angled interface with a crack was used. The degree of mode mixity could then be varied with interface angle.

1.3.2 Experimental Work

The theoretical work has been augmented by experimental research on static and dynamic fracture of bimaterial interfaces [100-121], and of the experimental works that have been performed those using the method of photoelasticity are of particular interest. Photoelasticity has long been used for qualitative and quantitative analysis of structures,

and has been applied to the problem of finding stress distributions and stress intensity factors in transparent isotropic materials [96-102, 106,110,113-115,120], and transparent orthotropic materials [116],

Dally and Sanford performed early experimental work demonstrating the use of photoelasticity for static [97,98] and also dynamic [99] fracture studies in monolithic materials. Early photoelastic investigations of fracture in monolithic materials were performed on isotropic homogeneous materials, later photoelasticity has been extended to investigate the static fracture behavior of orthotropic materials by Khanna, Ellingsen, and Winter [116].

Photoelastic investigations of bimaterial interfaces were first performed on bimaterials where both half-planes where isotropic, that is, isotropic-isotropic bimaterials. Gdoutos and Papakaliatakis [100] were the first to perform such a study on the static behavior of an interface crack in an isotropic/isotropic bimaterial. They demonstrated that the photoelastic method was applicable to this problem and presented the mathematical and experimental methods to perform such an analysis.

Lu and Chiang [102] expanded on this work and proposed two different approaches to determining the stress-intensity factors from the isochromatic fringe patterns, analyzing isotropic-isotropic transparent bimaterials with elastic mismatches. Singh et al. [105] performed additional dynamic fracture studies in polymer-metal bimaterials using both photoelasticity and coherent gradient sensing. Shukla and Kavaturu [106] studied crack growth along inclined interfaces, and gave dynamic fracture criteria for crack growth along bimaterial interfaces, again using dynamic photoelasticity in an isotropic-isotropic polymer-metal bimaterial.

In 2000, Hawong et al. [110] also used photoelasticity to investigate dynamic fracture in isotropic-isotropic bimaterials with inclined interfaces. They investigated the effect of both varying the interface angle and crack location in a polymer-metal bimaterial. In 2001 Shukla [111] reviewed photoelastic investigations of dynamic bimaterial fracture. Polymer-metal bimaterials were used for the experimental work, that is, isotropic-isotropic bimaterials. The effects of several factors were examined, the factors being: crack velocity, mode mixity, and the presence of non-singular stresses. Shukla also presented useful information on how to properly interpret dynamic isochromatic fringe patterns. In 2003, Ricci et al. [113] performed dynamic experiments on an isotropic-orthotropic bimaterial fracture. They used photoelasticity to analyze the mechanical behavior of the isotropic half, while the orthotropic (non-transparent composite) half was analyzed using strain gages. A dynamic interfacial fracture study by Ricci, Shukla, and Kavaturu [114] used both strain gages and photoelasticity in the same isotropic polymer half, and compared the results from each method. They found good agreement between the strain gage data and the results from photoelastic analysis when considering isotropic materials. It must be mentioned that it remained unknown if similar results would be found upon such an investigation of orthotropic bi-materials.

One area in this field of research that has not been explored is experimental work on the static and dynamic behavior of interfaces in wholly anisotropic bimaterials, i.e. the behavior of bi-materials where both half-planes are non-isotropic. This has been due to difficulty in creating anisotropic materials and in particular simpler orthotropic materials that have sufficient transparency and birefringent characteristics for photoelastic analysis. Such a material has been developed by the research group of Khanna and Ellingsen and it

has been successfully applied in the study of Mode-I stress intensity factors in orthotropic composite materials [116]. Thus, it is now feasible to undertake experimental photoelastic studies of the static and dynamic behavior of interfaces in wholly non-isotropic or orthotropic bimaterials.

1.3.3 Ancillary Experimental Methods

In addition to what has been mentioned previously, other experimental methods have been developed prior to this investigation.

Finding the refractive index of very small objects (such as glass fibers) can be done by using a microscope and a set of liquids with known refractive indices. This is called the Central Illumination Method, and is also known as the Becke Line Method [122]. This is very useful if an Abbe refractometer is not available, and was used in the initial phases of developing the composite used in this investigation.

Sampson [96] proposed the orthotropic stress-optic law that was used in this investigation. The same stress-optic law was used successfully in the investigation of fracture in orthotropic transparent composite materials by Khanna, Ellingsen, and Winther [116].

Conventional fringe multiplication in photoelasticity is difficult to set up and calibrate, and thus digital methods have been developed. Chen [123] presented one method for digital fringe multiplication, which calculates and generates fractional light intensities and fringe patterns. This method was not used in the investigation presented here. A different method was developed in-house.

Automated fringe pattern analysis was also not used in the current investigation, but it was discussed in the future works section. There have been principal developments and

refinements of automating fringe pattern analysis by Ramesh et al. [124-126], though the presentations thereof have been limited to analysis of isotropic materials – it would be beneficial to extend that method to orthotropic materials.

1.4 Literature Review – Summary

In summary, there has been a good amount of theoretical work done on interfacial fracture in bimaterials. Isotropic, orthotropic, and fully anisotropic bimaterials have all been considered and equations describing the stress and displacement fields have been developed. A good portion of this work is development of numerical equations and attempts to apply some form of finite element analysis.

There has been considerable focus on the oscillatory behavior of the mathematical solutions. Three main approaches have been made: It has been attempted to modify the mathematical descriptions of the stresses to make the oscillations disappear. Others have developed criteria for when the oscillatory solutions do and do not occur, apparently to give investigators some situations to investigate where oscillations do not occur. Finally, several papers state that the physical implications of the oscillatory solutions can simply be neglected. In any case, the general consensus is that the physical implications and consequences of the oscillatory stress fields are limited to a very small region around the crack tip, and ignoring them is of small consequence.

The experimental work has for the most part dealt with isotropic-isotropic bimaterials, though isotropic-orthotropic bimaterials also have been examined using the measurements made on the isotropic half. Photoelasticity has been successfully used for analysis of isotropic-isotropic bimaterials, but has only been partially applied to isotropic-orthotropic bimaterials.

Isotropic-orthotropic bimaterials have mainly been investigated in one of two ways, both of which resulted from the fact that the orthotropic material half is not transparent and hence does not easily lend itself to photoelastic measurements. One way is to record

the mechanical behavior of the orthotropic half with non-optical methods. Another way is to join the orthotropic half to a transparent isotropic half, then infer the behavior of the orthotropic half by what could be observed photelastically in the isotropic half.

What has not been done previously is use to photoelasticity to directly observe the mechanical behavior of orthotropic-orthotropic bimaterials, which has been accomplished in the research reported here.

2 Experimental Methods

2.1 A Word about Units

The International System of units (SI) is not only the predominant unit system in the world, it is also the standard unit system in science. However, the official unit system in the USA is still the US Customary unit system, and engineers educated in the USA are expected to be conversant in both systems.

The machine shop at the College of Engineering is set up for US Customary units, their milling machines are US made and all measuring equipment and machine readouts are in inches (or thousands of inches). For those reasons all specimens were designed with dimensions in inches, and for sake of consistency the testing equipment was calibrated to measure loads in pounds force (lbf).

It would certainly be possible to manufacture everything in SI based units, but this would be impractical and unnecessarily complicated and time-consuming in a machine shop set up for US Customary units.

For analytical and presentation purposes the dimensions and forces have been converted to SI units. All units are presented in SI first, with the corresponding US Customary units following in parentheses.

Those are the reasons why many dimensions will appear odd in SI but with familiar-sized numbers in US Customary, such as specimen thickness of 6.35 mm (1/4 in.).

2.2 Photoelasticity

Many transparent noncrystalline (amorphous) materials that are optically isotropic when free of stress become optically anisotropic and display properties similar to crystals when they are stressed. That is, some materials undergo a *change in refractive index* when they are subjected to stress. These characteristics persist while loads on the material are maintained, but disappear when the loads are removed, provided that no residual stresses have been introduced into the material. This behavior is known as temporary double refraction and was first discovered in 1816 by Sir David Brewster. The term "double refraction" refers to the fact that the index of refraction is different in different directions of the material when the material is stressed. The method of photoelasticity is based on this physical behavior of transparent amorphous materials.

From classical mechanics it is known that at least three mutually perpendicular planes, which are free of shear stress, exist at each point in a body under load. These planes are known as principal planes and the stresses acting on them are the principal normal stresses σ_1, σ_2, and σ_3. Generally the three principal stresses have different magnitudes and are sorted according to arithmetic magnitude (that is, the sign is also being considered): σ_1 is the largest principal stress and σ_3 the smallest principal stress.

One geometrical representation of the principal planes and stresses is the *stress ellipsoid*, as shown in Figure 2.2.1. Also shown in this figure is how the optical anisotropy or the temporary double refraction can be represented by an ellipsoid, in this case called an *index ellipsoid*. Any radius of the index ellipsoid represents a direction of light propagation through the point. A plane through the origin perpendicular to the radius intersects the ellipsoid as an ellipse. The semi-axes of that ellipse represent the

indices of refraction associated with light waves having planes of vibration which contain the radius vector and an axis of the ellipse.

For an optically isotropic material (such as an unstressed amorphous material) the three principal indices of refraction are equal; as a consequence the index ellipsoid becomes a sphere and the index of refraction is the same for all directions of light propagating through the material.

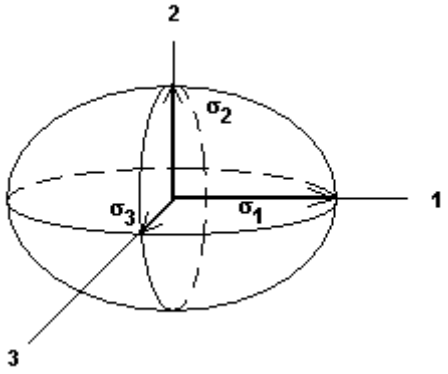

Stress Ellipsoid

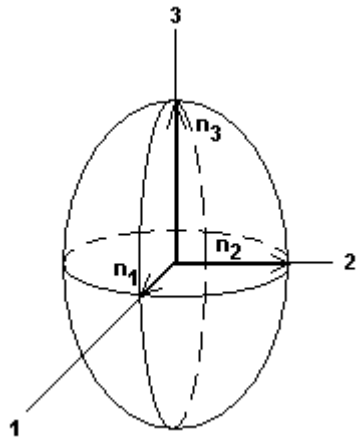

Index Ellipsoid

Figure 2.2.1 Stress and Index Ellipsoids

The similarity between the stress-ellipsoid representation of the *stress state* at a point, and the index-ellipsoid representation of the *optical properties* of a material at a point, suggests there is a relationship between the two quantities. In fact, Maxwell reported such a relationship; the changes in the indices of refraction were found to be linearly proportional to the loads and consequently, the stress state. The changes in refractive indices and the stress state are related by

$$\begin{aligned} n_1 - n_0 &= c_1\sigma_1 + c_2\left(\sigma_2 + \sigma_3\right) \\ n_2 - n_0 &= c_1\sigma_2 + c_2\left(\sigma_3 + \sigma_1\right) \\ n_3 - n_0 &= c_1\sigma_3 + c_2\left(\sigma_1 + \sigma_2\right) \end{aligned} \qquad (2.1)$$

where σ_1, σ_2, and σ_3 are the principal stresses at a point, n_0 is the refractive index of unstressed material, and n_1, n_2, and n_3 are the indices of refraction of material in a stress state associated with the principal stress direction, i.e. they are the principal indices of refraction. c_1 and c_2 are called the stress-optic coefficients. These equations are the fundamental relationships between stress and optical effect, and they are known as the stress-optic law.

The stress-optic law indicates that a complete three-dimensional stress field can be determined by measuring the three principal indices of refraction and establishing the directions of the three principal optical axes. This is very difficult to do in three dimensions; most practical applications are restricted to cases of plane stress ($\sigma_3 = 0$), in which case the stress-optic law reduces to

$$n_1 - n_0 = c_1\sigma_1 + c_2\sigma_2$$

$$n_2 - n_0 = c_1\sigma_2 + c_2\sigma_1 \qquad (2.2)$$

Measurements of absolute retardation have been done but they are difficult and time-consuming. The method of photoelasticity utilizes relative retardations and has therefore enjoyed widespread use. More details on this method can be obtained from Dally and Riley [117].

2.3 The Circular Polariscope

2.3.1 Working Principle of the Circular Polariscope

When a stressed model is placed in the field of a circular polariscope certain patterns become visible: these patterns are called isochromatic fringes. Isochromatic means “of one color”, and can be compared to isobars on a weather map; the isobars are the contours of constant barometric pressures whereas isochromatic fringes are contours of constant shear stress.

The circular polariscope consists of a light source, and four optical elements: Two polarizing filters, called the polarizer and the analyzer, and two quarter-wave plates. They are arranged in the sequence shown in Figure 2.3.1:

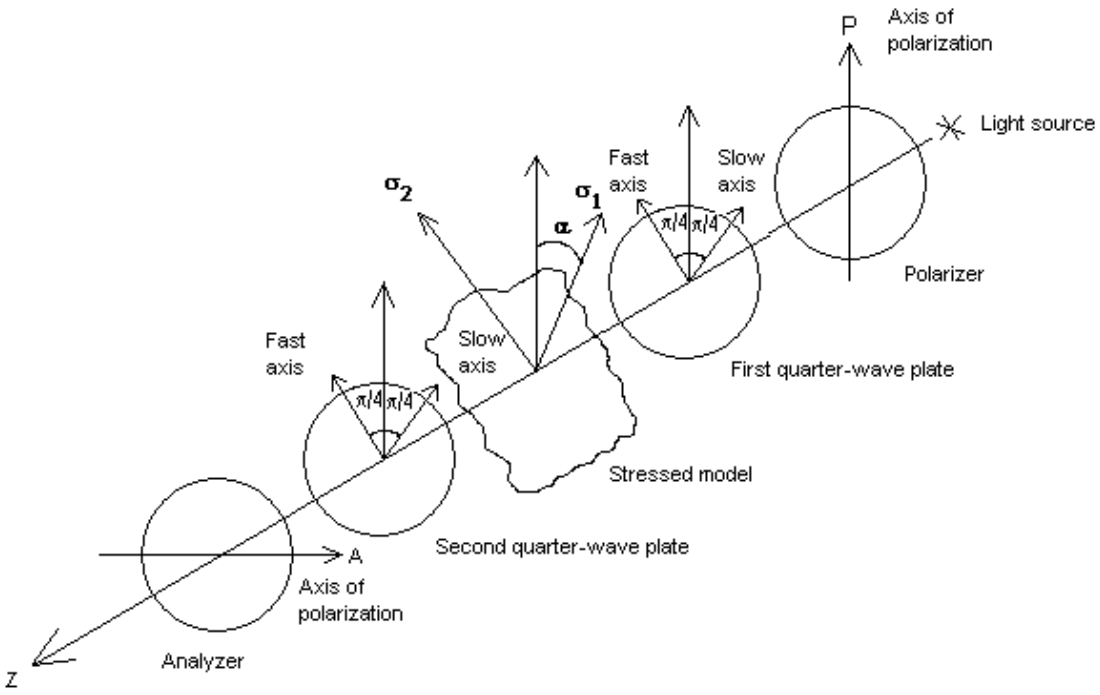

Figure 2.3.1 A Stressed Model in the Circular Polariscope

As a light beam leaves the light source in a polariscope it enters the polarizer and emerges plane-polarized, that is, only light waves whose electric vector is parallel to the axis of polarization emerge from the polarizer.

The light beam emerging from the polarizer then enters the first quarter-wave plate and its electric vector is resolved into two components E_f and E_s parallel to the fast and slow axes of the quarter wave plate, respectively. Inside the quarter-wave plate the component parallel to the slow axis travels slower than the component parallel to the fast axis, and thus develops a phase shift. Upon leaving, the slow component has developed a phase shift Δ of a quarter-wave, that is, $\Delta = \pi/2$.

The components that left the quarter plate (denoted E'_f and E'_s) enter the model. The stressed model behaves like a temporary wave plate; inside the model the components of the light beam are resolved into "new" components E_1 and E_2 whose directions of vibration are parallel to the directions of the principal stresses σ_1 and σ_2 in the model. The two components propagate through the model at different velocities and the emerging components E'_1 and E'_2 have a greater relative retardation than E_1 and E_2.

When the light emerges from the model it enters the second quarter-wave plate, and another phase shift develops as the light is resolved into components along the fast and slow axes of the wave plate. Upon leaving the second wave plate the light components have developed a relative phase shift of 90 degrees between the slow components E'_f and E'_s. Finally, the light enters the analyzer. The vertical components of E'_f and E'_s are absorbed in the analyzer while the horizontal components are transmitted.

The intensity of the light beam emerging from the circular polariscope is a function only of the principal-stress difference. The isochromatic fringes are the contours of

maximum shear stress in the plane of the specimen. The isochromatic fringe patterns are averaged through the thickness of the model material; consequently the stresses that are found from photoelastic analysis are the average stresses through the thickness of the material [2]. Such isochromatic fringe patterns are visible in Figure 2.3.2, which shows an orthotropic-orthotropic bimaterial (consisting of a glass fiber reinforced polymer composite that is transparent to light) under load in the polariscope.

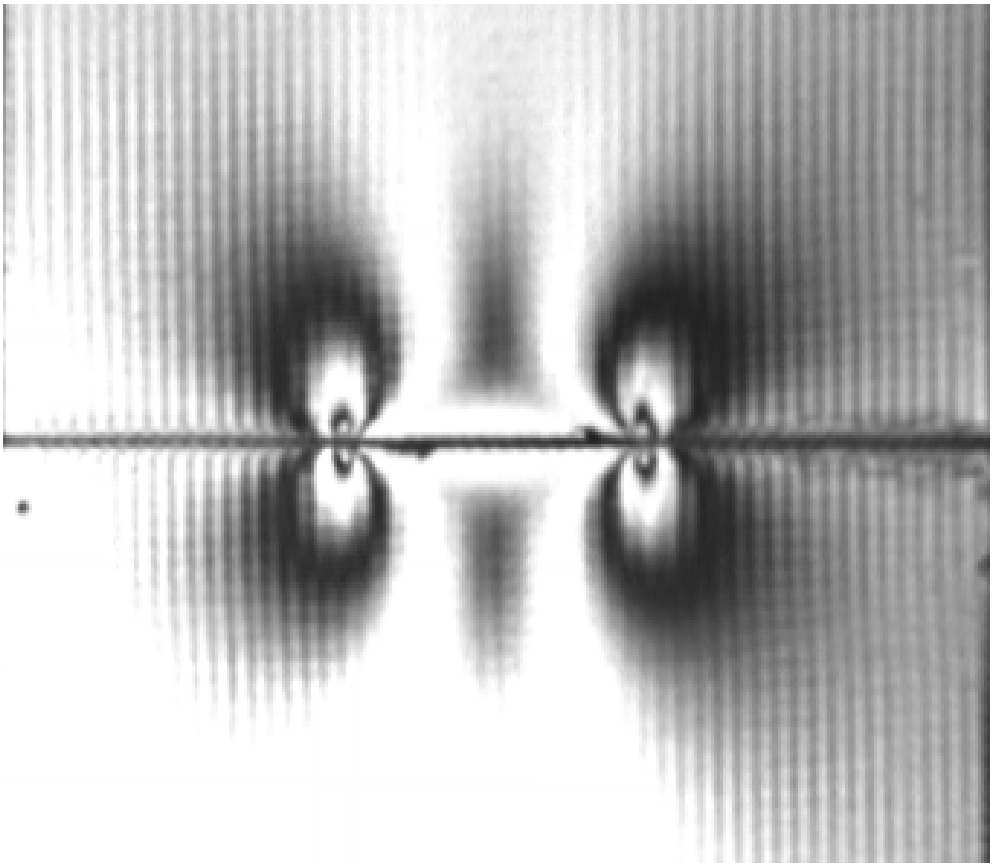

Figure 2.3.2 Isochromatic Fringes Surrounding the Crack Tips in an Orthotropic-Orthotropic Bimaterial with Horizontal Interface

2.3.2 The Circular Polariscope and Digital Imaging System

The polariscope was purchase from Terco and was modified to use an in-house designed loading system that could apply much higher loads than the loading system that came with the polariscope. The loading frame is welded steel channel, while a hand-pumped double-acting hydraulic cylinder is used to apply load. The applied loads are measured with an S-shaped load cell which is connected to a digital readout. Finally, isochromatic fringe patterns are recorded live with a digital imaging system. Table 1 gives the specifications for the components of this system, while Figure 2.3.3 is a photograph of the system as currently configured. The digital camera was situated atop a crate to bring its field of view level with the specimens. The hand pump was bolted to the table, while the directional valve was bolted to the loading frame itself. The hand pump was situated such that the operator could observe the fringe patterns developing in the specimens as load was applied.

To ensure that the polariscope was properly set up (polarizing filters and quarter-wave plates set in their correct orientations), a Homalite disc was placed in compression (Figure 2.3.4) and observed in the polariscope (Figure 2.3.5). If the circular polariscope was set up properly in the dark field, there should be no isoclinics present (that is, fringes showing the principal stress directions), and unstressed regions should appear dark. Isoclinic fringes in a disc in compression show up as a cross. No such fringes were apparent in Figure 2.3.5. The outer diameter was a free surface and could not carry stress, therefore it was expected to appear dark (as this would be the zero order fringe in the dark field of the circular polariscope). This was also the case. Thus the polariscope was confirmed to be set up properly.

Table 1 Equipment List for Circular Polariscope and Digital Imaging System

Item	Manufacturer	Model	Comment
Loading Frame	Dakota Steel, Rapid City, SD	(Custom)	C8 x 13.75 steel channel, welded
Grips	Shoener Machine, Rapid City, SD	(Custom)	Mild steel
Polariscope	Terco	Terco MT-3100	
Load Cell	Transcell	BSS-5K	S-Shaped, 22 kN (5000 lb.) capacity
Load Cell Readout	Transcell	TI500E	Calibrated by manufacturer
Hydraulic Pump	Brand Hydraulics	HP-121-DA-95	Hand operated
Hydraulic Cylinder	Sheffer	2M-FF6	Double-acting
Directional Valve	Cross Hydraulics	n/a	
Digital Camera	Pulnix	TM-1040	Black-and-white camera, 30 fps capacity
Imaging Software	Epix Inc.	Xcap 2.2	
Computer	Generic IBM-Compatible	(Custom)	OS: Windows 2000

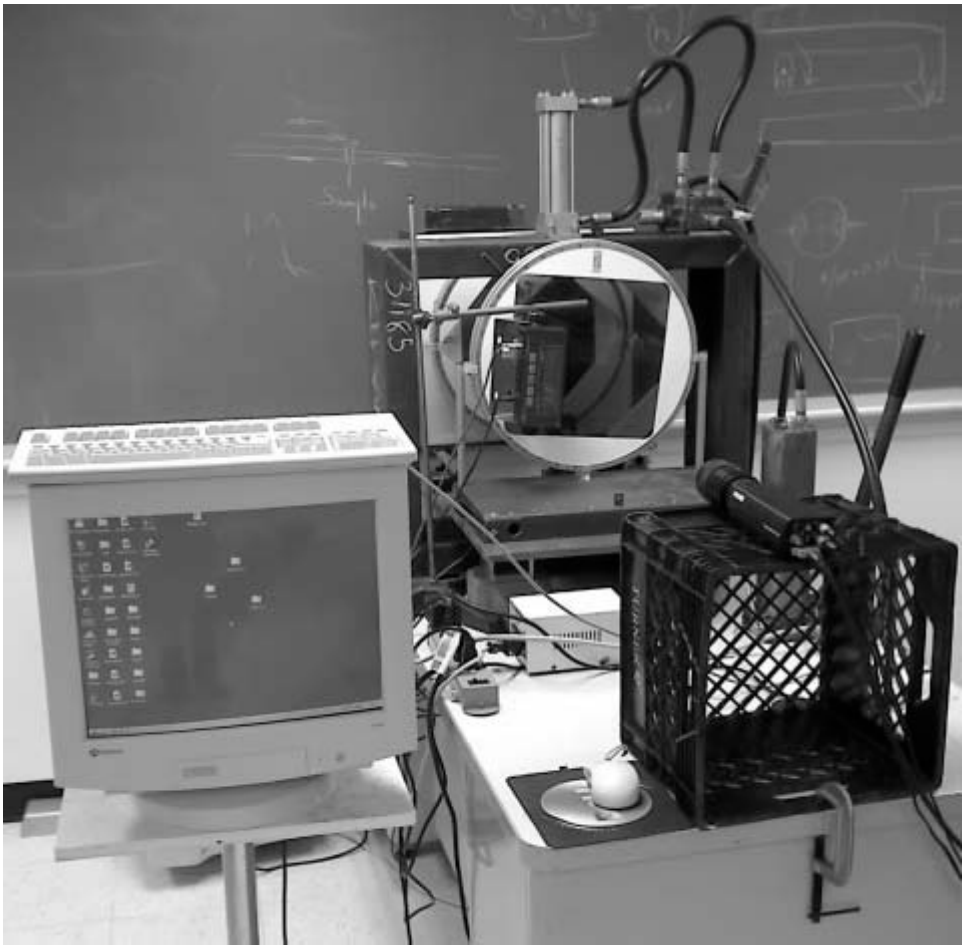

Figure 2.3.3 Polariscope, Loading Frame, and Digital Imaging System

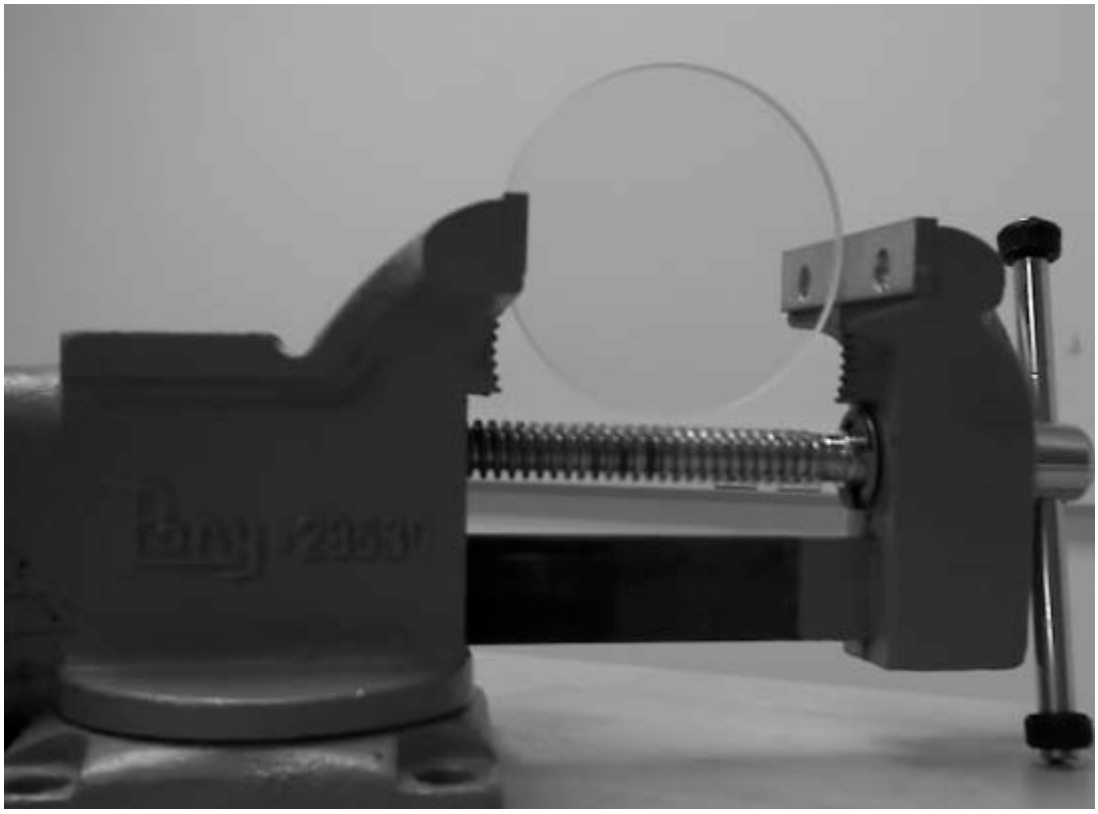

Figure 2.3.4 Homalite-100 Disc Under Compression in a Vise, Seen in Normal Light

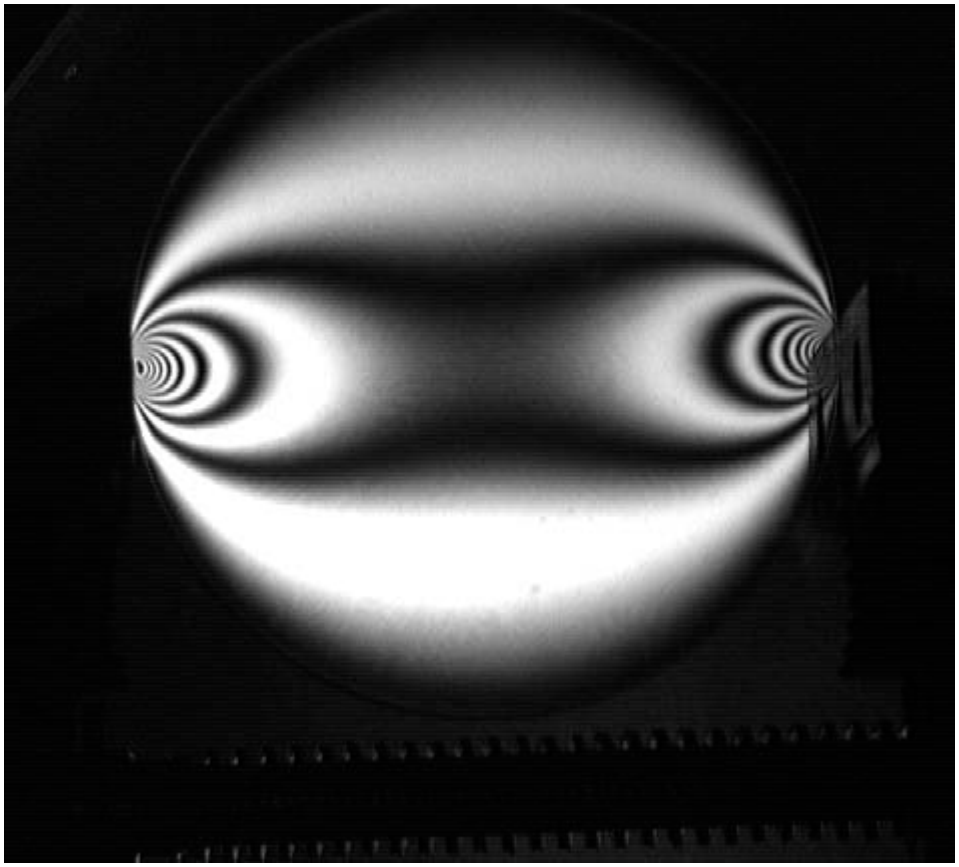

Figure 2.3.5 Homalite-100 Disc in Compression in Dark-Field Circular Polariscope

2.4 Specimen Configurations

2.4.1 Specimen Configurations Used

For modeling purposes, an interface was created by joining two bi-materials together with a butt joint. Within the interface a crack was created by preventing bonding in the desired crack location. Bonding was prevented by covering the desired crack area with Teflon tape. Normally, composite materials are not joined with butt joints, but the butt joint specimens serve the purpose well for investigating the mechanical behavior of both butt and lap joints, as will be explained in the next few paragraphs:

Butt-joint bi-material specimens were made in two general configurations, illustrated in Figure 2.4.1. The first configuration had a horizontal interface for Mode I dominated loading. The second configuration had an angled interface, with varying angles, to obtain different degrees of mixed-mode loading. Figure 2.4.2 and Figure 2.4.3 show actual images of isochromatic fringe patterns obtained from both specimen geometries, while the definitions of the relevant dimensions are illustrated in Figure 2.4.4.

There was one important issue pertaining to the angled interface specimens, as illustrated in Figure 2.4.5: How to define crack length and a/w ratio? If the crack length is kept at some absolute fixed length (Figure 2.4.5a), then the crack projection and its effective length decreases with increasing interface angle. With increasing interface angle, the interface itself becomes longer. With a fixed crack length, the crack length vs. interface length would then decrease. For these reasons it was decided that crack length and a/w ratio would be defined in terms of *effective* crack length and a/w ratio. Therefore, for the mixed-mode specimens the specimen width was denoted w_s while the interface length was denoted w, and the crack length a was set so that the a/w ratio would remain constant for varying interface angles as shown in Figure 2.4.5b. In other words, for

angled interface specimens the *relative crack length* specimen type was used.

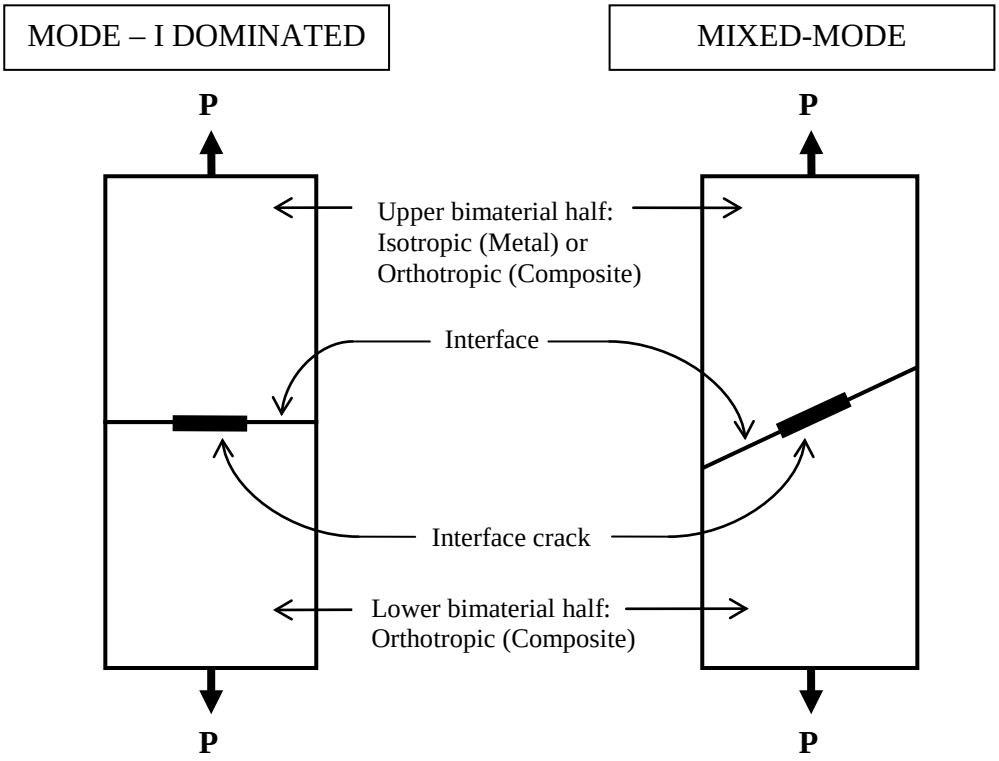

Figure 2.4.1 Specimen Configurations

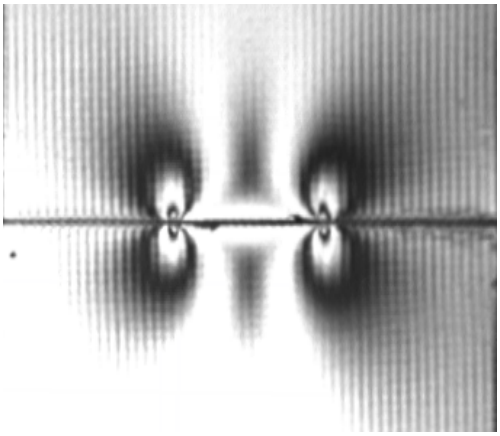

Figure 2.4.2 Orthotropic-Orthotropic Horizontal Interface Bimaterial Specimen under Load

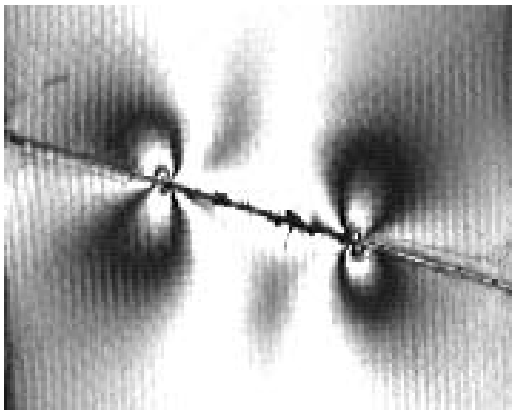

Figure 2.4.3 Orthotropic-Orthotropic Angled Interface Bimaterial under Load

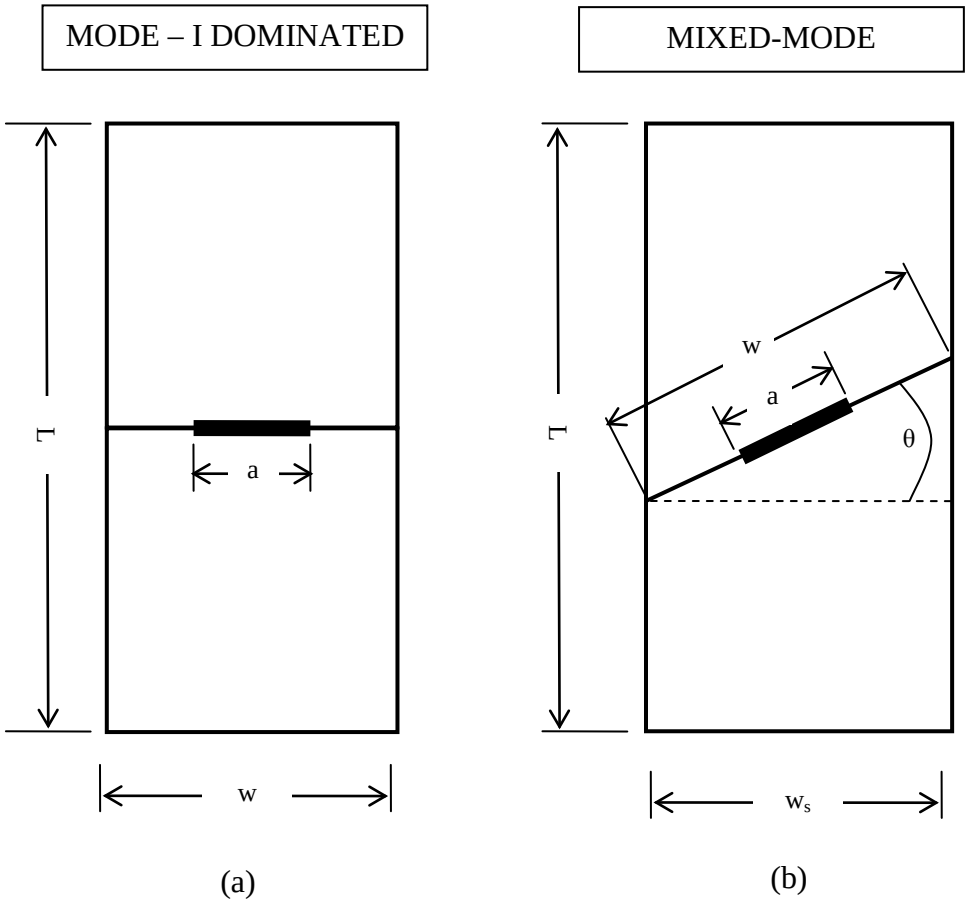

Figure 2.4.4 Definitions of Specimen Dimensions

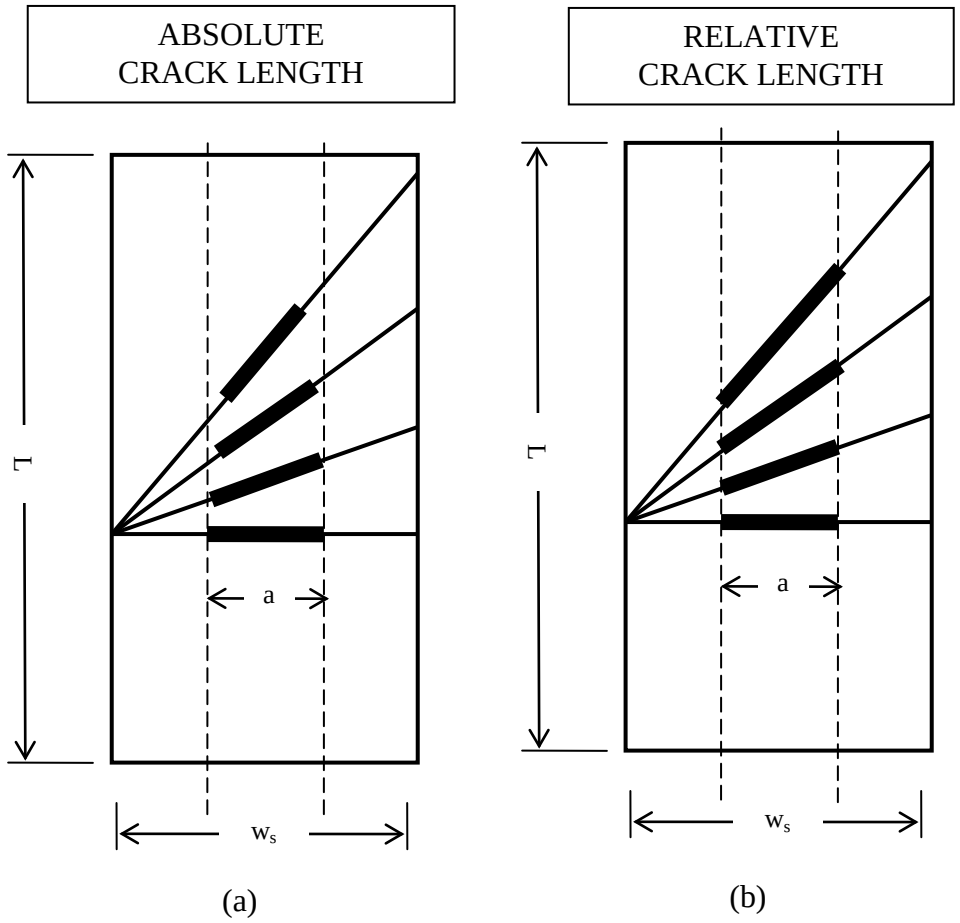

Figure 2.4.5 Absolute vs. Relative Crack Length

Several other types of mixed-mode specimens were tested, with disappointing results. The first type tested was the Double-Cantilever Beam (DCB) specimen, as illustrated in Figure 2.4.6. The mode mixity was to be varied by varying the location of the bimaterial interface relative to the centerline of the overall specimen. These specimens simply broke very prematurely, producing no useful isochromatic fringes.

The next type tested was the Brazilian Disc. The specimen type is illustrated in Figure 2.4.7 while Figure 2.4.8 shows an actual composite-composite Brazilian Disc in under low compressive load in the polariscope. The mode mixity was to be varied by varying the angled between the applied loads and the interface.

Finally, Four-Point Bend (FBD) specimens were fabricated and tested, the principle is sketched in Figure 2.4.9 and Figure 2.4.10 shows an actual composite-composite FBD specimen under load in the polariscope. The mode mixity was varied by varying the relative heights of the upper and lower specimen halves.

The BD and FBD specimens did produce a useful number of fringes, but attempts to regenerate them properly were unsuccessful. As can be seen in the photoelastic images, fringes from the loading points would interfere with the fringes emanating from the crack tips, and it seems likely this interference prevented successful analysis and regeneration. Such interference was not observed in the angled interface specimens unless loads were very high, 4.5 kN (1000 lb.) or more.

In conclusion, for the BD and FBD specimens the remote stress field was not sufficiently homogeneous for successful implementation of the photoelastic and analytical approach used in this investigation.

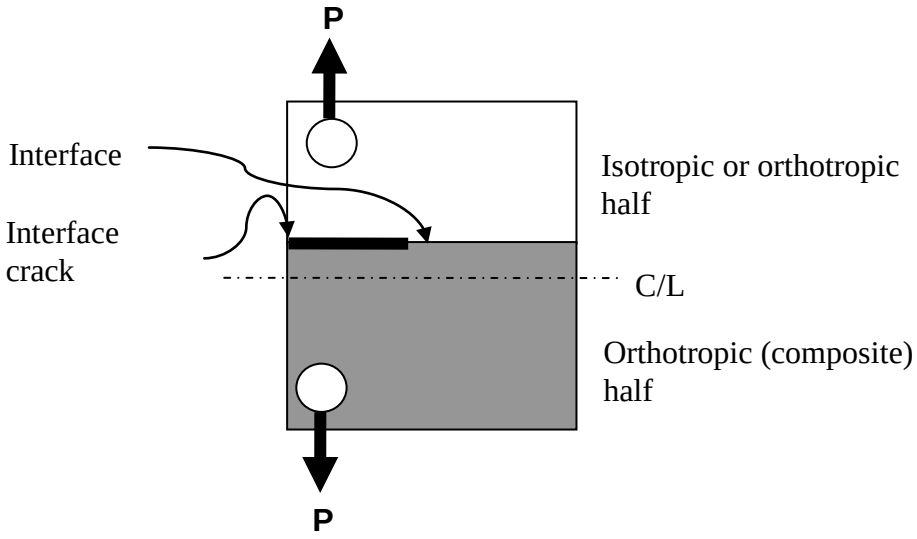

Figure 2.4.6 Schematic of Double-Cantilever Beam Interface Specimen

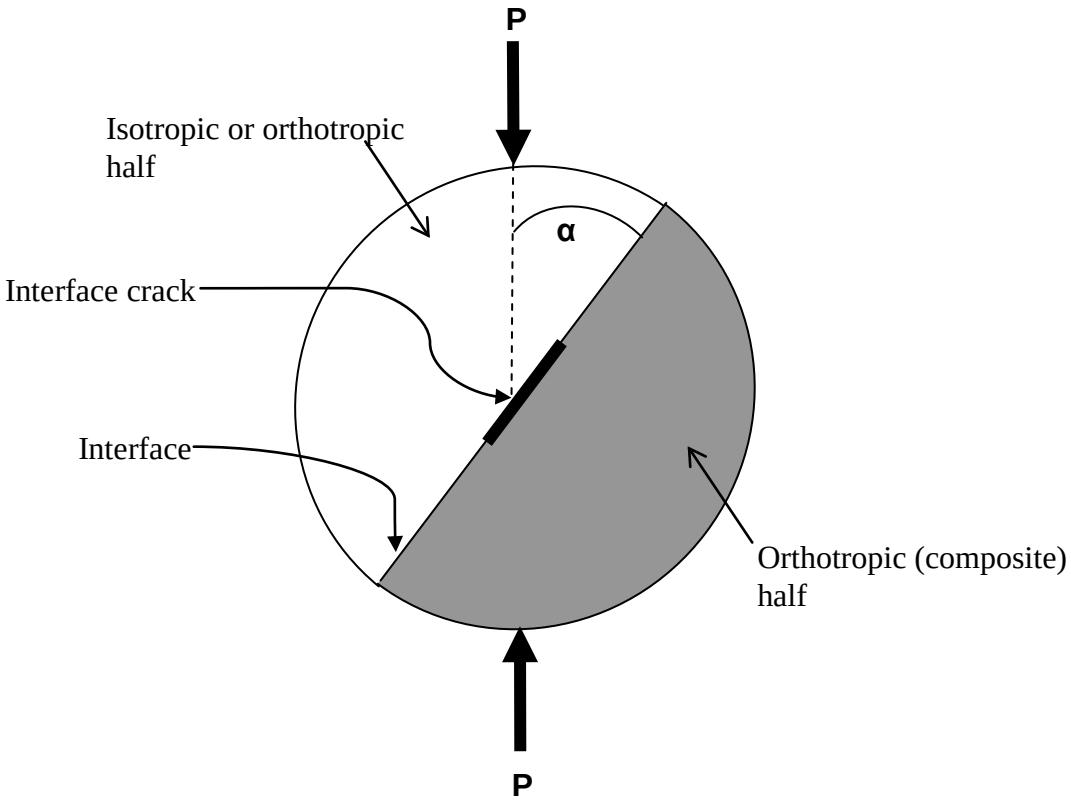

Figure 2.4.7 Schematic of Brazilian Disc Specimen

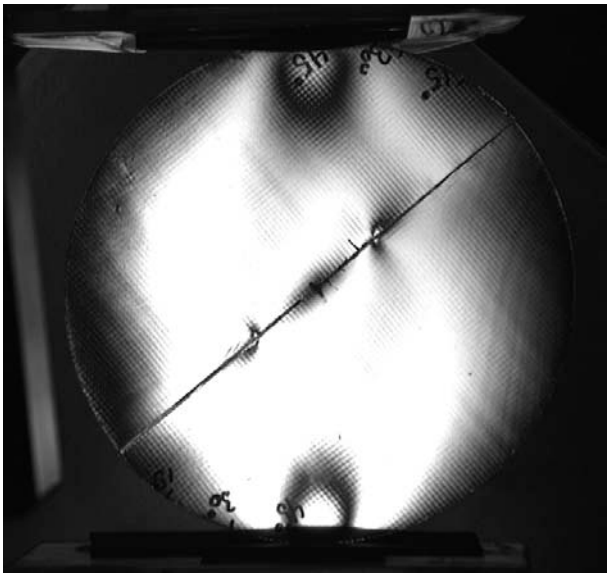

Figure 2.4.8 Composite-Composite Brazilian Disc Specimen Under 0.7 kN (160 lb) Compressive Load in Polariscope. Fringes Emanating from Loading Points even at this Very Low Load

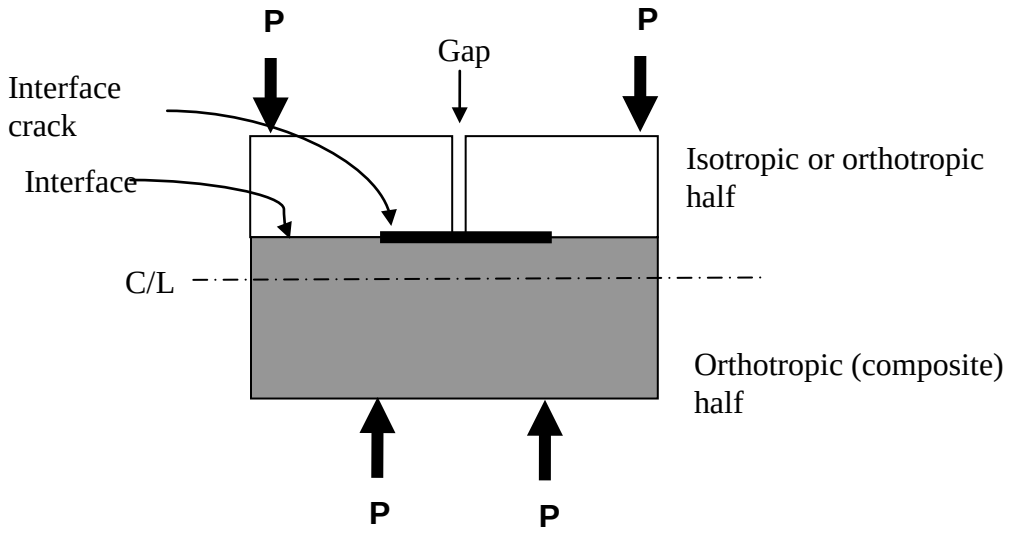

Figure 2.4.9 Schematic of Four-Point Bend Specimen

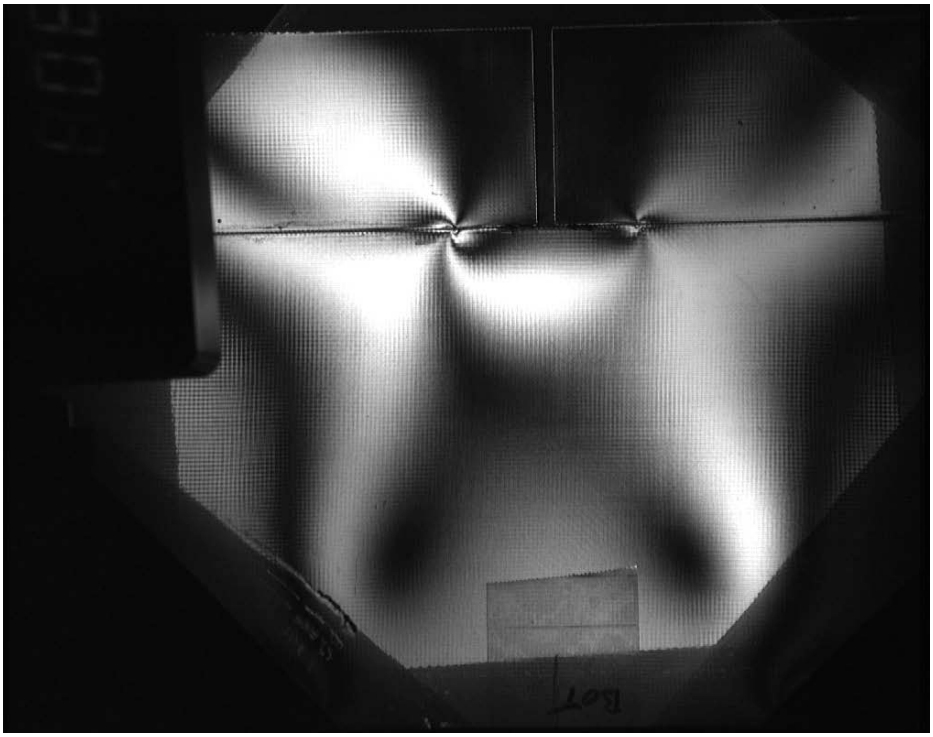

Figure 2.4.10 Composite-Composite Four-Point Bend Specimen Under 5.8 kN (1300 lb) Load in Polariscope

2.5 The Transparent Composite Material

2.5.1 Specifications

The composite material used in this investigation was a polyester matrix composite reinforced with bi-directionally woven E-glass cloth. The Polyester was grade MR17090 supplied by Ashland Chemical Co., which was cured with Methyl Ethyl Ketone Peroxide (MEKP) while Cobalt Octanate was added as a cure accelerant. The curing agents were available from any chemical supplier. The glass cloth was obtained from Aerospace Composite Products. A template together with a glass cloth cutter of the "pizza wheel" type was used to cut the cloth to size and shape. The cloth had to be somewhat smaller than the aluminum frame; a margin of 12.7 mm (0.5 inches) between the cloth edges and the aluminum frame was desirable to allow for purging of any air bubbles. The composite had to cure at room temperature for at least two days.

The composition of the matrix was chemically tailored so that its optical index of refraction closely matched that of the glass fibers, ensuring sufficient transparency for photoelastic analysis. Seven layers of glass cloth yielded a fiber volume fraction of about 18%. The thickness of the composite material was 6.35 mm (1/4 inch); it was fabricated by a hand lay-up technique, in two sizes of sheet: 330 mm by 510 mm (13 by 20 inches) and 400 mm by 510 mm (16 by 20 inches). The transparency of the composite material is demonstrated in Figure 2.5.1, a photograph of the author where the composite covers half of the author's face.

Figure 2.5.1 Author Partially Seen Through Composite Used in Investigation.

2.5.2 Fabrication Technique

As is illustrated in Figure 2.5.2, a 6.35 mm (1/4 inch) thick aluminum frame was laid on top of PVC plate clad with a Mylar sheet. Packing tape was used to cover the gap between the Mylar sheet and the PVC plate; this prevented any resin spillover from seeping in between the Mylar sheet and PVC plate when the mold arrangement was erected. Lumps of clay were placed against the sides of the aluminum frame; this prevented the frame from sliding around on the Mylar sheet, and also prevented the frame elements from accidentally separating.

Prior to pouring, the resin was degassed in a vacuum chamber to remove air bubbles that were introduced during mixing. Typically, degassing for 10 minutes at a gage pressure of -84.4 kPa (-25 in. Hg) removed all air bubbles.

The layup process started by pouring some resin into the frame (enough to cover the area inside the frame), and then laying down a fiberglass cloth. Sometimes bubbles of air would form underneath the cloth as it was laid down. In such cases a spatula could be used to purge air bubbles, though this had to be done with care; multiple layers of cloth could be pressed too closely together if a spatula was used too vigorously.

Resin was then poured on top of the first cloth layer, and a new layer of cloth was laid down. This process was repeated until all layers of cloth were laid down.

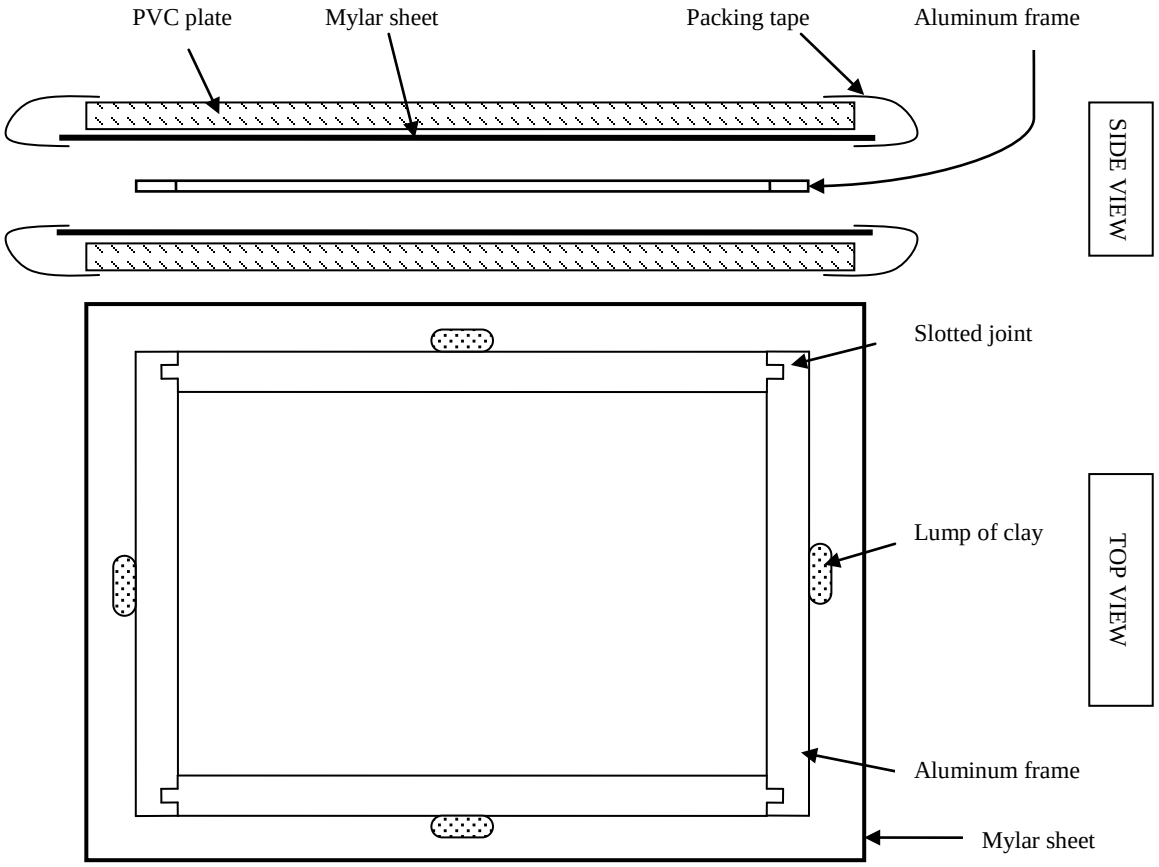

Figure 2.5.2 Mold for Making Composite Material

When all the layers had been laid down another Mylar-clad PVC plate was laid on top of the frame. The top and bottom plates were then clamped firmly with C-clamps against the aluminum frame. This arrangement was then erected sideways. The upright position of the mold caused any lack of resin to form an edge void rather than a large surface void. In addition, bubbles that may have become trapped underneath a cloth layer traveled to the top of the erected mold arrangement.

2.5.3 Fiber Volume Fraction of the Composite Material

The fiber volume fraction of the composite was found with a "burn-out" test. A crucible was placed on a precision scale, and the scale was tared. A section of composite was cut and placed in the crucible, and the weight was recorded. The composite was then subjected to a flame from a welding torch until all the resin had been burned off and only glass reinforcement remained. The crucible was then placed on the scale again and the weight of the glass was recorded. Using the densities of glass and resin, the volumes of glass and resin were determined and the resulting volume fraction of reinforcement was found.

The weight of the composite was 48.68 grams, and the weight of the reinforcement after burn-out was 14.66 grams. The mass of resin burned off thus was 34.02 grams. The density of the resin is 1.094 kg/liter, while the density of the glass reinforcement is 2.60 kg/liter. For the composite section tested, this yields a resin volume of $31.1 \cdot 10^{-6} m^3$ and a reinforcement volume of $5.64 \cdot 10^{-6} m^3$, resulting in a reinforcement volume fraction of 18.1%.

2.5.4 Photoelastic Properties of the Composite Material

The photoelastic response of a material is a measure of which fringe order will be observed in, for instance, the dark field of the polariscope for a given stress in the material. The photoelastic response can be found by loading tensile specimens in the polariscope while recording fringe orders and load. For this purpose, 25.4 mm (1 inch) wide strips were cut from the fabricated composite plates with reinforcement directions of 0°/90° and ±45°, as illustrated below in Figure 2.5.3 . The in-house made machining jig shown in Figure 2.5.4 greatly facilitated machining these specimens, it allowed up to five such specimens to be machined simultaneously.

The specimen dimensions were based on the ASTM standard for tensile testing of composite materials, ASTM D3039. The specimens have an overall length of 254 mm (10 in.), and are 50.8 mm (2 in.) wide at the ends, with 19.1 mm (3/4 in.) diameter holes where the loading pins attach. The central section of the specimens is 25.4 mm (1 in.) wide. An “analysis section” of 50.8 mm (2 in.) length is designated in the center part of the specimens. This area is considered sufficiently far away from the loading holes and geometry changes that these do not affect the optical and mechanical behavior of the material in the analysis section.

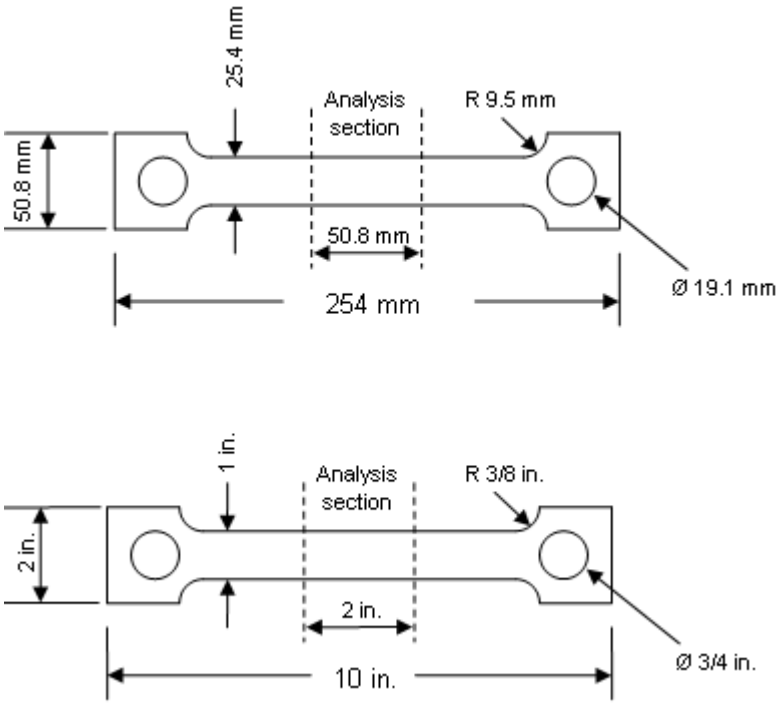

Figure 2.5.3 Specimens for Determining Composite Properties, in SI and US Customary Units

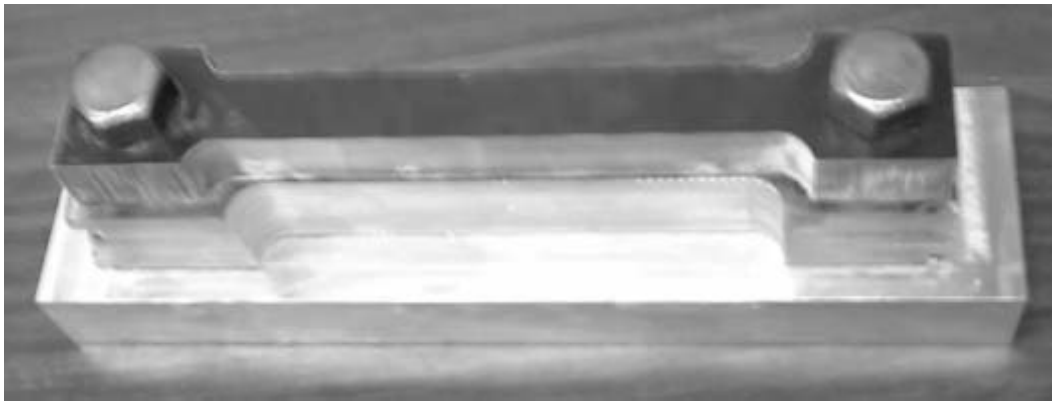

Figure 2.5.4 Machining Jig for “Dogbone” Composite Specimens

The composite strips were loaded in tension in the “dark field” of the polariscope. In the dark field, a specimen under no load appears dark. This is the zero-order fringe. When tensile load is applied the specimen gradually appears brighter, and as maximum brightness is reached we have a half-order fringe. The specimen then grows darker again as the load increases, and we are then observing the first order fringe.

A digital light meter was used to measure the intensity of light transmitted through the analysis section of the specimen. To ensure that only the intensity of light traveling through the composite was recorded, a mask-and-tube arrangement was created, as illustrated below in Figure 2.5.5.

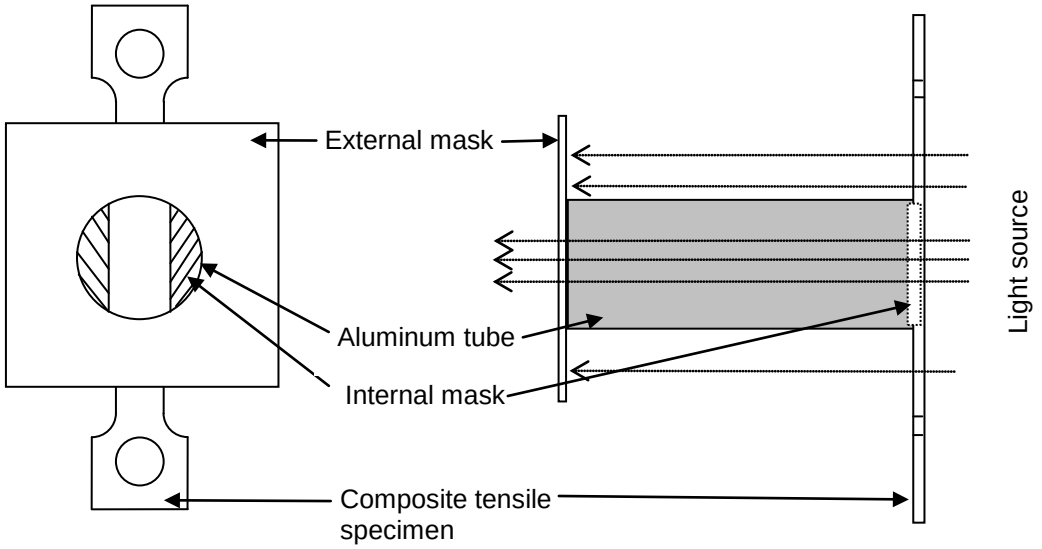

Figure 2.5.5 Tube and Mask Arrangement for Photoelastic Property Tests

A two-inch diameter aluminum tube was fitted with an internal mask on one end and an external mask on the other end. The internal mask fitted around the specimen, so that light would only enter the tube through the specimen. The external mask on the other end would ensure that only light traveling through the tube would enter the light meter.

During testing, intensity and load were recorded as the load increased and then plotted, as shown in Figure 2.5.6.

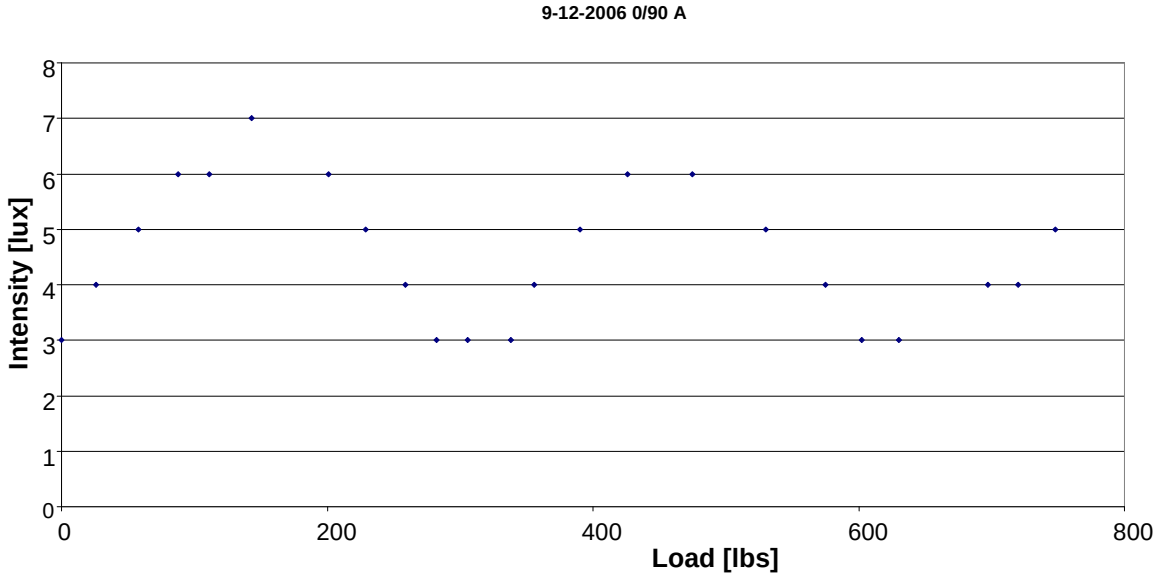

Figure 2.5.6 Intensity vs. Load for 0/90 Degree Reinforcement Angle Tensile Specimen

From this plot, the fringe order vs. load were determined. The specimen was loaded in the “dark field” and so where the intensity is lowest we have whole-order fringe, and where the intensity is the highest we have a half-order fringe. From this a load vs. fringe order plot was generated:

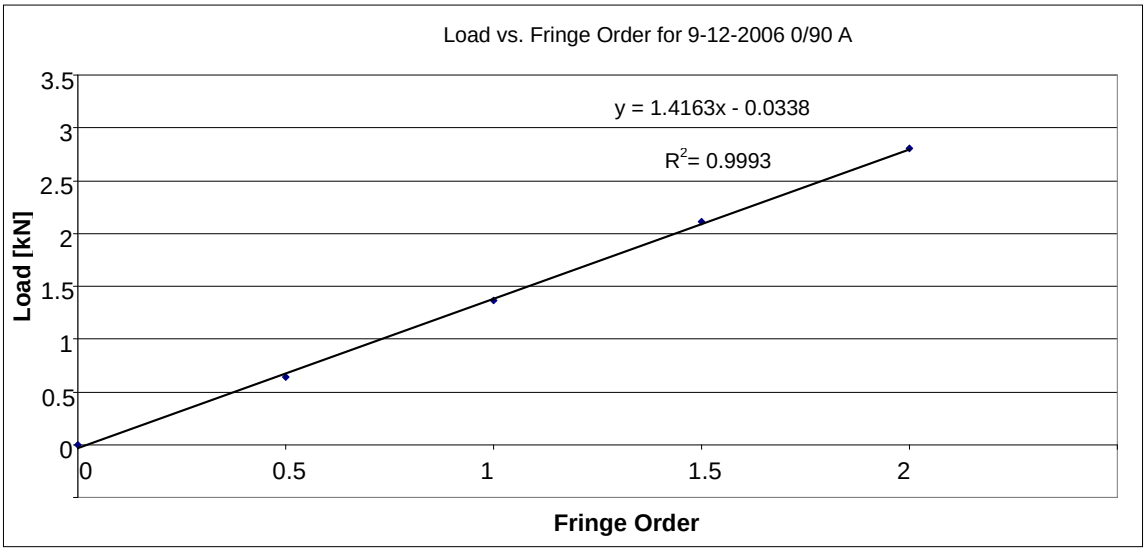

Figure 2.5.7 Load vs. Fringe Order for 0/90 Degree Reinforcement Angle Tensile Specimen

The photoelastic response, or stress-fringe value, f_σ was then calculated using the expression

$$f_\sigma = \frac{\sigma}{N} \cdot t = \frac{P \cdot t}{N \cdot w \cdot t} = \frac{P}{N \cdot w} \tag{2.3}$$

where σ is the normal stress, P is the applied load, w the specimen width, t the thickness, and N the observed fringe order. A linear curve fit was used across the data range, and then the photoelastic response was calculated by dividing the slope of the load vs. fringe order curve by the specimen width. The procedure was repeated for a tensile specimen with reinforcement directions of ±45°, with results as shown in Figure 2.5.8 and Figure 2.5.9.

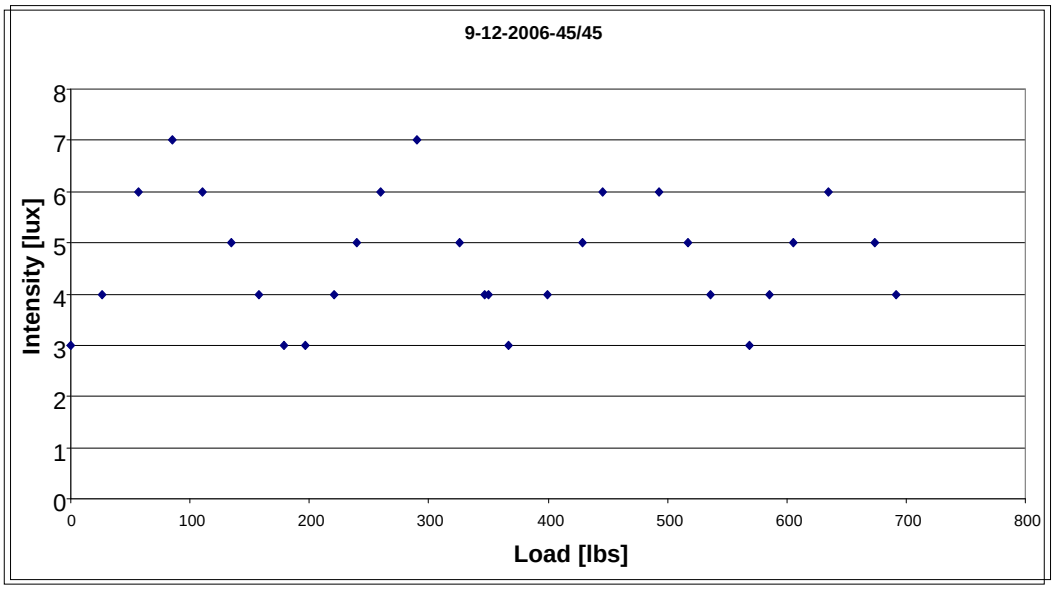

Figure 2.5.8 Intensity vs. Load for +/- 45 Degree Reinforcement Angle Tensile Specimen

Figure 2.5.9 Load vs. Fringe Order for +/- 45 Degree Reinforcement Angle Specimen

The photoelastic response of the material was found to be

$$f_L = f_T = 55.9\frac{kPa \cdot m}{fringe} \quad \text{and} \quad f_{LT} = 32.3\frac{kPa \cdot m}{fringe} \text{ where}$$

f_L and f_T are the photoelastic responses of material samples cut along the 0° and 90° reinforcement directions, respectively, while f_{LT} is the photoelastic response of the material samples cut in the ±45° reinforcement directions. The mechanical properties of the composite are equal in the *L* and *T* directions, so it is reasonable to expect that f_L equals f_T. This was also found to be the case. As can be seen in Figure 2.5.7 and Figure 2.5.9 the photoelastic response was linear with respect to load throughout the loading range.

2.6 Mechanical Properties of the Composite Material

The mechanical properties were found using procedures based on ASTM test methods D3039-76 and D3518-76.

2.6.1 Young's Modulus

25.4 mm [1.0 in.] wide strips were cut from the fabricated composite sheets oriented so that they had reinforcement directions of 0/90 degrees and ±45 degrees. The strips were machined to ensure that they were straight and had smooth edges. To apply load to the samples, 12.7 mm [0.5 in.] pin holes were made at each end of the strips where pins attach to the grips. Strain gages were attached on each side of both specimens, in the lateral and longitudinal directions. In the longitudinal direction, a Measurements Group CEA-13-240UZ-120 strain gage was used on both specimens. This is a 6.1 mm [0.240 in.] gage length, 120 Ohm strain gage with self temperature compensation. In the transverse direction, a Measurements Group "Small" (3.05 mm [0.120 in.] gage length, 120 Ohm) was used. The small gage was used due to the narrow geometry in the transverse direction. Polyester is a poor conductor of heat, so it was expected that the strain gages would warm up more when mounted on the composite samples than if they were attached to metal specimens. To reduce error from thermally induced strains and thermally induced drift, the strain gage circuits were turned on and balanced an hour before tensile tests were performed. The assumption is that after one hour, the gages would have reached a thermal equilibrium with the surroundings. After one hour, the circuits were again balanced, and the tensile tests commenced. The specimens were loaded in tension while recording load, lateral strain, and longitudinal strain. The

recorded data was entered into a spreadsheet and a plot was made based on recorded strain and calculated normal stress.

The 0°/90° specimen was used to find the modulus of elasticity and the Poisson's ratio of the material. The ASTM D3039-76 standard gives the following mathematical expression for modulus of elasticity:

$$E = \frac{\Delta P}{\Delta l}\left(\frac{l}{bd}\right) \qquad (2.4)$$

The modulus of elasticity is calculated from the slope of the load vs. deformation line, using eq. (2.4) where l is the longitudinal strain gage length, b is the specimen width, and d is the specimen thickness. Measured with machine shop calipers, the 0/90 degree specimen was 25.3 mm [0.998 in.] wide and 5.38 mm [0.212 in.] thick. For presentation purposes, the load and strain data were converted to stress and strain data, as shown in Figure 2.6.1. It was observed that the material exhibited a linear response throughout the loading range. The modulus of elasticity was found to be $E = 9.65$ GPa [1.4 MPSi]. The Poisson's ratio ν was found by averaging the difference between lateral and longitudinal strain throughout the loading range, yielding a Poisson's ratio $\nu = 0.25$.

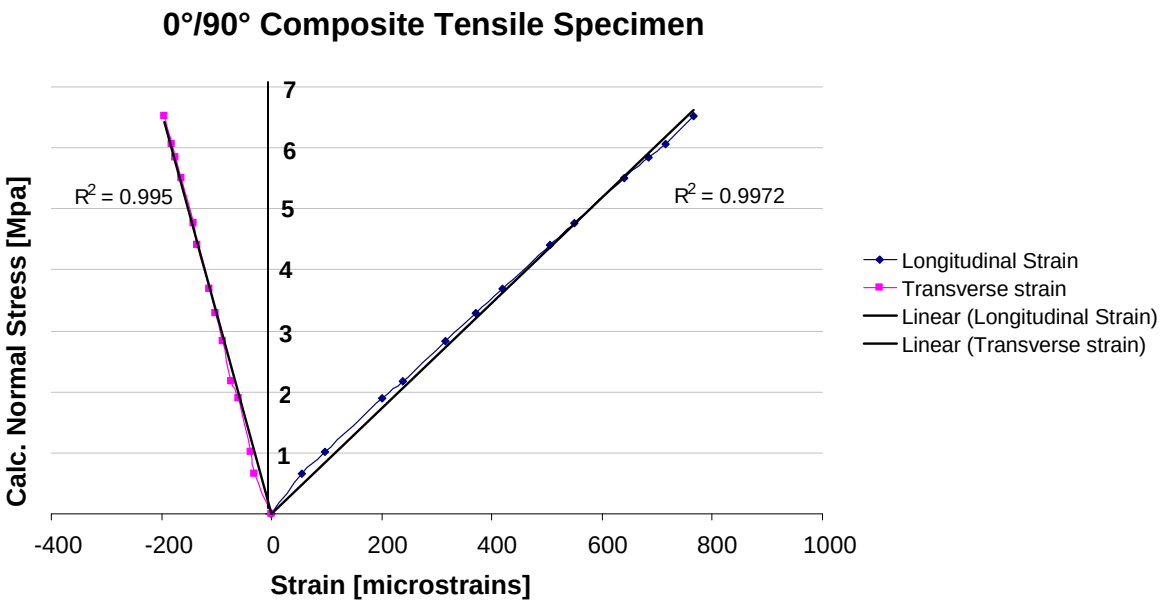

Figure 2.6.1 Stress vs. Strain Plot for 0/90 Degree Composite Tensile Specimen

2.6.2 Shear modulus

The shear modulus of the material was found in a similar manner. The ±45° specimen was loaded in tension while recording load and longitudinal and lateral strain. The ASTM D3518-76 standard specifies calculating shear modulus *G* as:

$$G = \frac{\Delta \tau_{12}}{\Delta \gamma_{12}} \tag{2.5}$$

where:

$\tau_{12}^{i} = \dfrac{P_x^i}{2bd}$

$\gamma_{12}^{i} = \varepsilon_x^i - \varepsilon_y^i$, and

$P_x^{\,i}$ = load at i^{th} point of ±45° specimen tensile load-deformation curve

τ_{12}^{i} = shear stress at the i^{th} point of the unidirectional shear stress – strain curve

γ_{12}^{i} = shear strain at the i^{th} point of the unidirectional shear stress – strain curve

$\varepsilon_x^{\,i}$ = longitudinal strain at the i^{th} point of the ±45° specimen tensile load deformation curve

$\varepsilon_y^{\,i}$ = transverse strain at the i^{th} point of the ±45° specimen tensile load deformation curve

b = width of tensile specimen

d = thickness of tensile specimen

The shear stress and shear strain at each data point is calculated using the given formulae, and plotted as shown in Figure 2.6.2. Again, the material response was linear throughout the loading range. *G* could be found from the slope of calculated shear stress vs. calculated shear strain. For this material, the shear modulus was found to be *G* = 2.07 GPa [0.30 MPSi].

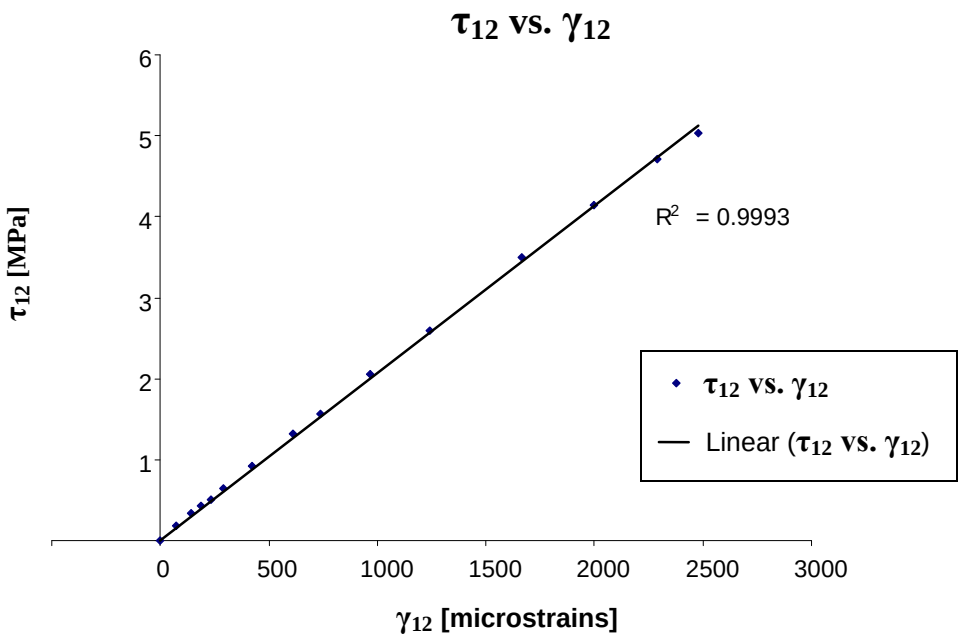

Figure 2.6.2 Shear Stress vs. Shear Strain Plot for Composite

2.7 Fabricating the Bimaterial Specimens

Specimens were created from the raw composite sheets in a series of steps. First the intended shapes of the bimaterial halves were drawn upon the composite sheet with permanent marker, then the halves were cut out with a band saw. A milling machine was then used to machine the band-sawed halves; this was done to get smooth edges and mating surfaces, and also to achieve accurate mating surface angles. Holes for the loading pins were also machined. The machining parameters are given in Appendix D.

To improve interfacial strength, the mating surfaces were silane treated with a mixture of 2 grams of A0700-KG silane for every 100 ml of 95% Ethanol. The mating surfaces were dipped in the mixture, and kept there while gently agitating for at least two minutes. Then the specimens were left to dry for 48 hours before proceeding. A rack of drying specimens is shown in Figure 2.7.1.

Next, the silane-treated halves were wrapped with thin self-adhesive plastic, as illustrated in Figure 2.7.2, to prevent any urethane spillover from bonding to the front or back of the specimen. The intended crack area was covered with Teflon tape, as shown in Figure 2.7.3 which worked well to prevent bonding.

A PVC sheet was then covered with Mylar, and the bimaterial halves were gently clamped onto it with the mating surfaces facing each other, but leaving a gap into which the urethane adhesive could be poured. A principle sketch of this can be seen in Figure 2.7.4, while Figure 2.7.5 shows a photograph of a bimaterial joining setup ready for having urethane poured.

Urethane adhesive (Ultralane 720-LV) was then prepared. . The urethane consists two separate components, “A” and “B” that are the resin and the hardener, respectively. The

two components were mixed together in equal parts. Then the urethane was degassed in a vacuum chamber at -84.4 kPa gage pressure (-25 in. Hg) for 7-8 minutes to remove air bubbles that became introduced during mixing. The urethane was poured in the gap between the mating surfaces, and then the mating surfaces were pushed against each other. The C-clamps were tightened, and small pieces of clay were put on each side of the specimen where the mating surfaces terminated. This prevented urethane from seeping out from the interface region. It was found best not to put the clay in place until after the mating surfaces had been joined, otherwise clay could get in between the mating surfaces and prevent bonding, effectively ruining the specimen.

Figure 2.7.1 Silane-Treated Bimaterial Halves Hanging to Dry

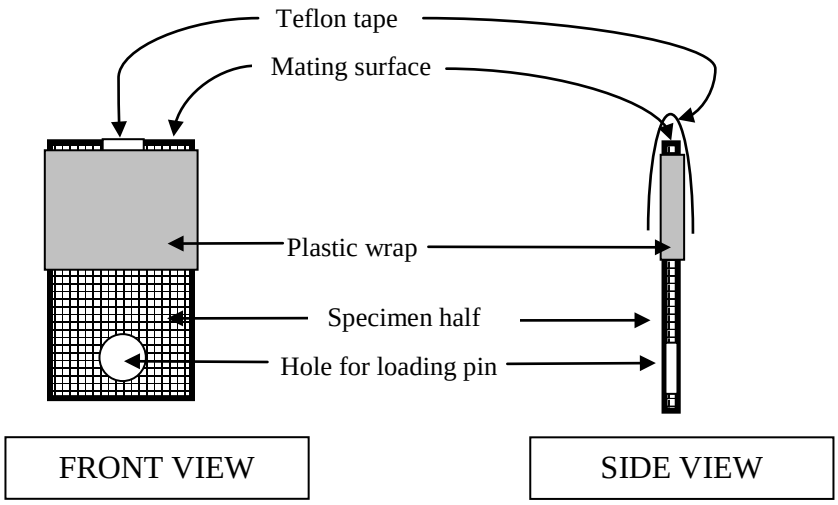

Figure 2.7.2 Preparatory Wrapping of Bimaterial Halves

Figure 2.7.3 Aluminum Bimaterial Half with Mating Surface Partially Covered with Teflon

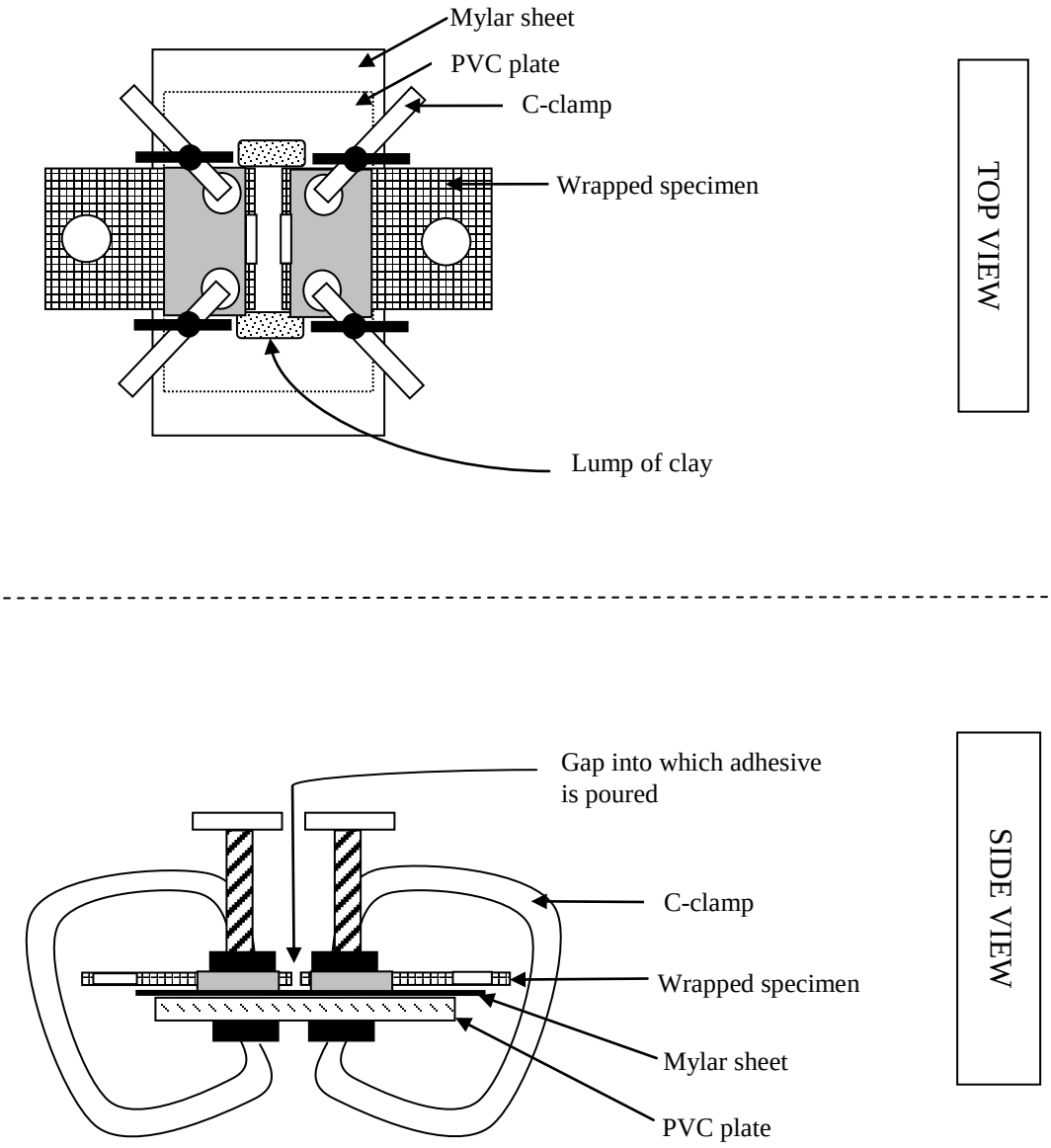

Figure 2.7.4 Principle Sketch of Bimaterial Mating Setup

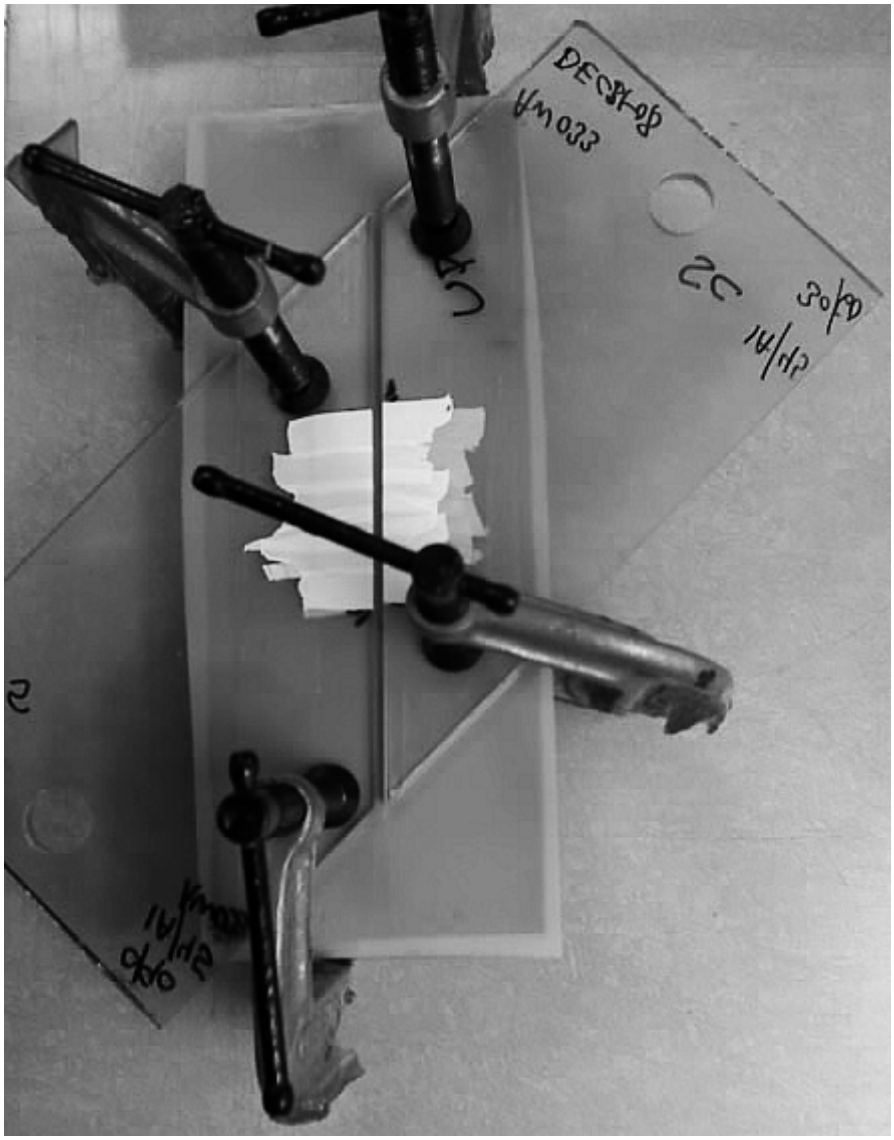

Figure 2.7.5 Photograph of Actual Bimaterial Mating Setup

3 Analytical Methods

3.1 General Methodology

The methodology used was the following: First the fringe orders at many points were obtained from the isochromatic fringe patterns surrounding the crack tip; then the stress-field equations were used in conjunction with the appropriate stress-optic law to determine the stress field. Once the stress field had been determined from the experimentally obtained data, the results were fed back into the stress-optic law in order to numerically *re-generate* a fringe pattern. If the generated fringe pattern qualitatively and quantitatively matched the observed fringe pattern, then the solution was verified and the proposed stress-field equations were considered to have been experimentally verified as shown by Khanna, Ellingsen and Winter [116].

3.2 Data Acquisition

Isochromatic fringe patterns were recorded with a conventional digital imaging system, keeping the load-cell readout visible in the camera's field of view. The fringe patterns were then examined with image software and a number of data points taken, as shown in Figure 3.2.1, where each data point consisted of the fringe order N at that point, and the location (x, y) of the point in the material coordinate system (that is, relative to the crack tip, which is the origin).

Furthermore, each specimen was divided into four *quadrants*. Each quadrant consisted of the area above or below one of the crack tips, as shown in Figure 3.2.2. Thus, four sets of data were acquired, one from each of the four quadrants (Q1, Q2, Q3, and Q4) of the specimen. Each data set was analyzed and verified separately.

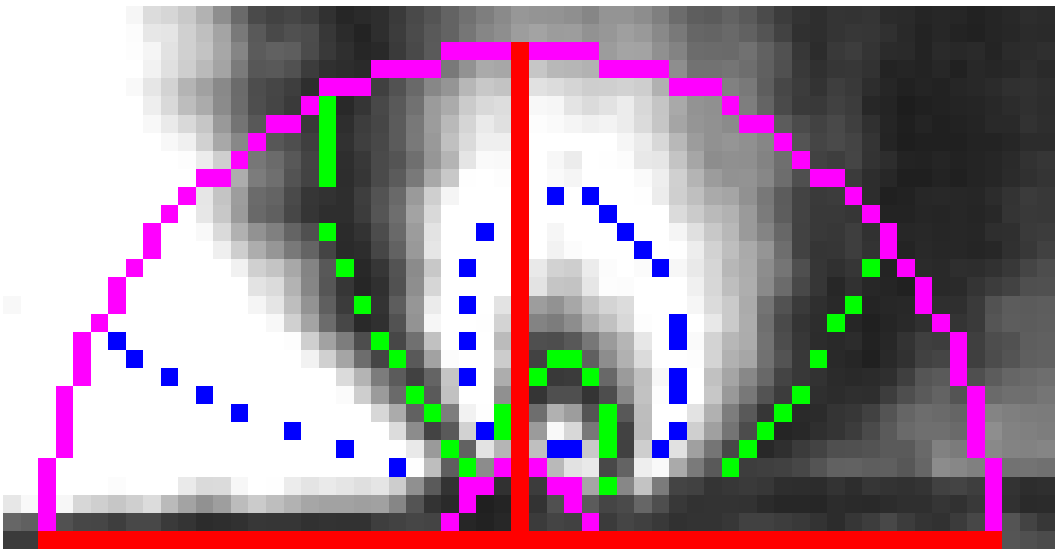

Figure 3.2.1 Data Points Collected from Annular Region Surrounding Crack Tip (First Quadrant)

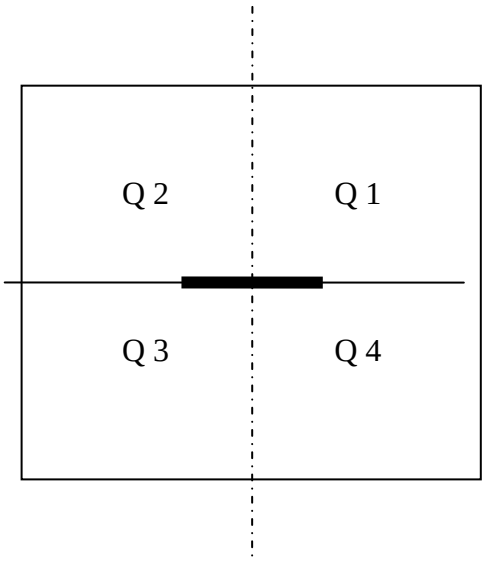

Figure 3.2.2 Specification of Bimaterial Quadrants

3.3 Fringe Multiplication

In some cases a specimen broke before higher order fringes became visible around the interface crack tip, thus yielding only a well-developed first order or fractional order fringe. To increase the amount of information that could be extracted from the photoelastic fringe patterns a fringe multiplication procedure developed in-house was proposed. There does exist a digital fringe multiplication method developed by Chen [123]; that method calculates and generates theoretical fractional fringes. In contrast, the false-color method does not generate any new fringes; it simply uses false color to make the existing fractional fringes more visible.

In brief, the grayscale tones in the experimentally obtained fringe patterns were converted to false colors. The black integer-order fringe was converted to blue; the white half-order fringe was converted to red, and the intermediate fringe orders were converted to green and yellow. Table 1 shows the original fringe order, its original grayscale, and the corresponding false color.

Table 2 False Colors and Their Corresponding Fringe Values

Fringe Order	**Grayscale**	**False Color**
0	**Black**	**Blue**
1/6	Dark Gray	Green
1/3	Pale Gray	Yellow
1/2	**White**	**Red**
2/3	Pale Gray	Yellow
5/6	Dark Gray	Green
1	**Black**	**Blue**
(Sequence repeats for higher fringe orders)		

The conversion to false color yielded several benefits, all of them making fringe interpretation easier. While the intermediate order fringes are indeed present in the original images, it was difficult to distinguish between them; the false colors made them stand out on their own. Also, dividing the patterns into discrete colors made it easier to ensure that data points were taken along the centers of each fringe.

There is an inherent “coarseness” in the images, resulting from the use of woven reinforcement cloth. A smoothing method was implemented to alleviate this coarseness and to ease interpretation of the false-color images. An example of the use of false-color fringe multiplication, and of smoothing, is shown in Figure 3.3.1:

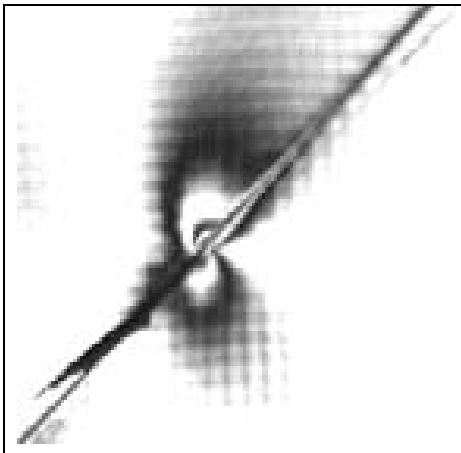	Experimentally obtained isochromatic fringe pattern
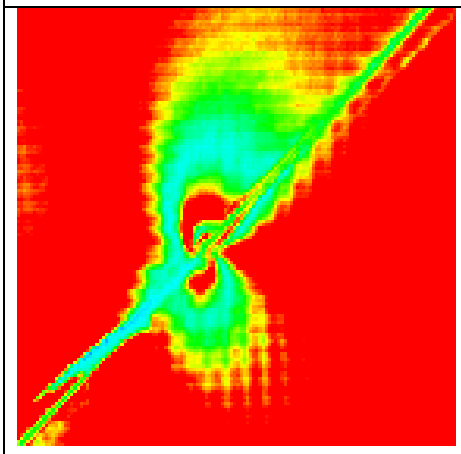	Fringe pattern false-color multiplied, no smoothing
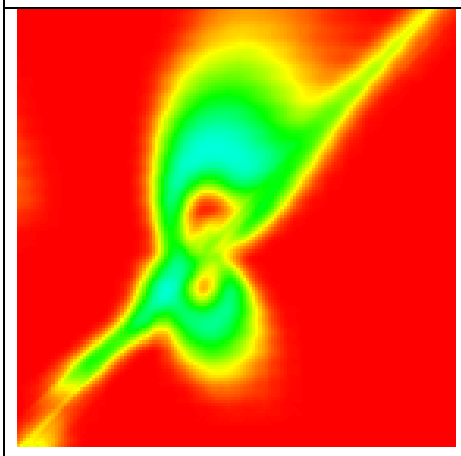	Fringe pattern smoothed and false-color multiplied

Figure 3.3.1 False-Color Fringe Multiplication of Isochromatic Fringes in 0º/90º Composite - 0º/90º Composite Bimaterial with Interface Angle 45º, Load 2.7 kN (600 lb), a/w =0.33, w = 127 mm (5 in.)

It should be noted that this procedure is different from Three-Fringe Photoelasticity (TFP). In TFP, white light is used in the polariscope to obtain a color image (Each primary color of white light produces its own set of isochromatic fringes). The experimentally obtained color image thus has multiple fringe patterns. The color isochromatics are then converted to grayscales with a look-up table that is material-dependent. TFP was developed to automate photoelastic analysis. [124-126].

A problem with using the smoothing algorithm was that it would make the fringes appear slightly shifted relative to the crack tip. This produced problems that are discussed in the crack-tip location section below, and the smoothing part was therefore not used in this investigation.

3.4 Stress Field and Stress-Optic Law

Lee [31], developed static and dynamic stress-field equations for orthotropic/orthotropic bi-materials. Their implemented form is presented below, as is a brief discussion on their development. While the stress-field equations were developed for dynamic cracking, they can also be used for static cases by specifying a very low crack velocity.

Using the stress-optic laws it is possible to relate the observed fringe patterns to the state of stress in the material. In the following treatment, it was assumed that the specimens remain in a plane stress state. This may not hold true for the entire region of the specimens, a region very close to the crack tip may be under a three-dimensional state of stress, and so no data was collected from a small region surrounding the crack tip. Furthermore, far away from the crack tip the stress state becomes dominated by the remotely applied stress and therefore a maximum radius was specified, beyond which no data was collected. To account for these factors an annular region was specified from which data was collected, with an inner diameter equal to one half of the specimen thickness, and an outer diameter equal to two times the specimen thickness.

The presence of oscillatory terms in the stress field equations do have physically inadmissible (that is, impossible) implications, notably overlapping physical regions near the crack tip. However, the general consensus is that any such region will be very small; some argue that the region will be on an atomic size scale. In any case, the use of an annular region avoided the issue of physically impermissible implications of using the oscillatory stress field; the “zone of impermissibility” was already outside the annular region considered for analysis.

In a previous paper [32], Lee outlined the approach used to obtain stress intensity factors and stress fields surrounding the crack tip in the vicinity of a propagating crack in an orthotropic material (i.e. not a bimaterial). Briefly, Lee provided the plane stress components as shown below:

$$\sigma_x = \left[m^2 + \rho c^2 \left(a_{12} - a_{22}\right)\right]\frac{\partial^2 U}{\partial z^2}$$

$$\sigma_y = \left[1 + \rho c^2 \left(a_{12} - a_{11}\right)\right]\frac{\partial^2 U}{\partial z^2} \tag{3.1}$$

$$\tau_{xy} = \left\{-m\left[1 - \rho c^2\left(\frac{a_{22}}{m^2} + a_{11}\right) + \left(\frac{\rho c^2}{m}\right)^2\left(a_{11}a_{22} - a_{12}^2\right)\right]\right\}\frac{\partial U}{\partial z^2}$$

where U is the Airy stress function. Using the stress-strain equations and the strain compatibility equation along with eq. (3.1) Lee wrote the stress function as

$$U(z) = U_1(z_1) + U_2(z_2) + \overline{U_1(z_1)} + \overline{U_2(z_2)} = 2\,\mathrm{Re}\left[U_1(z_1) + U_2(z_2)\right] \tag{3.2}$$

where

$$z_1 = x + m_1 y$$

$$z_2 = x + m_2 y \tag{3.3}$$

$$\overline{z_1} = x - m_1 y$$

$$\overline{z_2} = x - m_2 y$$

Where m_1 and m_2 are the roots of a characteristic equation defined by Lee in reference [32]. Lee then defines new functions ϕ and ψ that were first shown as derivatives of U. However, U was never given, Lee instead gave explicit definitions for ϕ and ψ, thus bypassing the issue of defining an Airy stress function altogether. That is, first ϕ and ψ were given as

$$\phi(z_1) = \frac{dU_1}{dz_1} \ , \ \phi'(z_1) = \left(\frac{d\phi}{dz_1}\right) \tag{3.4}$$

$$\psi(z_2) = \frac{dU_2}{dz_1} \ , \ \psi'(z_2) = \frac{d\psi_2}{dz_1} \tag{3.5}$$

Using eqns. (3.2) and (3.4) and (3.5) the explicit form of the plane stress field can be written as

$$\begin{aligned}
\sigma_x &= 2\,\mathrm{Re}\left\{\left[m_1^2 + \rho c^2\left(a_{12} - a_{22}\right)\right]\phi' + \left[m_2^2 + \rho c^2\left(a_{12} - a_{22}\right)\right]\psi'\right\} \\
\sigma_y &= 2\,\mathrm{Re}\left\{\left[1 + \rho c^2\left(a_{12} - a_{11}\right)\right]\left(\phi' + \psi'\right)\right\} \\
\tau_{xy} &= -2\,\mathrm{Re}\left(\mu_1\phi' + \mu_2\psi'\right)
\end{aligned} \tag{3.6}$$

The analytic complex functions $\varphi(z_1)$ and $\psi(z_2)$ have been defined as a power series shown below (shown in enlarged form for readability)

$$\phi(z_1) = \sum_n A_n z_1^{\lambda_n} = \sum \left(A_n^0 + iA_n^*\right) r_1^{\lambda_n} e^{i\lambda_n\theta_1} \tag{3.7}$$

$$\psi(z_2) = \sum_n B_n z_2^{\lambda_n} = \sum \left(B_n^0 + iB_n^*\right) r_2^{\lambda_n} e^{i\lambda_n\theta_2} \tag{3.8}$$

where

$$\begin{aligned}
A_n^0 &= \mathrm{Re}\left[\frac{-\mu_2}{\sqrt{2\pi}(1+M_1)(\mu_1 - \mu_2)}\right] K_n^0 \\
A_n^* &= \mathrm{Re}\left[i\frac{1}{\sqrt{2\pi}(\mu_1 - \mu_2)}\right] K_n^* \\
B_n^0 &= -h(n) A_n^0 \\
B_n^* &= -h(\bar{n}) A_n^*
\end{aligned} \tag{3.9}$$

$$h(n) = \begin{cases} \mu_1 / \mu_2 & : n \text{ even} \\ 1 & : n \text{ odd} \end{cases} \tag{3.10}$$

$$\bar{n} = n + 1$$

[32] provides further details on each term within these equations. The equations given therein were then developed further for analysis of orthotropic bimaterials.

For an orthotropic bi-material, the oscillatory stress fields having an odd power series (n = 1,3,5,…) were adopted from Lee [31] and Ricci et al. [113] and implemented as shown below:

$$\sigma_x = \sum_{n=odd} \frac{K_n^{\,0}}{2\sqrt{2\pi}D\cosh(\varepsilon\pi)} \begin{bmatrix} (M_b - p^2)\left\{e^{\varepsilon(\pi-\theta_l)}\overline{A}\cos\left(\varepsilon\ln r_l + \frac{n-2}{2}\theta_l\right) + e^{-\varepsilon(\pi-\theta_l)}A\cos\left(\varepsilon\ln r_l - \frac{n-2}{2}\theta_l\right)\right\} r_l^{\left(\frac{n-2}{2}\right)} \\ -(M_b - q^2)\left\{e^{\varepsilon(\pi-\theta_s)}\overline{B}\cos\left(\varepsilon\ln r_s + \frac{n-2}{2}\theta_s\right) + e^{-\varepsilon(\pi-\theta_s)}B\cos\left(\varepsilon\ln r_s - \frac{n-2}{2}\theta_s\right) r_s^{\left(\frac{n-2}{2}\right)}\right\} \end{bmatrix}$$
$$+ \sum_{n=odd} \frac{K_n^{\,*}}{2\sqrt{2\pi}D\cosh(\varepsilon\pi)} \begin{bmatrix} -(M_b - p^2)\left\{e^{\varepsilon(\pi-\theta_l)}\overline{A}\sin\left(\varepsilon\ln r_l + \frac{n-2}{2}\theta_l\right) + e^{-\varepsilon(\pi-\theta_l)}A\sin\left(\varepsilon\ln r_l - \frac{n-2}{2}\theta_l\right)\right\} r_l^{\left(\frac{n-2}{2}\right)} \\ +(M_b - q^2)\left\{e^{\varepsilon(\pi-\theta_s)}\overline{B}\sin\left(\varepsilon\ln r_s + \frac{n-2}{2}\theta_s\right) + e^{-\varepsilon(\pi-\theta_s)}B\sin\left(\varepsilon\ln r_s - \frac{n-2}{2}\theta_s\right) r_s^{\left(\frac{n-2}{2}\right)}\right\} \end{bmatrix}$$

$$\sigma_y = \sum_{n=odd} \frac{K_n^{\,0}}{2\sqrt{2\pi}D\cosh(\varepsilon\pi)} \begin{bmatrix} (1+M_a)\left\{e^{\varepsilon(\pi-\theta_l)}\overline{A}\cos\left(\varepsilon\ln r_l + \frac{n-2}{2}\theta_l\right) + e^{-\varepsilon(\pi-\theta_l)}A\cos\left(\varepsilon\ln r_l - \frac{n-2}{2}\theta_l\right)\right\} r_l^{\left(\frac{n-2}{2}\right)} \\ -(1+M_a)\left\{e^{\varepsilon(\pi-\theta_s)}\overline{B}\cos\left(\varepsilon\ln r_s + \frac{n-2}{2}\theta_s\right) + e^{-\varepsilon(\pi-\theta_s)}B\cos\left(\varepsilon\ln r_s - \frac{n-2}{2}\theta_s\right) r_s^{\left(\frac{n-2}{2}\right)}\right\} \end{bmatrix}$$
$$+ \sum_{n=odd} \frac{K_n^{\,*}}{2\sqrt{2\pi}D\cosh(\varepsilon\pi)} \begin{bmatrix} -(1+M_a)\left\{e^{\varepsilon(\pi-\theta_l)}\overline{A}\sin\left(\varepsilon\ln r_l + \frac{n-2}{2}\theta_l\right) + e^{-\varepsilon(\pi-\theta_l)}A\sin\left(\varepsilon\ln r_l - \frac{n-2}{2}\theta_l\right)\right\} r_l^{\left(\frac{n-2}{2}\right)} \\ +(1+M_b)\left\{e^{\varepsilon(\pi-\theta_s)}\overline{B}\sin\left(\varepsilon\ln r_s + \frac{n-2}{2}\theta_s\right) + e^{-\varepsilon(\pi-\theta_s)}B\sin\left(\varepsilon\ln r_s - \frac{n-2}{2}\theta_s\right) r_s^{\left(\frac{n-2}{2}\right)}\right\} \end{bmatrix}$$

(3.11)

$$\tau_{xy} = \sum_{n=odd} \frac{K_n^{\,0}}{2\sqrt{2\pi}D\cosh(\varepsilon\pi)} \begin{bmatrix} \alpha_l\left\{e^{\varepsilon(\pi-\theta_l)}\overline{A}\sin\left(\varepsilon\ln r_l + \frac{n-2}{2}\theta_l\right) - e^{-\varepsilon(\pi-\theta_l)}A\sin\left(\varepsilon\ln r_l - \frac{n-2}{2}\theta_l\right)\right\} r_l^{\left(\frac{n-2}{2}\right)} \\ +\alpha_s\left\{-e^{\varepsilon(\pi-\theta_s)}\overline{B}\sin\left(\varepsilon\ln r_s + \frac{n-2}{2}\theta_s\right) + e^{-\varepsilon(\pi-\theta_s)}B\sin\left(\varepsilon\ln r_s - \frac{n-2}{2}\theta_s\right) r_s^{\left(\frac{n-2}{2}\right)}\right\} \end{bmatrix}$$
$$+ \sum_{n=odd} \frac{K_n^{\,*}}{2\sqrt{2\pi}D\cosh(\varepsilon\pi)} \begin{bmatrix} \alpha_l\left\{e^{\varepsilon(\pi-\theta_l)}\overline{A}\cos\left(\varepsilon\ln r_l + \frac{n-2}{2}\theta_l\right) - e^{-\varepsilon(\pi-\theta_l)}A\cos\left(\varepsilon\ln r_l - \frac{n-2}{2}\theta_l\right)\right\} r_l^{\left(\frac{n-2}{2}\right)} \\ +\alpha_s\left\{-e^{\varepsilon(\pi-\theta_s)}\overline{B}\cos\left(\varepsilon\ln r_s + \frac{n-2}{2}\theta_s\right) + e^{-\varepsilon(\pi-\theta_s)}B\sin\left(\varepsilon\ln r_s - \frac{n-2}{2}\theta_s\right) r_s^{\left(\frac{n-2}{2}\right)}\right\} \end{bmatrix}$$

where

$$A = \alpha_s + (1 + M_a)\eta$$

$$\overline{A} = \alpha_s - (1 + M_a)\eta$$

$$B = \alpha_l + (1 + M_a)\eta$$

$$\overline{B} = \alpha_l - (1 + M_a)\eta$$

$$B_{12} = \frac{1}{2}\left[2a_{12} + a_{66} + \rho c^2\left({a_{12}}^2 - a_{11}a_{66} - a_{11}a_{22}\right)\right]\frac{1}{a_{11}}$$

$$D_k = \left[(1 + M_a)(\alpha_s - \alpha_l)\right]_k$$

$$h_{11} = (l_{11})_1 - (l_{11})_2$$

$$h_{12} = (l_{12})_1 + (l_{12})_2$$

$$h_{21} = (l_{21})_1 + (l_{21})_2$$

$$K_{66} = \frac{1}{a_{11}}\left\{a_{22} + \rho c^2\left[{a_{12}}^2 - a_{22}a_{66} - a_{11}a_{22} + \rho c^2 a_{66}\left(a_{11}a_{22} - {a_{12}}^2\right)\right]\right\}$$

$$(l_{11})_k = \left\{\frac{p_s\alpha_l - p_l\alpha_s}{D}\right\}_k = \left\{\frac{q_s - q_l}{\alpha_s - \alpha_l}\right\}_k$$

$$(l_{12})_k = \left\{\frac{(1 + M_\alpha)(p_l - p_s)}{D}\right\}_k$$

$$(l_{21})_k = \left\{\frac{\alpha_s q_l - \alpha_l q_s}{D}\right\}_k$$

$$M_a = \rho c^2(a_{12} - a_{11})$$

$$M_b = \rho c^2(a_{12} - a_{22})$$

$$p = \sqrt{B_{12} - \sqrt{{B_{12}}^2 - K_{66}}}$$

$$q = \sqrt{B_{12} + \sqrt{B_{12}{}^2 - K_{66}}}$$

$$r_l = r\sqrt{\cos^2\theta + p^2\sin^2\theta}$$

$$r_s = r\sqrt{\cos^2\theta + q^2\sin^2\theta}$$

$$Z_l = p \quad Z_s = q$$

$$\alpha_l = p + a_{22}\frac{\rho c^2}{p} - p\rho c^2 a_{11} - \frac{\left(\rho c^2\right)^2}{p}\left(a_{11}a_{22} - a_{12}{}^2\right)$$

$$\alpha_s = q + a_{22}\frac{\rho c^2}{q} - q\rho c^2 a_{11} - \frac{\left(\rho c^2\right)^2}{q}\left(a_{11}a_{22} - a_{12}{}^2\right)$$

$$\beta = \frac{h_{11}}{\sqrt{h_{12}h_{21}}}$$

$$\varepsilon = \frac{1}{2\pi}\ln\frac{1-\beta}{1+\beta}$$

$$\theta_l = \arctan\left(Z_l\tan\theta\right)$$

$$\theta_s = \arctan\left(Z_s\tan\theta\right)$$

$$a_{11} = \frac{\cos^4\alpha}{E_L} + \frac{\sin^4\alpha}{E_T}$$

$$a_{12} = -\frac{\nu_{LT}}{E_L}$$

$$a_{22} = \frac{\cos^4\alpha}{E_T} + \frac{\sin^4\alpha}{E_L}$$

$$a_{66} = \frac{1}{\mu_{LT}}$$

a_{ij} are displacement constants, ρ is the density, c is the crack propagation velocity, c_l and c_s are the longitudinal and shear wave velocities of the composite, α is the fiber reinforcement angle with respect to the crack propagation angle, E_L, E_T, G_{LT}, and $v_{LT} = -\varepsilon_T/\varepsilon_L$ are the elastic moduli and Poisson's ratio, respectively. The above are dynamic equations which are also applicable for a static case if a very low crack velocity is assumed. In the odd power series, when n=1, K_n^0 and K_n^* become K_I and K_{II}, respectively, thus the opening mode and shear mode stress intensity factors can be calculated explicitly. Once K_I and K_{II} have been determined, the energy release rate G can be calculated by

$$G = \frac{\left(K_I^2 + K_{II}^2\right)h_{21}}{4\cosh^2(\varepsilon\pi)} \tag{3.12}$$

The observed fringe patterns are related to the mechanical stresses through Sampson's stress-optic law for orthotropic materials [96]:

$$\frac{N^2}{h^2} = \left(\frac{\sigma_L}{f_L} - \frac{\sigma_T}{f_T}\right)^2 + \left(\frac{2\cdot\tau_{LT}}{f_{LT}}\right)^2 \tag{3.13}$$

where N is the observed isochromatic fringe order, σ_L and σ_T are the longitudinal and transverse normal stresses along the two respective principal material directions, τ_{LT} is the shear stress, f_L and f_T are the stress-fringe values of the material in the longitudinal and transverse directions, f_{LT} is the stress-fringe value in shear, and h is the thickness of the specimen.

3.5 Overdeterministic Analysis

3.5.1 Determining the Stress-Intensity Factors

Sanford and Dally [97] outlined the numerical approach for the overdeterministic analysis: If the *exact* stresses and fringe orders at each point were known then both sides of the stress-optic law would equal each other. In practice this is not the case so the *difference* between the two sides has been defined as an error function *g*, written as

$$g = \left(\frac{\sigma_L}{f_L} - \frac{\sigma_T}{f_T} \right)^2 + \left(\frac{2 \cdot \tau_{LT}}{f_{LT}} \right)^2 - \frac{N^2}{h^2} \tag{3.14}$$

There will be one such equation for each data point. As expressed above, the error function *g* determines the difference between the observed fringe order at each point, and what the calculated fringe order at that point should be. The calculated fringe order is determined on the basis of the calculated stresses at that point and the coordinates of the point. The system is said to be overdeterministic because the number of simultaneous equations is higher than the number of unknowns. An iterative approach was used to solve the system of equations, where *g* should decrease with each successive iteration. Once *g* comes sufficiently close to zero the calculated and observed fringe orders are virtually equal. The expression used to calculate the fringe order contains the calculated stress fields, and so the stress fields can be extracted from the above equations.

The system of equations is represented in matrix form as

$$[g] = [c] \cdot [\Delta] \tag{3.15}$$

where

$$[g]=\begin{bmatrix}-g_1\\-g_2\\\cdots\\-g_K\end{bmatrix}\quad[\Delta]=\begin{bmatrix}\Delta K_1^0\\\cdots\\\Delta K_n^0\\\Delta K_1^*\\\cdots\\\Delta K_n^*\end{bmatrix}\quad[c]=\begin{bmatrix}\frac{\partial g_1}{\partial K_1^0} & \cdots & \frac{\partial g_1}{\partial K_n^0} & \frac{\partial g_1}{\partial K_1^*} & \cdots & \frac{\partial g_1}{\partial K_n^*}\\ \cdots & \cdots & \cdots & \cdots & \cdots & \cdots\\ \cdots & \cdots & \cdots & \cdots & \cdots & \cdots\\ \frac{\partial g_K}{\partial K_1^0} & \cdots & \frac{\partial g_K}{\partial K_n^0} & \frac{\partial g_K}{\partial K_1^*} & \cdots & \frac{\partial g_K}{\partial K_n^*}\end{bmatrix} \tag{3.16}$$

$k = 0,1,..K$ where K is the number of data points. The coefficient matrix [c] contains partial derivatives of g with respect to the unknown quantities K_n^0 and K_n^*. There is one row for each data point, and one column for each unknown coefficient. The stress intensity factors near the crack tip are the quantities K_1^0 and K_1^*, where $K_1^0 = K_I$ and $K_1^* = K_{II}$ (when n = 1.) The correction matrix [Δ] contains the corrections for the values of the unknown quantities. An initial guess is needed for the iterative method; the difference in the calculated values from one iteration to the next is applied to the quantities by

$$\left(K_1^0\right)_{i+1} = K_{1\,i}^0 + \Delta K_{1\,i}^0 \tag{3.17}$$

this applies to all the unknown quantities.

For ease of implementation of this method one can rewrite [Δ] as

$$[\Delta] = [d]^{-1}\,[c]^{\mathrm{T}}\,[g] \qquad \text{where} \quad [d] = [c]^{\mathrm{T}}\,[c] \tag{3.18}$$

The algorithm behind this method can be broken down into the following steps:

1) Select a data acquisition region
2) Collect a number of data points *(x, y, N)*
3) Assume initial values for unknowns K_1^0 .. K_n^0 , K_1^* .. K_n^*
4) Compute elements of matrices [g] and [c] for each data point
5) Compute [Δ]
6) Revise initial estimates of K_1^0 .. K_n^0 , K_1^* .. K_n^* in equation (3.16)

Repeat until [Δ] becomes reasonably small.

The overdeterministic method as well as the image regeneration procedure was implemented in a mathematical software program called Maple 11, which works well for implementing systems of very large equations. Typically 60-100 data points were used and 20 iterations were performed. With a two-term odd power series the iterative calculations took about 60 seconds to complete on an Intel Core 2 computer system. Though for common calculations 20 iterations are completed in a moment on a modern computer system, the equations in question were very computationally intensive. The subsequent full-size image regeneration took somewhat longer, 2-3 minutes. This was reasonable considering the image matrix contains 90 thousand elements (for a 300 by 300 pixel image) that were individually calculated, again using a system of very large equations.

3.5.2 Fringe Regeneration

Once the experimentally obtained fringe pattern had been analyzed, the solution was verified by mathematically *regenerating* the fringe pattern that was used for analysis. This was done by inserting the now *known* coefficients into the stress-optic law and plotting this across a grid overlaying the analyzed area.

$$N = \left(\left[\left(\frac{\sigma_L}{f_L} - \frac{\sigma_T}{f_T} \right)^2 + \left(\frac{2 \cdot \tau_{LT}}{f_{LT}} \right)^2 \right] h^2 \right)^{\frac{1}{2}} \qquad (3.19)$$

Equation 3.17 was solved for each grid point. A fringe value was obtained for each grid point and a corresponding grayscale value was assigned to that point. The assignment of grayscales was the same as that of Table 1 (That is, which grayscale to generate for which fringe order). After calculating fringe values (and thus grayscales) for the entire grid, a fringe pattern had been obtained which was then compared to the

experimental pattern. The area considered was the annular region surrounding the crack tip. Features compared were the fringe order, size, and orientation of the fringes. Most experimental patterns had a “large” and “small” integer order fringe present. The regenerated patterns were examined to see that the large fringe was generated in the correct size, and that the small fringe was generated at a correct size and orientation.

If the experimental and regenerated fringe patterns showed good agreement, the solution was considered verified.

3.5.2.1 Some Concerns Regarding Fringe Regeneration

The odd oscillatory series give K_I and K_{II} explicitly when $n = 1$. Specifying a higher n will result in more terms, which could intuitively be assumed to give better accuracy in the analysis and regeneration. This, however, was not found to be the case for the specimens that were tested. Figure 3.5.1 illustrates this issue:

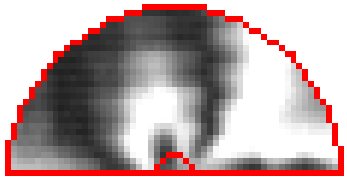

Experimental fringe pattern
Specimen: 2nd quadrant of 0°/90°-0°/90°
$a/w = 0.17$, $P = 2.4$ kN

n = 1, 2 terms (as used throughout)
(K_1^0, K_1^*)

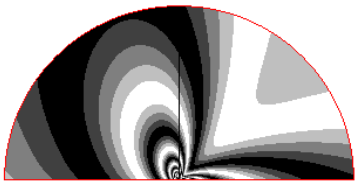

$K_I = 0.88 \cdot 10^6 \,\mathrm{Pa}\sqrt{\mathrm{m}}$
$K_{II} = -0.47 \cdot 10^6 \,\mathrm{Pa}\sqrt{\mathrm{m}}$
$G = 30.4 J/m^2$

n = 2 (truncated), 3 terms
(K_1^0, K_3^0, K_1^*)

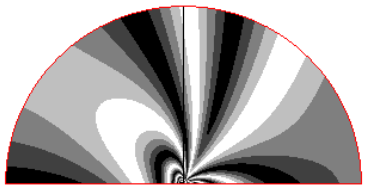

$K_I = 0.96 \cdot 10^6 \,\mathrm{Pa}\sqrt{\mathrm{m}}$
$K_{II} = -0.28 \cdot 10^6 \,\mathrm{Pa}\sqrt{\mathrm{m}}$
$G = 30.7 J/m^2$

n = 2, 4 terms
$(K_1^0, K_3^0, K_1^*, K_3^*)$

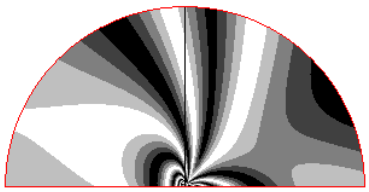

$K_I = 1.00 \cdot 10^6 \,\mathrm{Pa}\sqrt{\mathrm{m}}$
$K_{II} = -0.30 \cdot 10^6 \,\mathrm{Pa}\sqrt{\mathrm{m}}$
$G = 33.2 J/m^2$

n = 3 (truncated), 5 terms
$(K_1^0, K_3^0, K_5^0, K_1^*, K_3^*)$

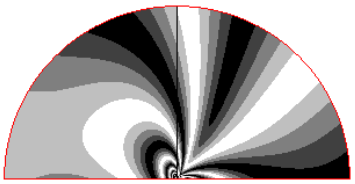

$K_I = 0.90 \cdot 10^6 \,\mathrm{Pa}\sqrt{\mathrm{m}}$
$K_{II} = -0.34 \cdot 10^6 \,\mathrm{Pa}\sqrt{\mathrm{m}}$
$G = 28.6 J/m^2$

Figure 3.5.1 Effect of Increasing the Number of Terms in Stress-Field Equations

The calculated stress intensity factors and energy release rate remained largely correct, but as can be seen, the fringe patterns were regenerated incorrectly when $n \geq 2$. False fringes become increasingly present as the number of terms increases, along with an increasing degree of malformation.

Another important issue was the proper location of the crack tip, that is, the origin of the fringe patterns. If the crack tip location was not determined properly, the analysis and regeneration procedure would yield incorrect results and images, as is demonstrated in Figure 3.5.2. Incorrect crack tip locations would result in varying degrees of malformed fringes, along with incorrect stress intensity factors. This turned out to be a major confounding factor in the analysis of the isochromatic fringe patterns, and it was very time-consuming to deal with.

The crack tip location could be tentatively identified from the images, but not with enough accuracy to avoid the issues mentioned above. A large set of fringe patterns had to be regenerated; one set was generated for each point in a grid overlaying the area surrounding the crack tip. Typically 289 (17^2) fringe patterns were regenerated. Then each one was compared to the experimentally obtained pattern. Once a correctly regenerated fringe pattern had been found for one quadrant, say Quadrant 1, then the same offset was used to generate a fringe pattern for the opposing quadrant, in this case Quadrant 4. Typically, once a good fringe pattern had been regenerated for Quadrant 1 the fringe pattern generated for the opposing quadrant (Quadrant 4) also turned out well when using the same offset that gave a gave a good regenerated pattern in Quadrant 1.

Thus, for each bimaterial specimen, for two of the specimen quadrants 289 fringe patterns had to be regenerated and compared to the experimentally obtained isochromatic

fringe patterns, for each load that was to be investigated. A further two patterns was then generated for the remaining two quadrants. In sum, at least 580 fringe patterns were regenerated and manually compared to experimentally obtained fringe patterns, for each specimen.

Such high sensitivity to correctly locating the crack tip was not encountered in the investigation by Khanna, Ellingsen, and Winter [116]. In that investigation the Westergaard method for crack analysis was used; starting with an Airy stress function in conjunction with complex variables (of the type $z = x + iy$), stress field equations were developed. These contained a user-selectable number of unknown coefficients. Most of these coefficients did not have a physical meaning, but adding them increased the accuracy of the method.

	x = -1 mm	x = 0	x = +1mm
y = +1 mm	Evaluation: Fringes completely malformed	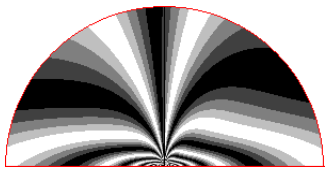 Evaluation: Fringes completely malformed	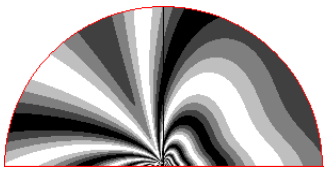 Evaluation: Fringes very malformed
y =0	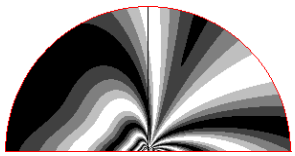 Evaluation: Fringes not well formed, oriented incorrectly	1st Quadrant (0°/90°) 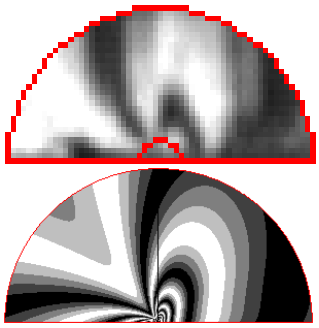 Evaluation: Fringes well formed, oriented correctly, with proper size compared to experimental pattern	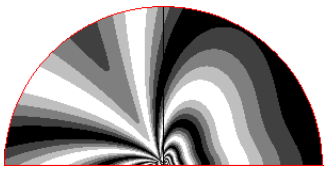 Evaluation: Fringes oriented correctly, but not well formed
y = -1 mm	Evaluation: Fringes completely malformed	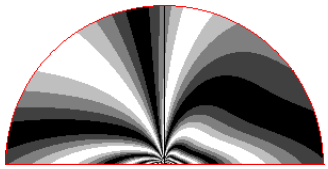 Evaluation: Fringes completely malformed	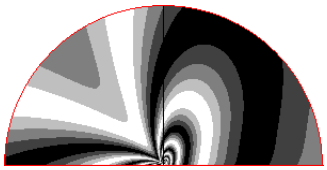 Evaluation: Fringes well formed and correct orientation, but too small compared to experimental pattern

Figure 3.5.2 Effect of Incorrectly Locating Crack Tip

4 Results and Discussion

4.1 Mode-I Fracture (Horizontal Interface)

The K_I and K_{II} values were calculated based on the methodology described above, using a two-term odd power series, that is n=1 .It was found that regenerating patterns for a large annular region was more time consuming and produced erroneous results. As stated above, the reason for using an annular region is that very near the crack tip the stress state is three-dimensional, and the plane stress assumption is no longer valid. Far away from the crack tip, the stress field is dominated by the remotely applied stress rather than the effect of the stress concentration around the crack tip. For these reasons, data was collected only from a region with an outer diameter of 2t and inner diameter of 0.5t, which is also what was regenerated. Several representative calculations are shown next; Figure 4.1.1 - Figure 4.1.8 show the experimentally obtained patterns that were used for analysis, the resulting stress-intensity factors, and the mathematically regenerated patterns. Figure 4.1.9 to Figure 4.1.12 show graphical summaries of the results. Finally, some fracture surfaces were examined with a metallurgical microscope.

It may be noted that the apparent grainy and coarse nature of the fringe pattern has two causes: The reinforcement used was a woven glass cloth, which added a lot of “texture” to the fringe patterns. In addition, the resolution of the digital imaging system was 1020 by 1020 pixels. The annular region was small compared to the overall specimen size so the magnification became large when looking at the annular region, and comparatively few pixels cover this region.

2nd Quadrant	**1st Quadrant**
Aluminum – no fringe pattern	Aluminum – no fringe pattern
3rd Quadrant	**4th Quadrant**
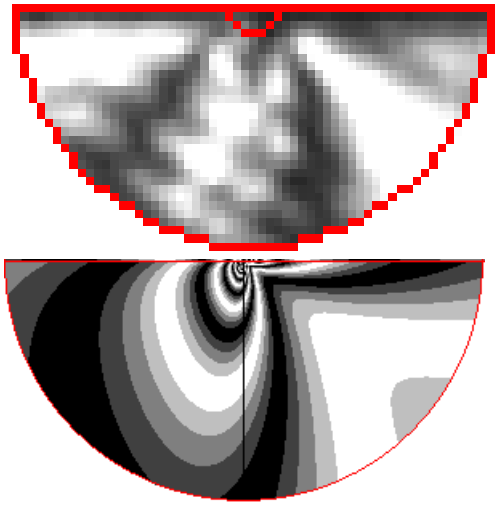 $K_I = 0.82 \cdot 10^6 \, \text{Pa}\sqrt{\text{m}}$ $K_{II} = 0.52 \cdot 10^6 \, \text{Pa}\sqrt{\text{m}}$ $G = 21.2 J / m^2$	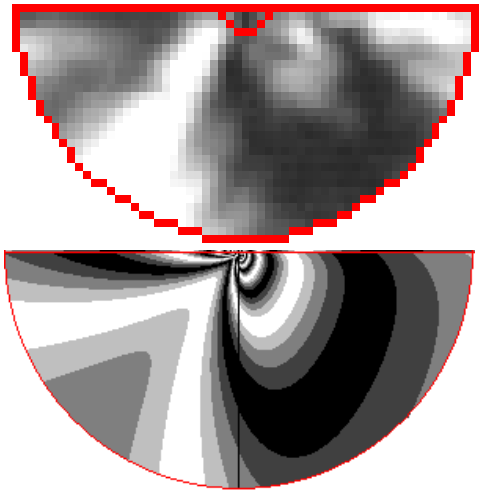 $K_I = 0.83 \cdot 10^6 \, \text{Pa}\sqrt{\text{m}}$ $K_{II} = -0.37 \cdot 10^6 \, \text{Pa}\sqrt{\text{m}}$ $G = 18.5 J / m^2$

Figure 4.1.1 Aluminum –30°/60° Composite Bimaterial, 2 kN (450 lb) Load, a/w = 0.33, w = 76 mm (3.0 in)

2nd Quadrant (0°/90°)

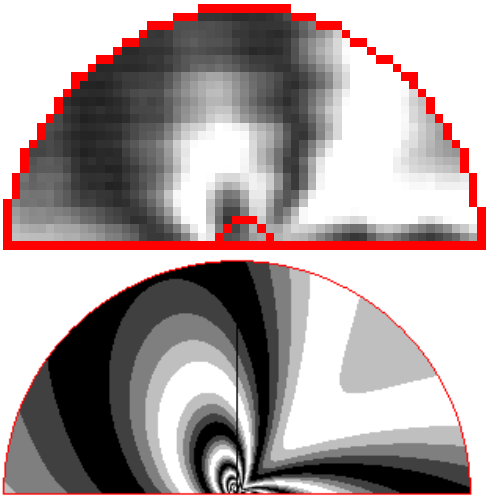

$K_I = 0.88 \cdot 10^6 \text{ Pa}\sqrt{\text{m}}$

$K_{II} = -0.47 \cdot 10^6 \text{ Pa}\sqrt{\text{m}}$

$G = 30.4 J/m^2$

1st Quadrant (0°/90°)

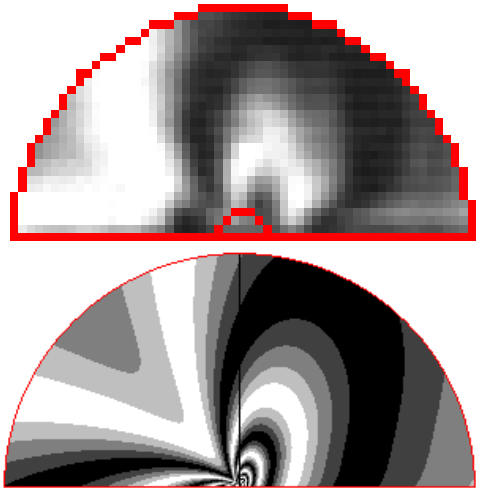

$K_I = 0.90 \cdot 10^6 \text{ Pa}\sqrt{\text{m}}$

$K_{II} = 0.40 \cdot 10^6 \text{ Pa}\sqrt{\text{m}}$

$G = 29.9 J/m^2$

3rd Quadrant (0°/90°)

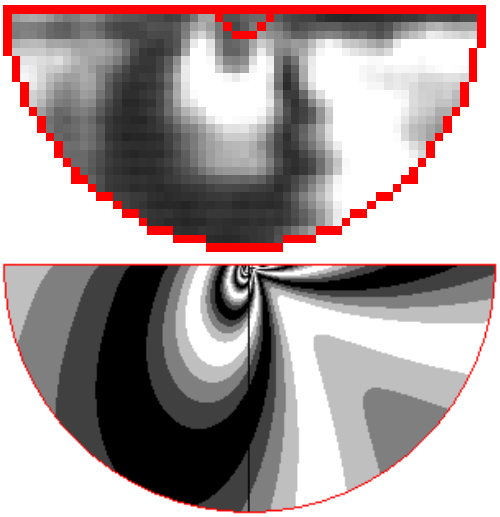

$K_I = 0.81 \cdot 10^6 \text{ Pa}\sqrt{\text{m}}$

$K_{II} = 0.39 \cdot 10^6 \text{ Pa}\sqrt{\text{m}}$

$G = 25.0 J/m^2$

4th Quadrant (0°/90°)

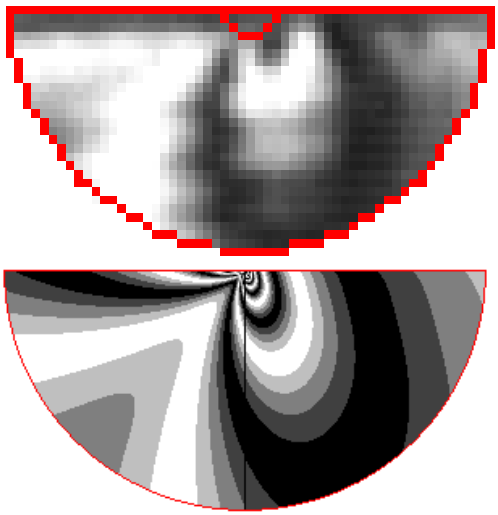

$K_I = 0.87 \cdot 10^6 \text{ Pa}\sqrt{\text{m}}$

$K_{II} = -0.40 \cdot 10^6 \text{ Pa}\sqrt{\text{m}}$

$G = 28.3 J/m^2$

Figure 4.1.2 0°/90° Composite - 0°/90° Composite Bimaterial, 2.7 kN (600 lb) Load, a/w = 0.17, w = 76 mm (3.0 in)

2nd Quadrant (0°/90°)

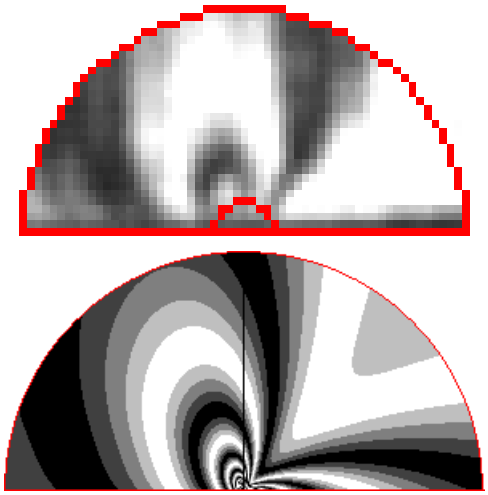

$K_I = 1.04 \cdot 10^6 \text{ Pa}\sqrt{\text{m}}$

$K_{II} = -0.50 \cdot 10^6 \text{ Pa}\sqrt{\text{m}}$

$G = 40.8 J/m^2$

1st Quadrant (0°/90°)

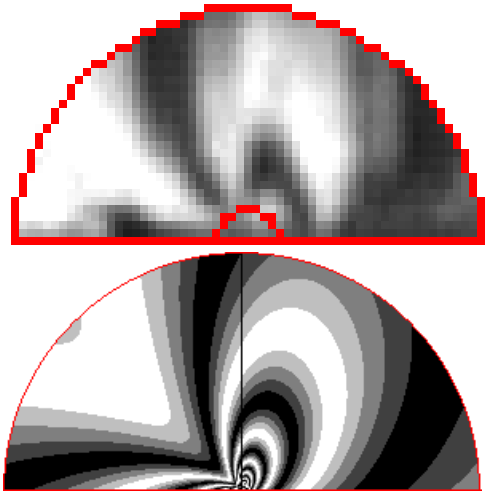

$K_I = 0.96 \cdot 10^6 \text{ Pa}\sqrt{\text{m}}$

$K_{II} = 0.55 \cdot 10^6 \text{ Pa}\sqrt{\text{m}}$

$G = 37.5 J/m^2$

3rd Quadrant (0°/90°)

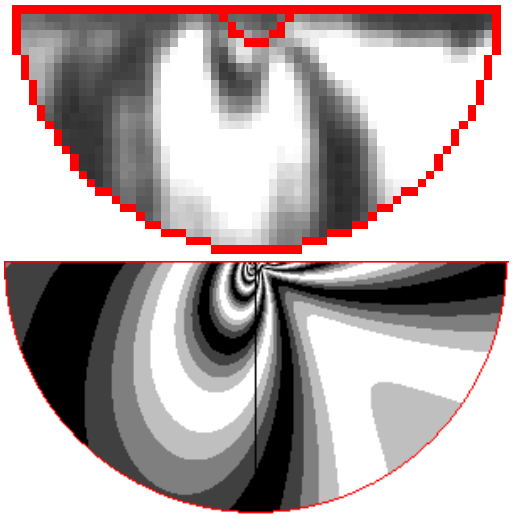

$K_I = 1.03 \cdot 10^6 \text{ Pa}\sqrt{\text{m}}$

$K_{II} = 0.50 \cdot 10^6 \text{ Pa}\sqrt{\text{m}}$

$G = 40.1 J/m^2$

4th Quadrant (0°/90°)

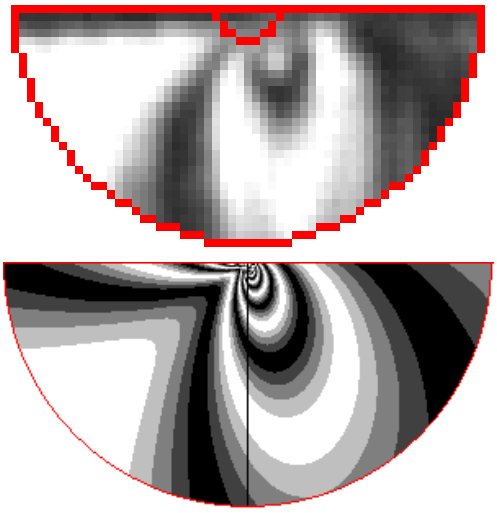

$K_I = 0.91 \cdot 10^6 \text{ Pa}\sqrt{\text{m}}$

$K_{II} = -0.58 \cdot 10^6 \text{ Pa}\sqrt{\text{m}}$

$G = 35.9 J/m^2$

Figure 4.1.3 0°/90° Composite - 0°/90° Composite Bimaterial, 2.7 kN (600 lb) Load, a/w = 0.25, w = 76 mm (3.0 in)

2nd Quadrant (0°/90°)	1st Quadrant (0°/90°)
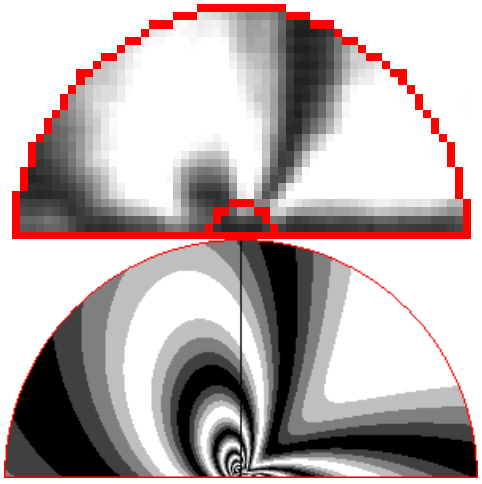	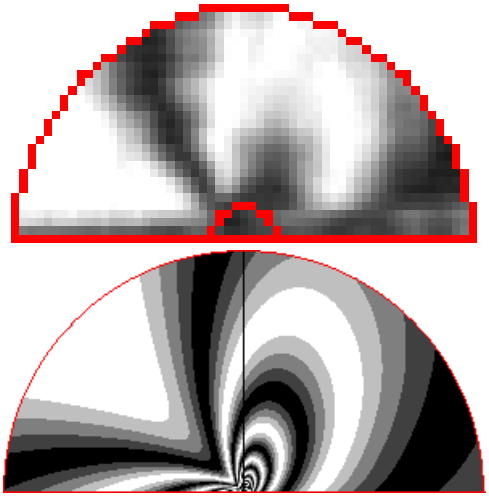
$K_I = 1.00 \cdot 10^6 \text{ Pa}\sqrt{\text{m}}$ $K_{II} = -0.59 \cdot 10^6 \text{ Pa}\sqrt{\text{m}}$ $G = 41.2 J/m^2$	$K_I = 1.04 \cdot 10^6 \text{ Pa}\sqrt{\text{m}}$ $K_{II} = 0.58 \cdot 10^6 \text{ Pa}\sqrt{\text{m}}$ $G = 43.4 J/m^2$
3rd Quadrant (0°/90°)	**4th Quadrant (0°/90°)**
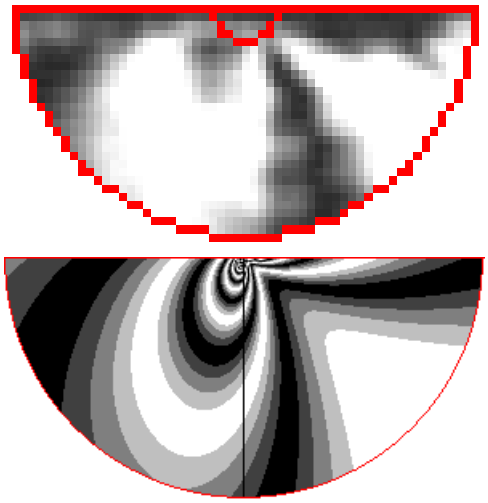	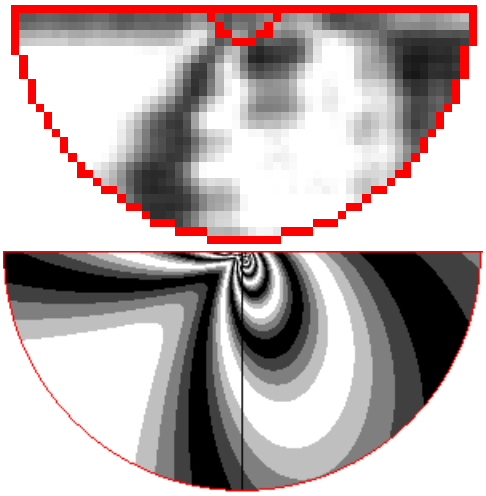
$K_I = 0.97 \cdot 10^6 \text{ Pa}\sqrt{\text{m}}$ $K_{II} = 0.58 \cdot 10^6 \text{ Pa}\sqrt{\text{m}}$ $G = 38.8 J/m^2$	$K_I = 0.97 \cdot 10^6 \text{ Pa}\sqrt{\text{m}}$ $K_{II} = -0.57 \cdot 10^6 \text{ Pa}\sqrt{\text{m}}$ $G = 39.3 J/m^2$

Figure 4.1.4 0°/90° Composite - 0°/90° Composite Bimaterial, 2.7 kN (600 lb) Load, a/w = 0.33, w = 76 mm (3.0 in)

2nd Quadrant (0°/90°)

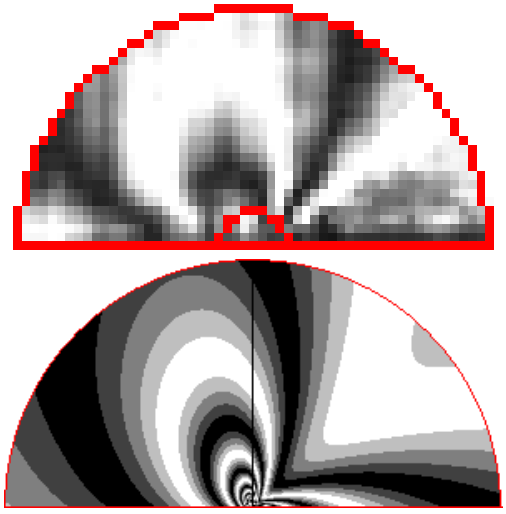

$K_I = 0.88 \cdot 10^6 \, \text{Pa}\sqrt{\text{m}}$

$K_{II} = -0.53 \cdot 10^6 \, \text{Pa}\sqrt{\text{m}}$

$G = 32.1 J / m^2$

1st Quadrant (0°/90°)

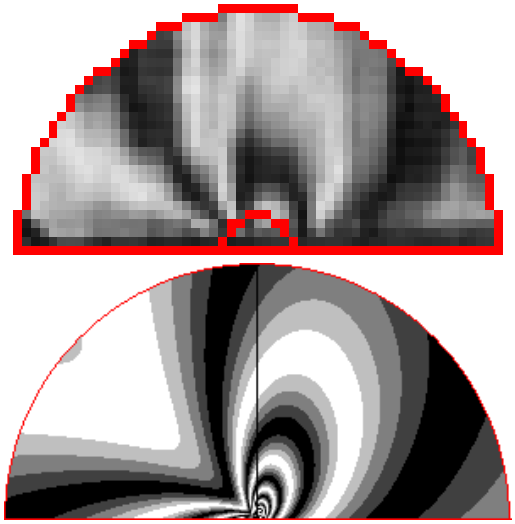

$K_I = 0.91 \cdot 10^6 \, \text{Pa}\sqrt{\text{m}}$

$K_{II} = 0.55 \cdot 10^6 \, \text{Pa}\sqrt{\text{m}}$

$G = 34.5 J / m^2$

3rd Quadrant (0°/90°)

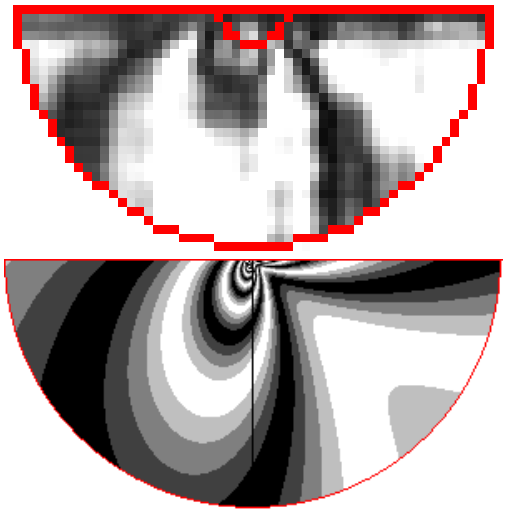

$K_I = 0.88 \cdot 10^6 \, \text{Pa}\sqrt{\text{m}}$

$K_{II} = 0.50 \cdot 10^6 \, \text{Pa}\sqrt{\text{m}}$

$G = 31.7 J / m^2$

4th Quadrant (0°/90°)

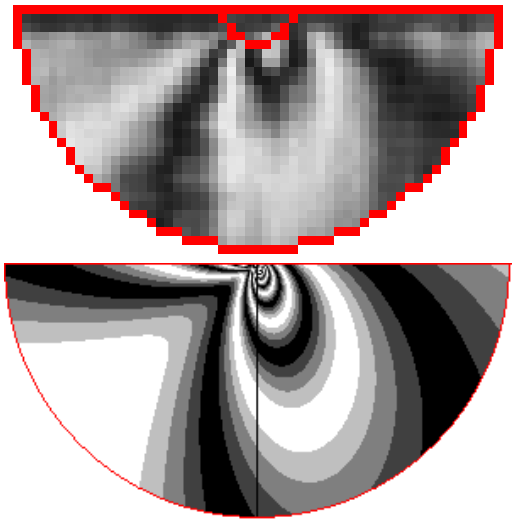

$K_I = 0.84 \cdot 10^6 \, \text{Pa}\sqrt{\text{m}}$

$K_{II} = -0.56 \cdot 10^6 \, \text{Pa}\sqrt{\text{m}}$

$G = 31.1 J / m^2$

Figure 4.1.5 0°/90° Composite - 0°/90° Composite Bimaterial, 2.7 kN (600 lb) Load, a/w = 0.5, w = 121 mm (4.75 in)

2nd Quadrant (0°/90°)

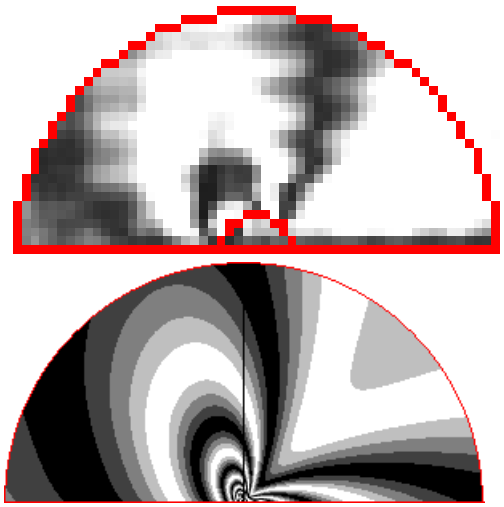

$K_I = 1.01 \cdot 10^6 \, \text{Pa}\sqrt{\text{m}}$

$K_{II} = 0.50 \cdot 10^6 \, \text{Pa}\sqrt{\text{m}}$

$G = 39.2 J / m^2$

1st Quadrant (0°/90°)

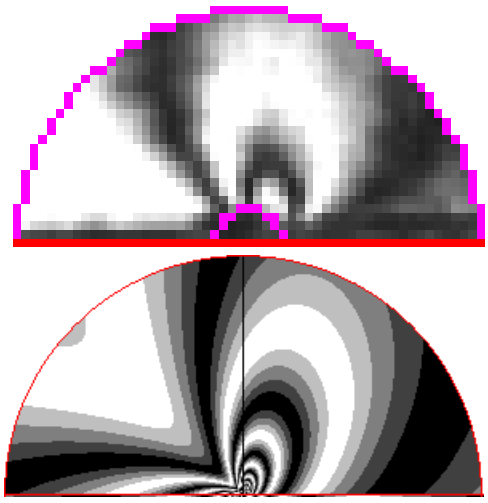

$K_I = 1.00 \cdot 10^6 \, \text{Pa}\sqrt{\text{m}}$

$K_{II} = 0.58 \cdot 10^6 \, \text{Pa}\sqrt{\text{m}}$

$G = 40.1 J / m^2$

3rd Quadrant (15°/75°)

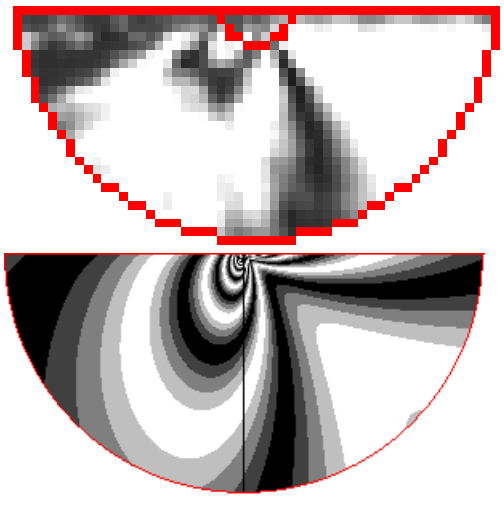

$K_I = 1.08 \cdot 10^6 \, \text{Pa}\sqrt{\text{m}}$

$K_{II} = 0.58 \cdot 10^6 \, \text{Pa}\sqrt{\text{m}}$

$G = 42.0 J / m^2$

4th Quadrant (15°/75°)

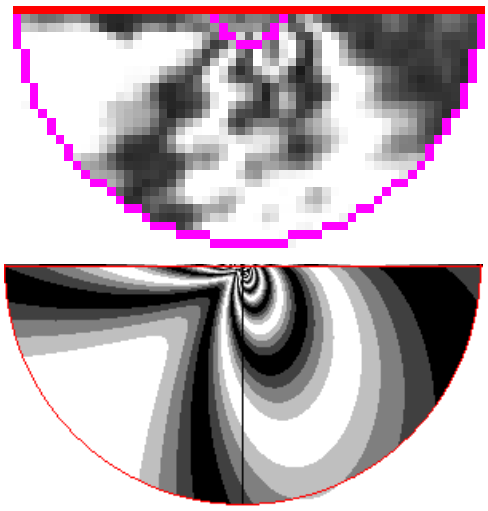

$K_I = 1.04 \cdot 10^6 \, \text{Pa}\sqrt{\text{m}}$

$K_{II} = -0.58 \cdot 10^6 \, \text{Pa}\sqrt{\text{m}}$

$G = 39.6 J / m^2$

Figure 4.1.6 0°/90° Composite - 15°/75° Composite Bimaterial, 2.7 kN (600 lb) Load, a/w = 0.33, w = 76 mm (3.0 in)

2nd Quadrant (0°/90°)

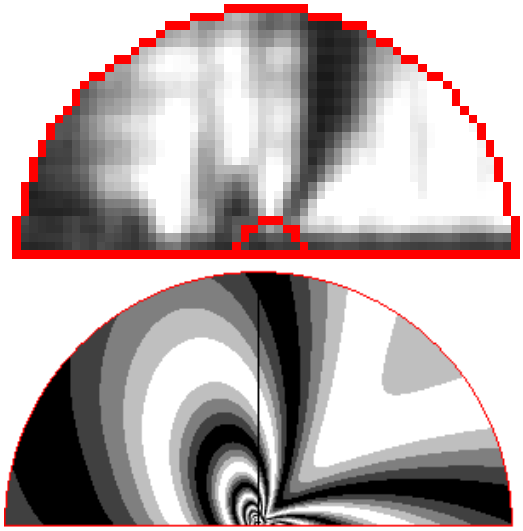

$K_I = 1.08 \cdot 10^6 \text{ Pa}\sqrt{\text{m}}$

$K_{II} = -0.52 \cdot 10^6 \text{ Pa}\sqrt{\text{m}}$

$G = 44.0 J/m^2$

1st Quadrant (0°/90°)

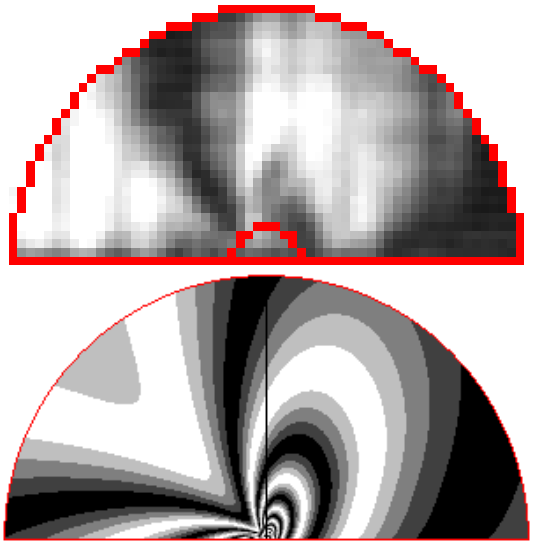

$K_I = 1.08 \cdot 10^6 \text{ Pa}\sqrt{\text{m}}$

$K_{II} = 0.52 \cdot 10^6 \text{ Pa}\sqrt{\text{m}}$

$G = 44.0 J/m^2$

3rd Quadrant (30°/60°)

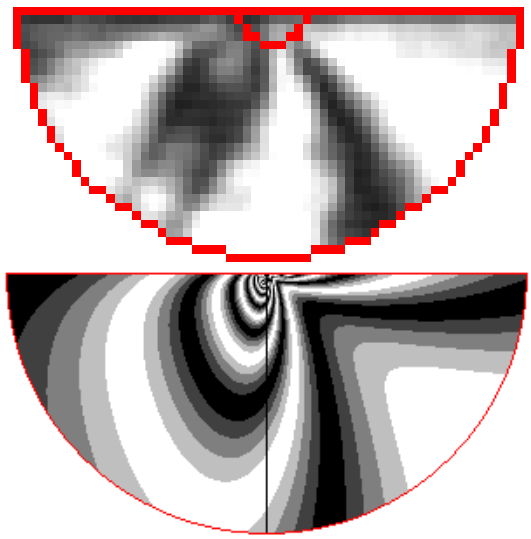

$K_I = 1.06 \cdot 10^6 \text{ Pa}\sqrt{\text{m}}$

$K_{II} = 0.67 \cdot 10^6 \text{ Pa}\sqrt{\text{m}}$

$G = 35.3 J/m^2$

4th Quadrant(30°/60°)

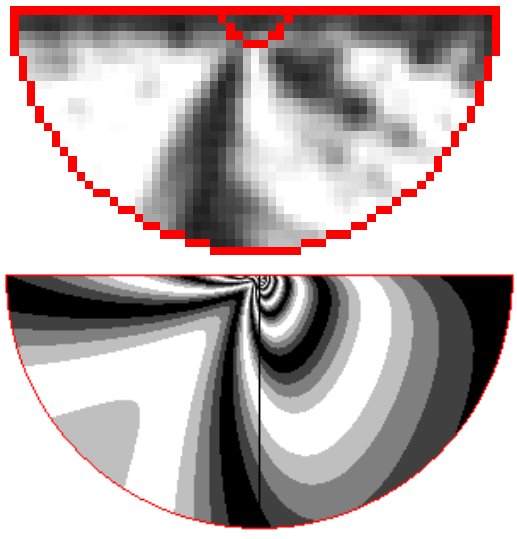

$K_I = 1.10 \cdot 10^6 \text{ Pa}\sqrt{\text{m}}$

$K_{II} = -0.53 \cdot 10^6 \text{ Pa}\sqrt{\text{m}}$

$G = 33.8 J/m^2$

Figure 4.1.7 0°/90° Composite - 30°/60° Composite Bimaterial, 2.7 kN (600 lb) Load, a/w = 0.33, w = 76 mm (3.0 in)

2nd Quadrant (0°/90°)

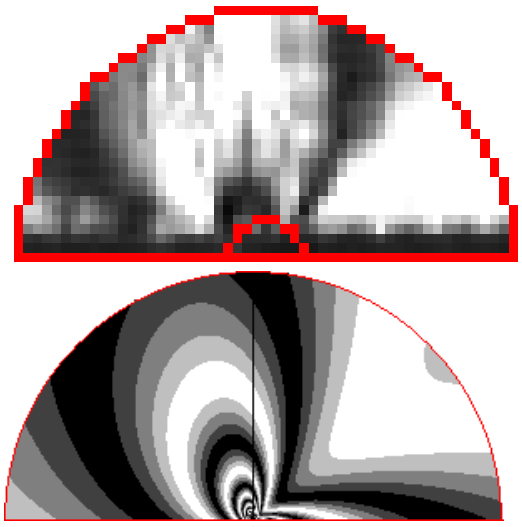

$K_I = 0.77 \cdot 10^6 \text{Pa}\sqrt{\text{m}}$

$K_{II} = -0.52 \cdot 10^6 \text{Pa}\sqrt{\text{m}}$

$G = 26.6 J / m^2$

1st Quadrant (0°/90°)

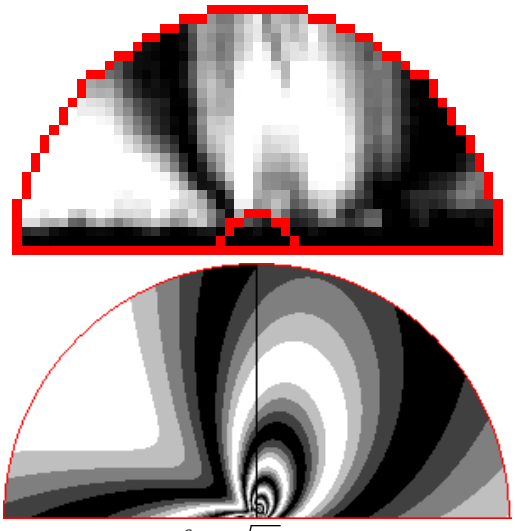

$K_I = 0.72 \cdot 10^6 \text{Pa}\sqrt{\text{m}}$

$K_{II} = 0.55 \cdot 10^6 \text{Pa}\sqrt{\text{m}}$

$G = 24.9 J / m^2$

3rd Quadrant (±45°)

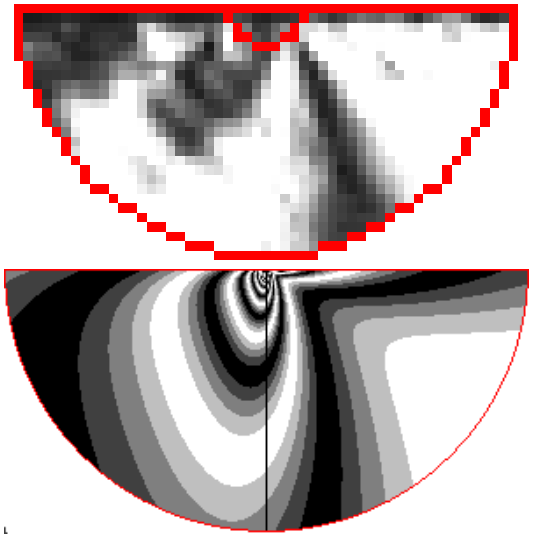

$K_I = 0.75 \cdot 10^6 \text{Pa}\sqrt{\text{m}}$

$K_{II} = 0.61 \cdot 10^6 \text{Pa}\sqrt{\text{m}}$

$G = 18.5 J / m^2$

4th Quadrant (±45°)

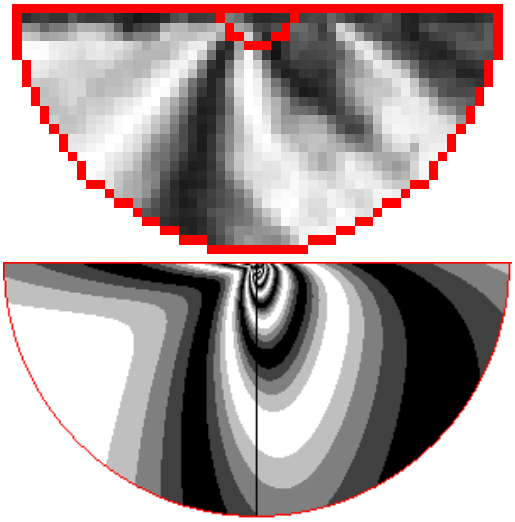

$K_I = 0.60 \cdot 10^6 \text{Pa}\sqrt{\text{m}}$

$K_{II} = -0.60 \cdot 10^6 \text{Pa}\sqrt{\text{m}}$

$G = 14.2 J / m^2$

Figure 4.1.8 0°/90° Composite - 45°/45° Composite Bimaterial, 3.3 kN (750 lb) Load, a/w = 0.33, w = 152 mm (6.0 in)

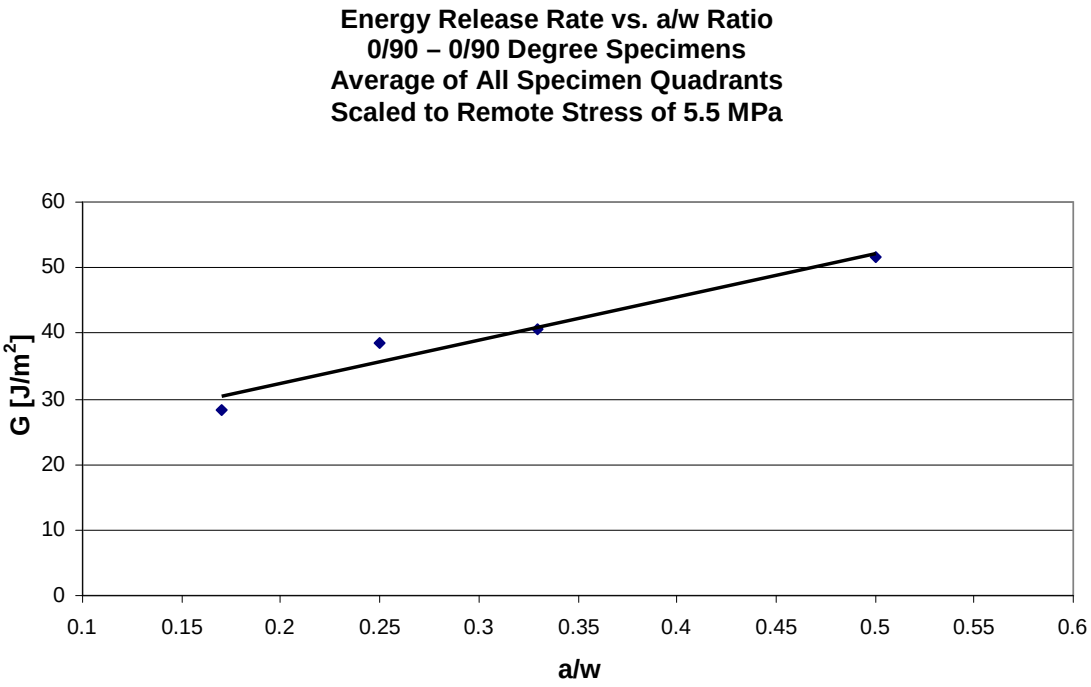

Figure 4.1.9 Energy Release Rate G vs. a/w for Specimens with Reinforcement Directions 0°/90° in Both Halves. Values are averaged for all four

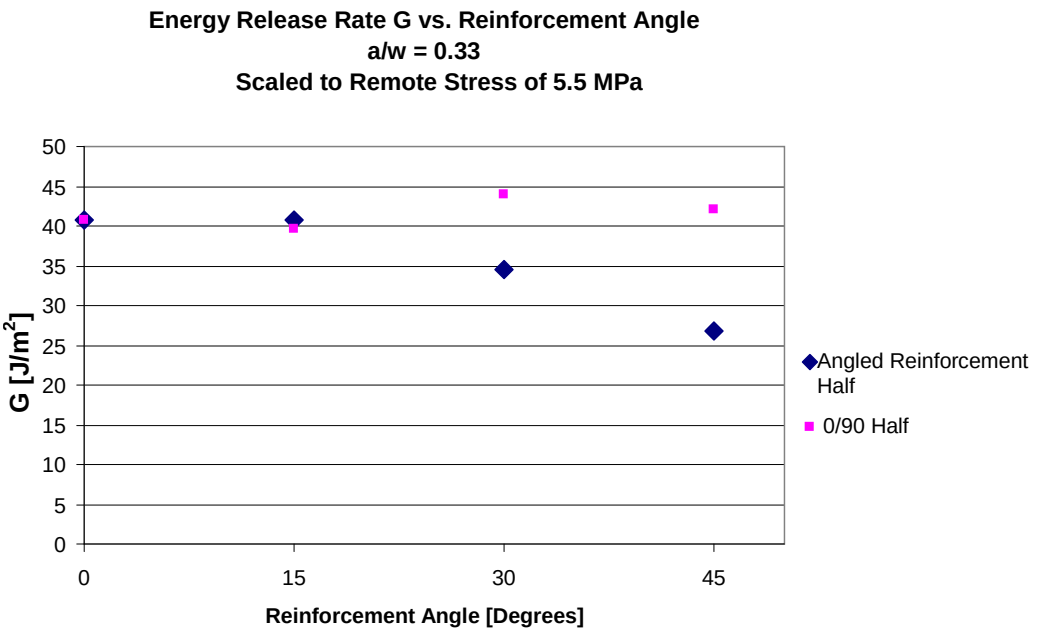

Figure 4.1.10 Energy Release Rate vs. Reinforcement Angle for Bimaterial Specimens with Varying Reinforcement Angle in One Half, a/w = 0.33

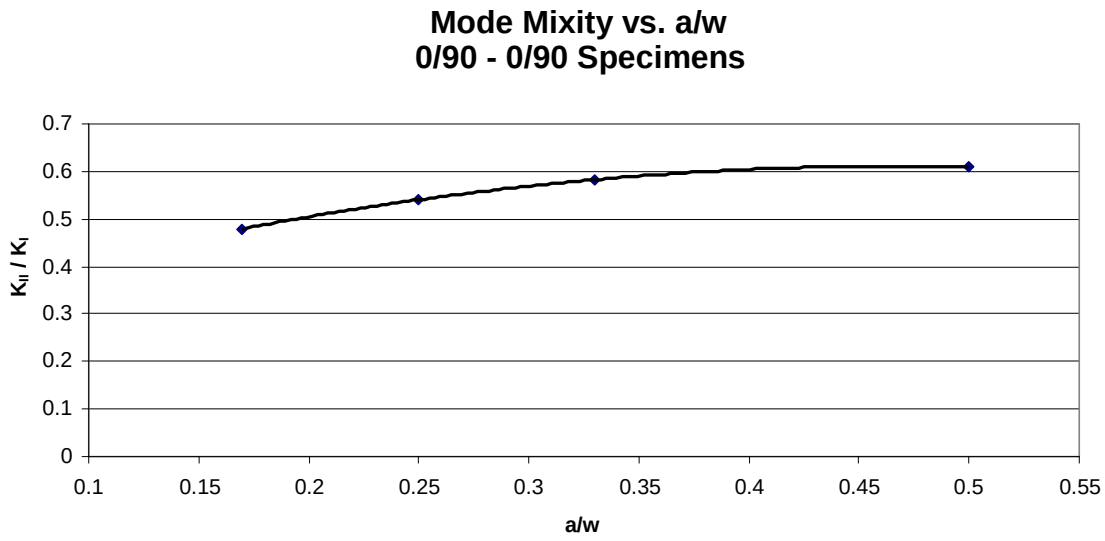

Figure 4.1.11 Mode Mixity vs. a/w Ratio for Specimens with Reinforcement Directions 0°/90° in Both Halves.

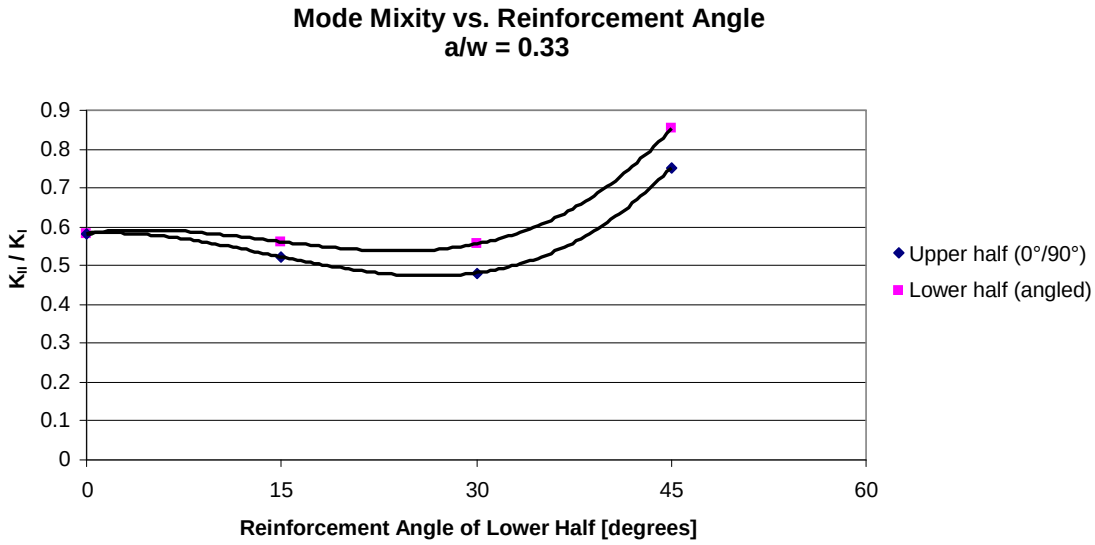

Figure 4.1.12 Mode mixity vs. Reinforcement Angle in Bimaterial Specimens with an Angled Half

In these specimens there was good agreement between the regenerated fringes and the experimentally obtained fringe patterns. In addition, there was good internal consistency in the specimens. What this means is that in specimens with reinforcement directions of 0º/90º in both halves the numerical results were very similar for each bimaterial quadrant. Furthermore, in specimens with reinforcement directions of 0º/90º in one half and some fiber reinforcement direction in the opposing half, there was good consistency within each bimaterial half.

For graphing purposes, the energy release rates G, and the stress intensity factors K_I and K_{II} were scaled to a remote stress of 5.5 MPa (800 Psi). That is, the energy release rates and stress intensity factors for specimens subjected to a remote stress other than 5.5 MPa were multiplied with a scaling factor. The scaling factor was based on the assumption of a linear relationship between remote stress and energy release rate. This assumption is based on the investigation of Khanna, Ellingsen, and Winter [116] which found a linear relationship between remote stress and the opening mode stress intensity factors in composite materials.

Figure 4.1.9 shows the relationship between crack length and energy release rate. A linear trend line has been added; it is difficult to say whether this trend is truly linear or perhaps weakly nonlinear (in a root-square fashion.) While the exact nature of the trend is difficult to determine, it is clear that the energy release rate increased with increasing relative crack length. One implication is clear; larger interfacial cracks pose greater risk for material failures than smaller cracks, not just because there is less cross-sectional area to carry loads, but also because the stress intensity factor near the crack tips is higher.

Figure 4.1.10 shows the relationship between energy release rate and reinforcement directions. In bimaterial halves where the reinforcement directions change, there is a corresponding change in the energy release rate, while the opposing bimaterial half (with unchanged reinforcement directions) see no significant changes in the energy release rate.

Figure 4.1.11 shows that the mode mixity (K_{II} / K_I) increases some with increasing crack length, while Figure 4.1.12 demonstrates that the mode mixity in both bimaterial halves changed when the reinforcement angle was changed in one bimaterial half. It is interesting to note that there was significant mode mixity present in the specimens that are expected to be strongly Mode I dominated.

There are other interesting implications of the results presented in Figure 4.1.11 and Figure 4.1.12: Mode I cracking is the most dangerous or critical mode of cracking, and generally a mixed-mode crack tries to become a Mode I crack to maximize the energy release rates. However, the implication of Figure 4.1.11 is that a larger crack tends toward higher mode mixity, which is to say, the Mode I component is diminished some while Mode II is increased some. This could help counteract the stress-concentration increase that results from increasing the crack length, that is, help reduce the growth rate of an interfacial crack.

Finally, from Figure 4.1.12 it can be seen that the directions of the reinforcement fibers affect mode mixity as well. It should be noted that the expression for calculating energy release rates depended implicitly on fiber angle; therefore the energy release rates were lower in specimen halves with off-axis reinforcement angles. However, when the reinforcement angle was changed in one bimaterial half it changed the mode mixity in *both* halves (that is, also the bimaterial half with reinforcement directions of $0^o/90^o$). This

implies that crack growth resistance can be designed into structures by varying the reinforcement between panels or layers.

The negative sign found in Quadrants 2 and 4 of each specimen was considered a numerical artifact.

4.1.1 Fracture Surface Topographic Examination of Horizontal Interface Bimaterial Specimens

The fracture surfaces of some specimens were examined with a metallurgical optical microscope. Two types of surfaces were very common. In bimaterial halves with reinforcement directions of 0º/90º, such as in Figure 4.1.13, the fracture surfaces were relatively smooth. There were areas of increased surface roughness, but overall the surface was quite smooth.

In contrast, specimens with angled reinforcement tended to have very rough fracture surfaces. This is quite evident in Figure 4.1.14 which shows the fracture surface of a bimaterial specimen half with fiber directions of 30º/60º. The surface was very rough; in fact the roughness exceeded the microscope's focal depth. This roughness appeared to be caused by significant spallation; it appears that the crack tried to grow into this bimaterial half; in other words, the crack tried to deflect its growth away from the horizontal.

These images added support to the conclusion that changing fiber angles can change the mode mixity, and help reduce the effects of increased crack lengths as cracks grow.

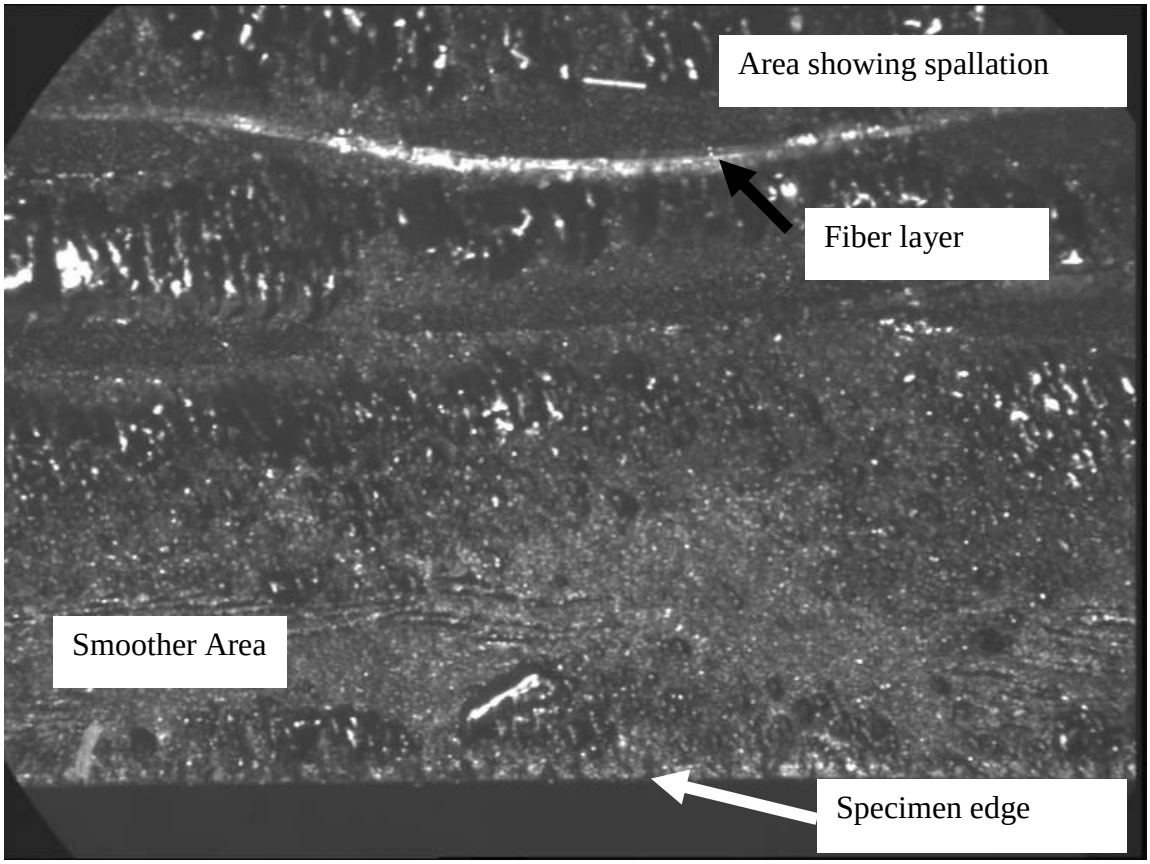

Figure 4.1.13 Fracture Surface (Viewing Fracture Surface Head-On) of 0º/90º Bimaterial Half at 50x Magnification

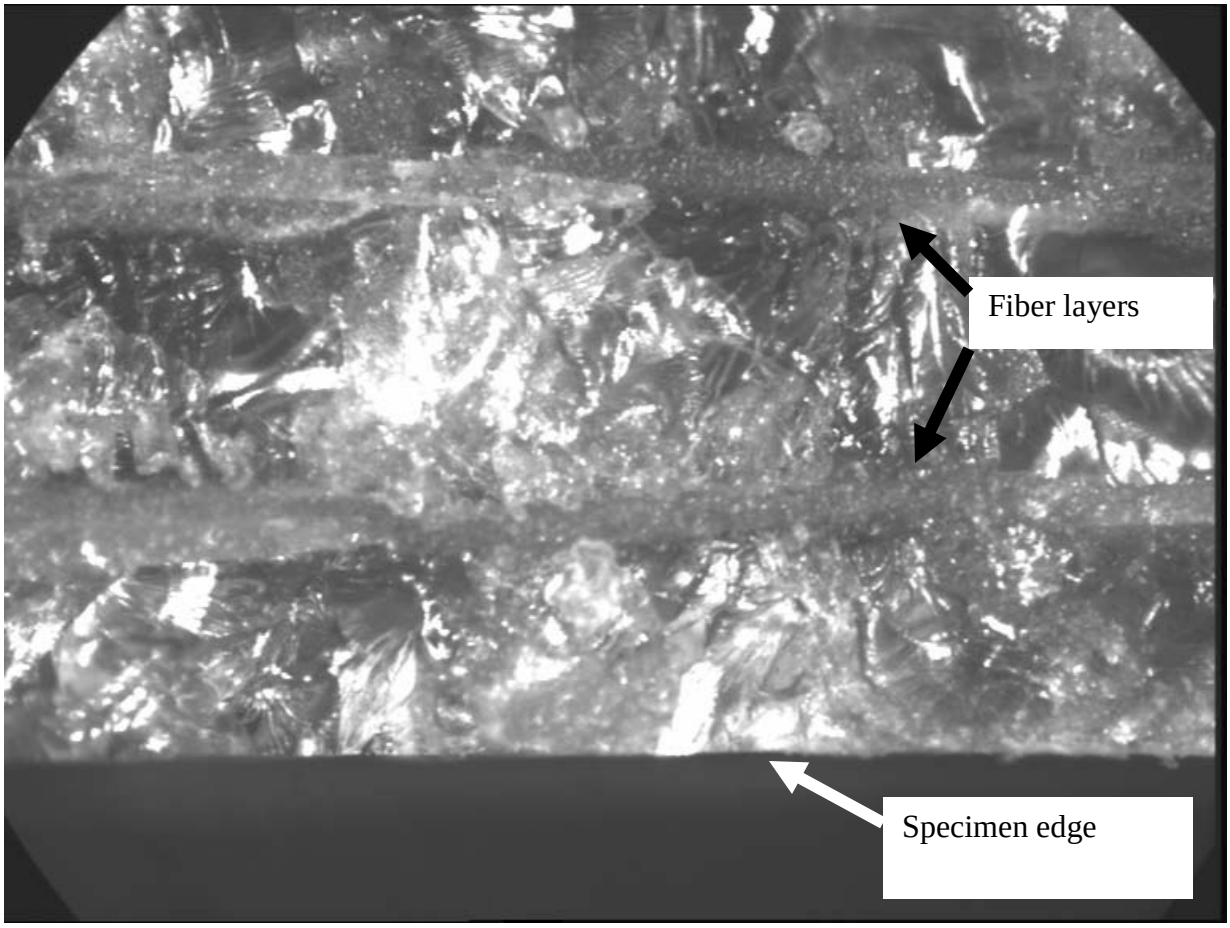

Figure 4.1.14 Fracture Surface (Viewing Fracture Surface Head-On) of 30º/60º Bimaterial Half at 50x Magnification

4.2 Mixed-Mode Fracture (Angled Interface)

Here the K_I and K_{II} values were calculated based on the same methodology described above, using a two-term odd power series, that is n=1. While there were occasional successes with using a larger annular region, such as in Figure 4.2.5, it was again found that regenerating patterns for a large annular region was difficult. For that reason, as in the horizontal interface specimens, data was collected only from a region with an outer diameter of 2t and inner diameter of 0.5t, which is also what was regenerated. The exception is Figure 4.2.5 which was analyzed and regenerated using an annular region with an inner diameter of 1t and an outer diameter of 3t, while all subsequent figures were analyzed and regenerated with the smaller annular region.

In the figures to follow, the interface and reinforcement angle specifications are relative to the horizon. In Lee's equations the term α refers to the angle between the reinforcement and the interface; care must be used to ensure that α is specified as the correct angle when using the Maple worksheets for analysis.

Fringe identification was more difficult in this specimen configuration and it was found to be helpful to the reader to include the full view of each specimen that was presented in this section. Figure 4.2.1 shows a typical fringe pattern progression from zero load to 4.5 kN (1000 lb) load, such progressions were used to help identify the fringe orders properly. Figure 4.2.2 shows the fringe numbering and data points taken from that specimen. In addition, each specimen has been discussed as it has been presented, to clarify issues regarding results and fringe regeneration.

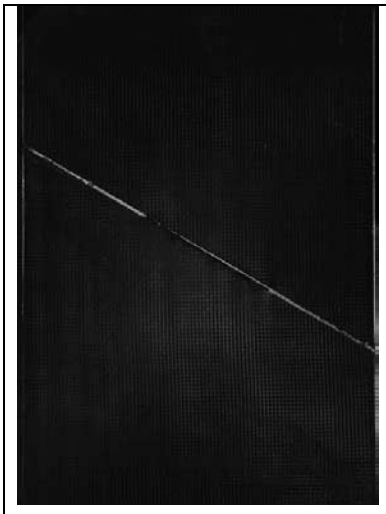		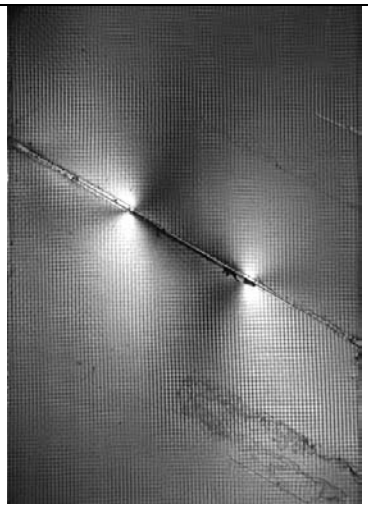
Zero load	0.45 kN (100 lb)	0.9 kN (200 lb)
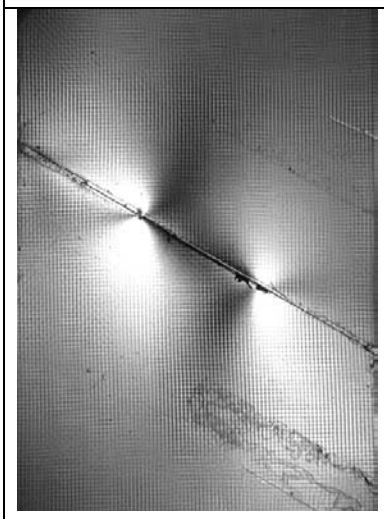	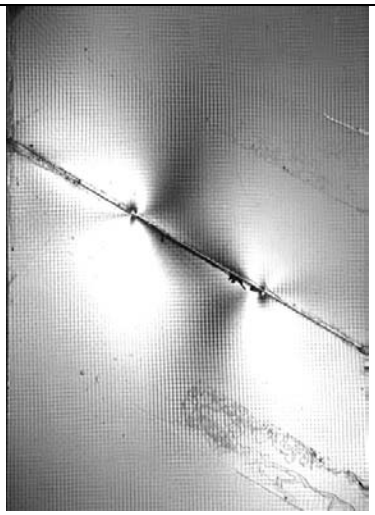	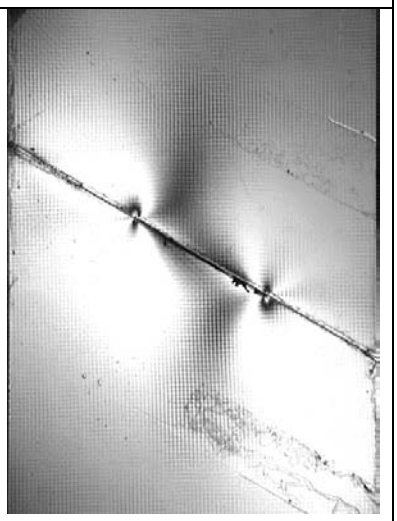
1.3 kN (300 lb)	1.8 kN (400 lb)	2.2 kN (500 lb)

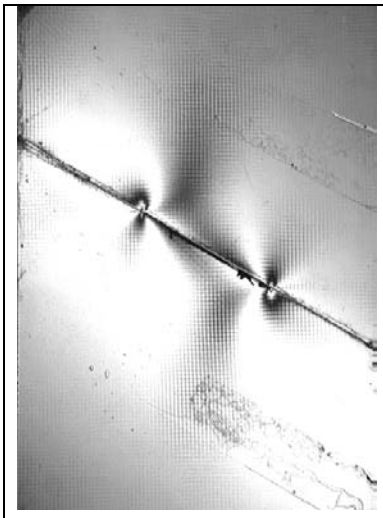

2.7 kN (600 lb)

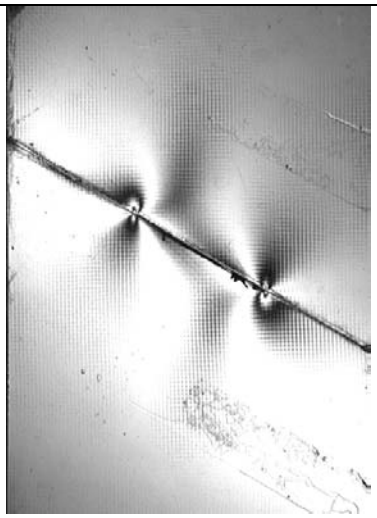

3.1 kN (700 lb)

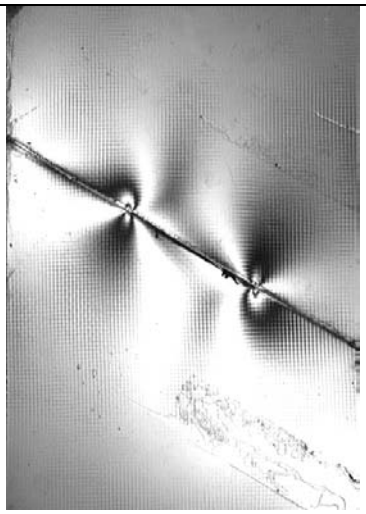

3.6 kN (800 lb)

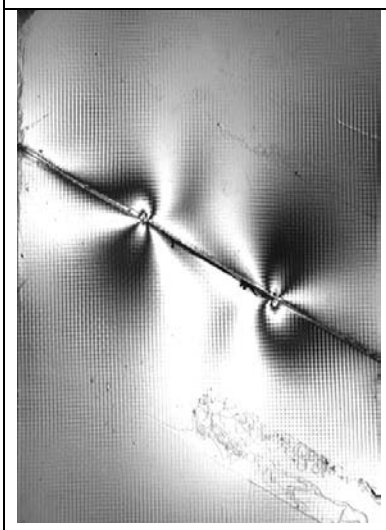

4.0 kN (900 lb)

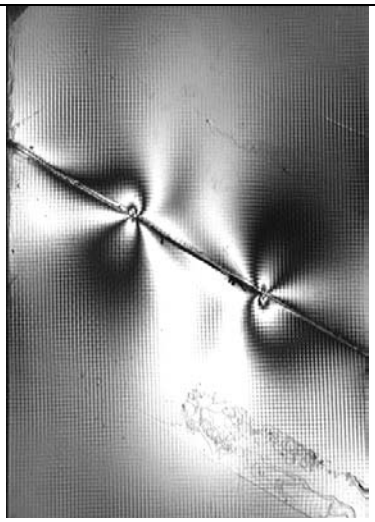

4.5 kN (1000 lb)

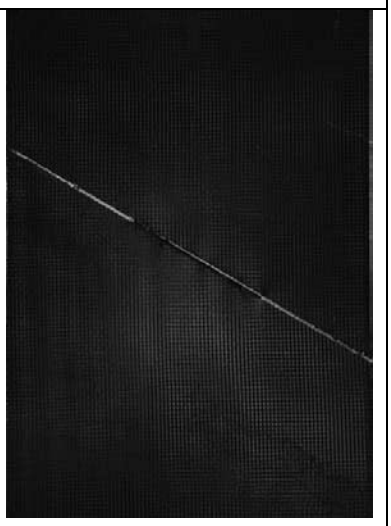

Load removed

Figure 4.2.1 Fringe Pattern Progression in Specimen with Interface Angle 30°, 0°/90° Composite - 0°/90° Composite Bimaterial, a/w = 0.33, w = 127 mm (5 in.)

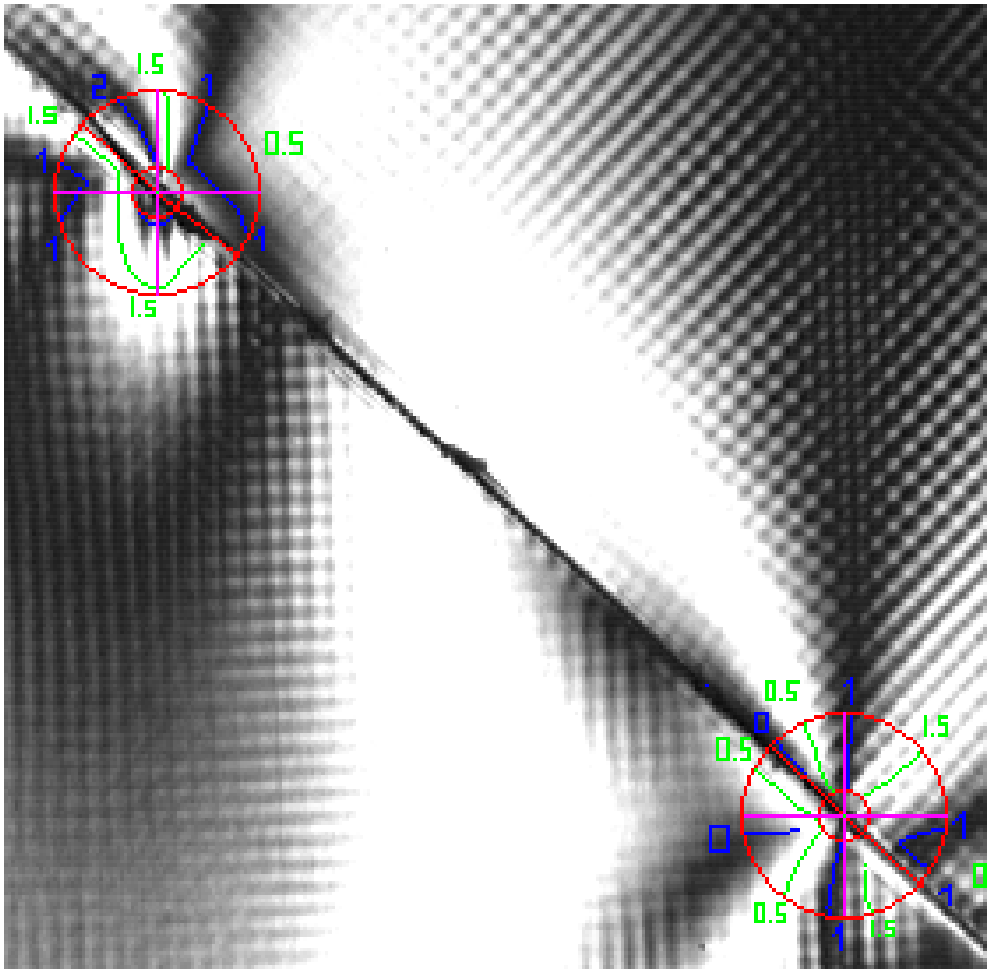

Figure 4.2.2 Annular Regions, Fringe Orders, and Data Points Taken from Specimen with Interface Angle 45°, 0°/90° Composite - ±45° Composite Bimaterial, a/w = 0.33, w = 127 mm (5 in.)under 4.0 kN (900 lb) load.

4.2.1 Fringe Asymmetries

An interesting phenomenon can be observed in the fringe progression shown above, which is that fringes develop asymmetrically across the interface. They show that the stresses are not equally distributed around the crack tips.

When the interface is angled the tractions acting upon it are not only trying to pull it apart. There is also a tendency to try to slide the interface apart, that is, there are significant shear forces acting along the interface. Consider the left crack tip in the bimaterial illustrated in Figure 4.2.3; it illustrates (for clarity) that there are fringe asymmetries across the interface. This shows that for angled interfaces the stress state is not symmetrical across the interface, Quadrant 2 and Quadrant 3 do not show the same number of fringes emanating from the crack tip. The same was observed in Quadrant 1 and Quadrant 4. However, the fringe count in Quadrant 1 and Quadrant 3 was the same, as was the fringe count in Quadrant 2 and Quadrant 4. This was referred to as “diagonal symmetry”; the fringe count in the vertically or horizontally opposed quadrants were different, but the fringe count in diagonally opposed quadrants was the same. The results are reported separately for the two instances of fringe count.

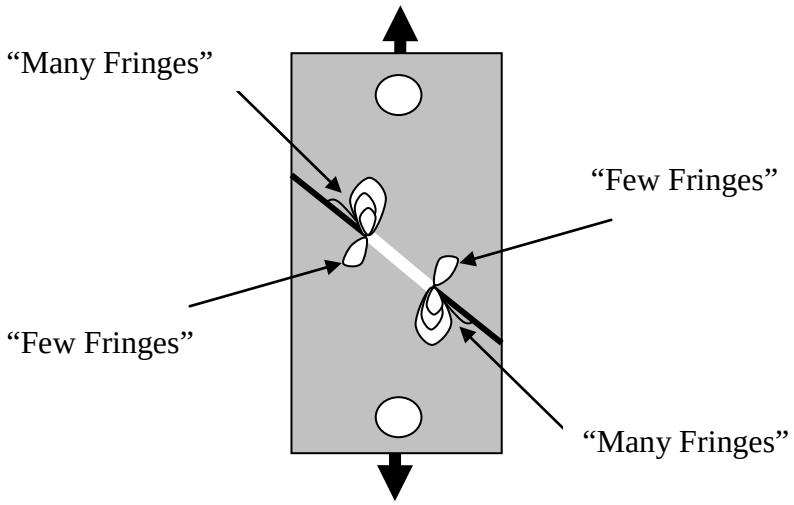

Figure 4.2.3 Asymmetric Development of Fringes Across Interface

4.2.2 Angled Interface Specimen Tests and Results

Several angled interface composite-composite and composite-aluminum bimaterial specimens under load in the circular polariscope are shown below. The resultant isochromatic fringe patterns have been analyzed, and stress intensity factors and energy release rates have been calculated. For verification, the observed isochromatic fringe patterns were mathematically regenerated. There were instances where the isochromatic fringe pattern for a specimen quadrant could not be well regenerated; in such cases no numerical results were reported, and it was stated that for the relevant specimen quadrant a good regeneration was not achieved.

4.2.2.1 Constant Reinforcement Directions (0º/90º - 0º/90º Composite-Composite Bimaterials), Varying Interface Angle

In this segment the reinforcement directions were kept constant at 0º/90º in both bimaterial halves, while the interface angle was varied.

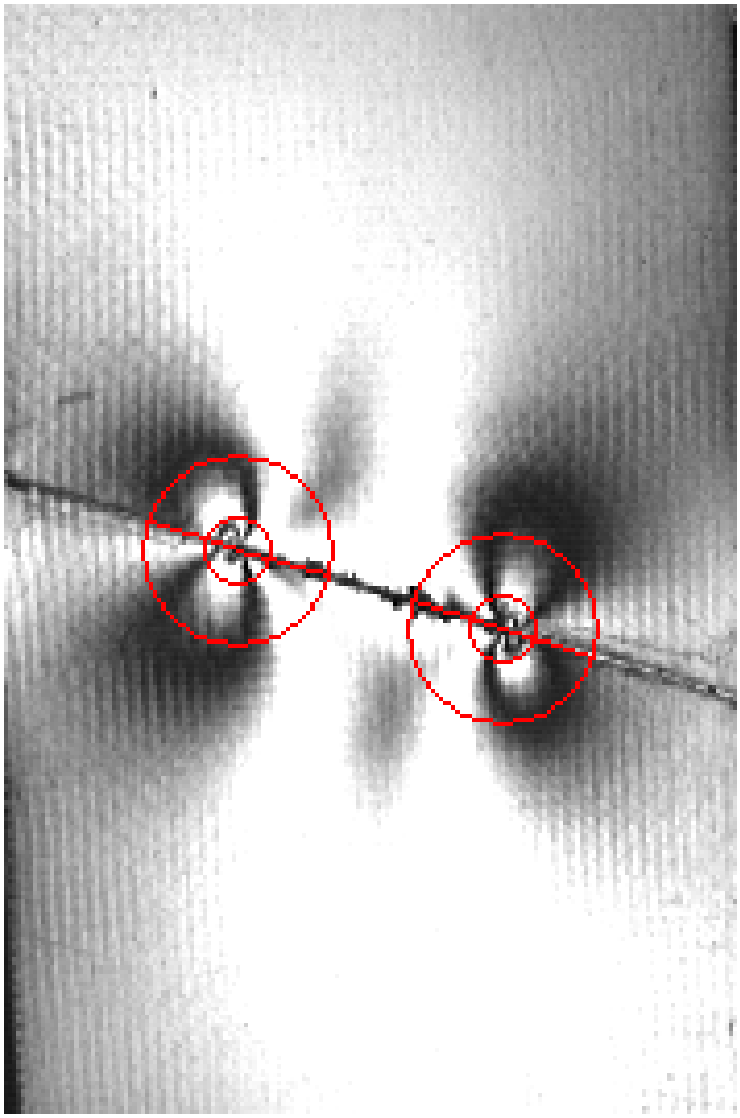

Figure 4.2.4 Interface Angle 15°, 0°/90° Composite - 0°/90° Composite Bimaterial, 2.7 kN (600 lb) Load, a/w = 0.33, w = 76 mm (3.0 in), Annular Region ID = 1t, OD = 3t (The only specimen to have OD = 3t)

2nd Quadrant (0°/90°)

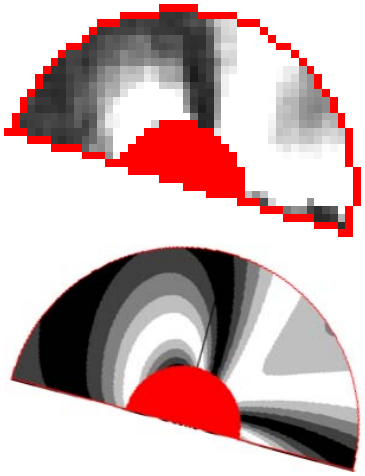

$K_I = 1.18 MPa\sqrt{m}$

$K_{II} = -0.54 MPa\sqrt{m}$

$\frac{K_{II}}{K_I} = 0.46$

$G = 47.4 N/m^2$

1st Quadrant (0°/90°)

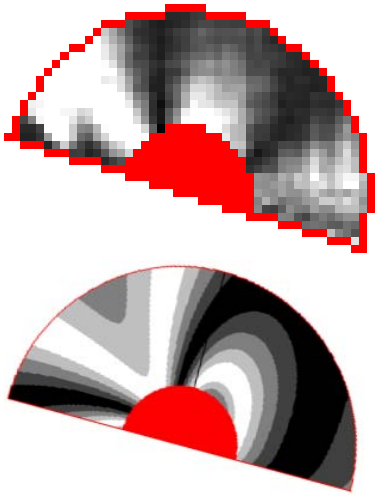

$K_I = 1.15 MPa\sqrt{m}$

$K_{II} = 0.49 MPa\sqrt{m}$

$\frac{K_{II}}{K_I} = 0.43$

$G = 44.3 N/m^2$

4th Quadrant (0°/90°)

$K_I = 1.18 MPa\sqrt{m}$

$K_{II} = 0.48 MPa\sqrt{m}$

$\frac{K_{II}}{K_I} = 0.41$

$G = 45.4 N/m^2$

3rd Quadrant (0°/90°)

$K_I = 1.30 MPa\sqrt{m}$

$K_{II} = -0.48 MPa\sqrt{m}$

$\frac{K_{II}}{K_I} = 0.37$

$G = 54.0 N/m^2$

Figure 4.2.5 Annular Regions and Regenerated Fringe Patterns for Specimen Shown in Figure 4.2.4

Brief discussion of results for the specimen shown in Figure 4.2.4:

Experimental fringe patterns were symmetrical across the interface, which is reasonable considering that the interface angle was small, 15º. The regenerated fringes corresponded well with their experimentally obtained counterparts. The numerical results for Q1, Q2, and Q3 were internally very consistent, while the results for Q4 were somewhat higher. Mode mixity was similar in all quadrants. Overall this was a good result.

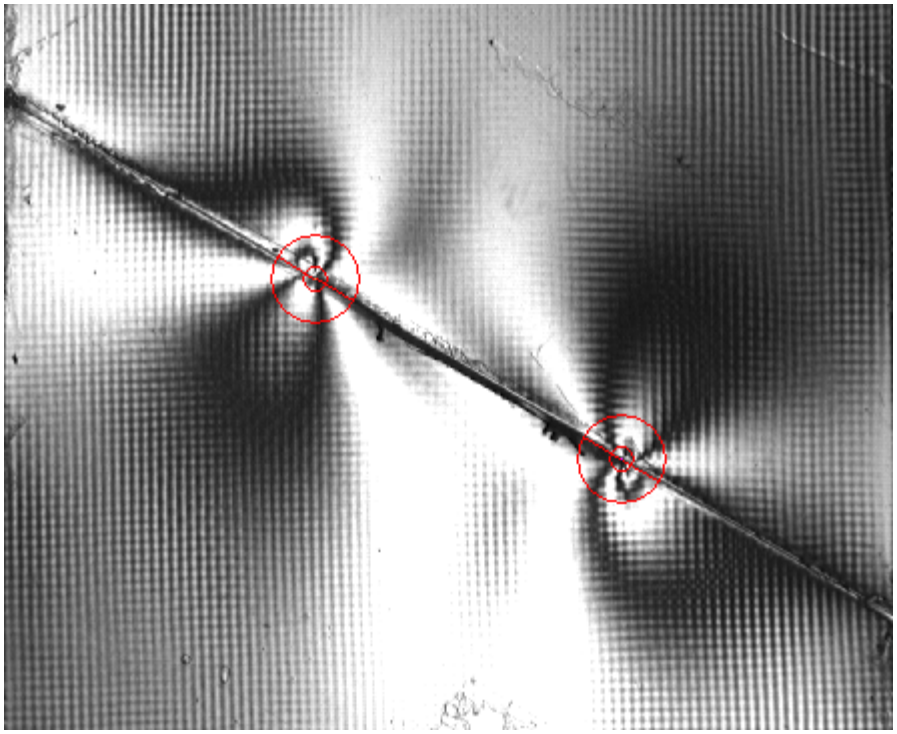

Figure 4.2.6 Interface Angle 30º, 0°/90° Composite - 0°/90° Composite Bimaterial, 4kN (900 lb) load, a/w = 0.33, w = 127 mm (5 in.)

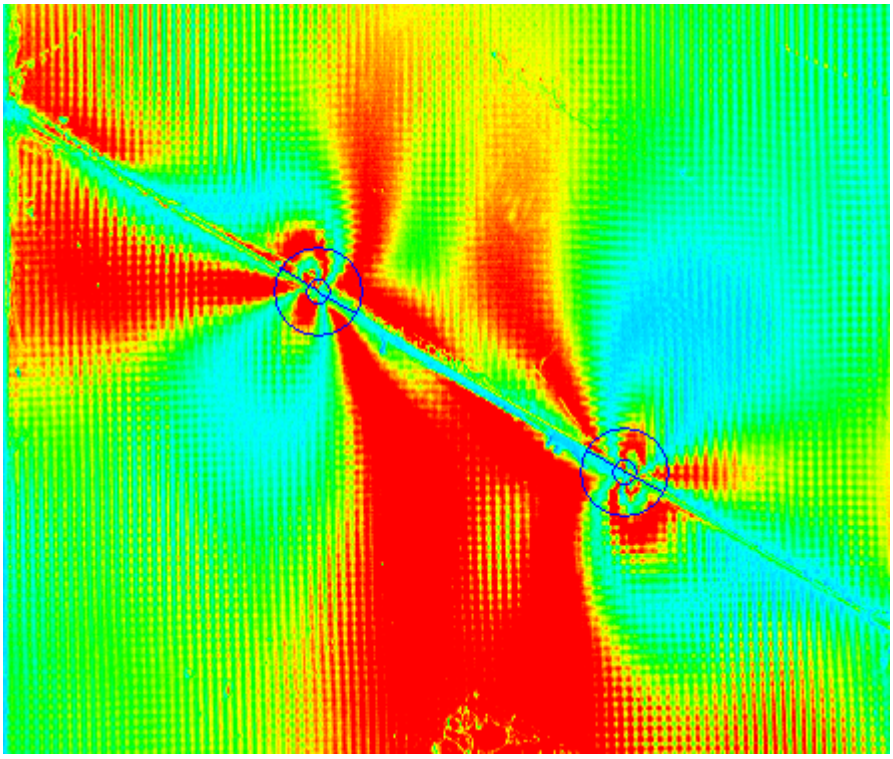

Figure 4.2.7 False-Color Fringe Multiplied Image of Specimen Shown in Figure 4.2.6

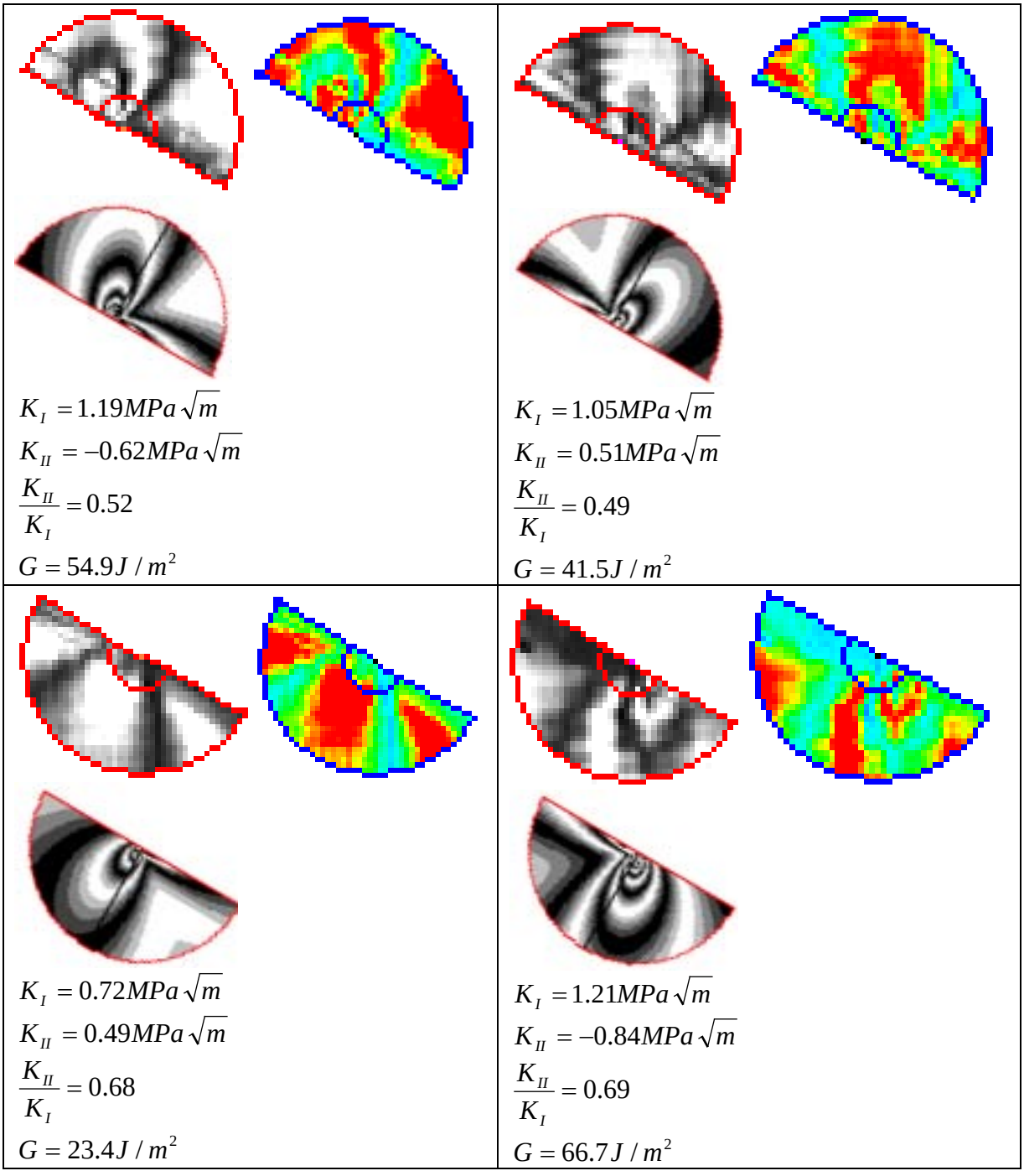

Figure 4.2.8 Annular Regions and Regenerated Fringe Patterns for Specimen Shown in Figure 4.2.6

Brief Discussion of the Results for the Specimen Shown in Figure 4.2.6:

The experimentally obtained patterns were not symmetrical across the interface. The fringe count was “high” in Q2 and Q4, and “low” in Q1 and Q3. The number of fringes observed in Q2 and Q4 were the same. The number of fringes should have been the same between Q1 and Q3; they were though the 2^{nd} order fringe in Q3 was smaller than that in Q1. The diagonal symmetry was thus present between Q1 and Q3, and to a lesser degree between Q2 and Q4.

The fringe patterns were well regenerated for Q2 and Q4, and their numerical results agreed reasonably well. The mathematically regenerated patterns for Q1 and Q3 were fair matches. Mode mixity (K_{II} / K_I) were similar for all quadrants, between 0.5 and 0.7.

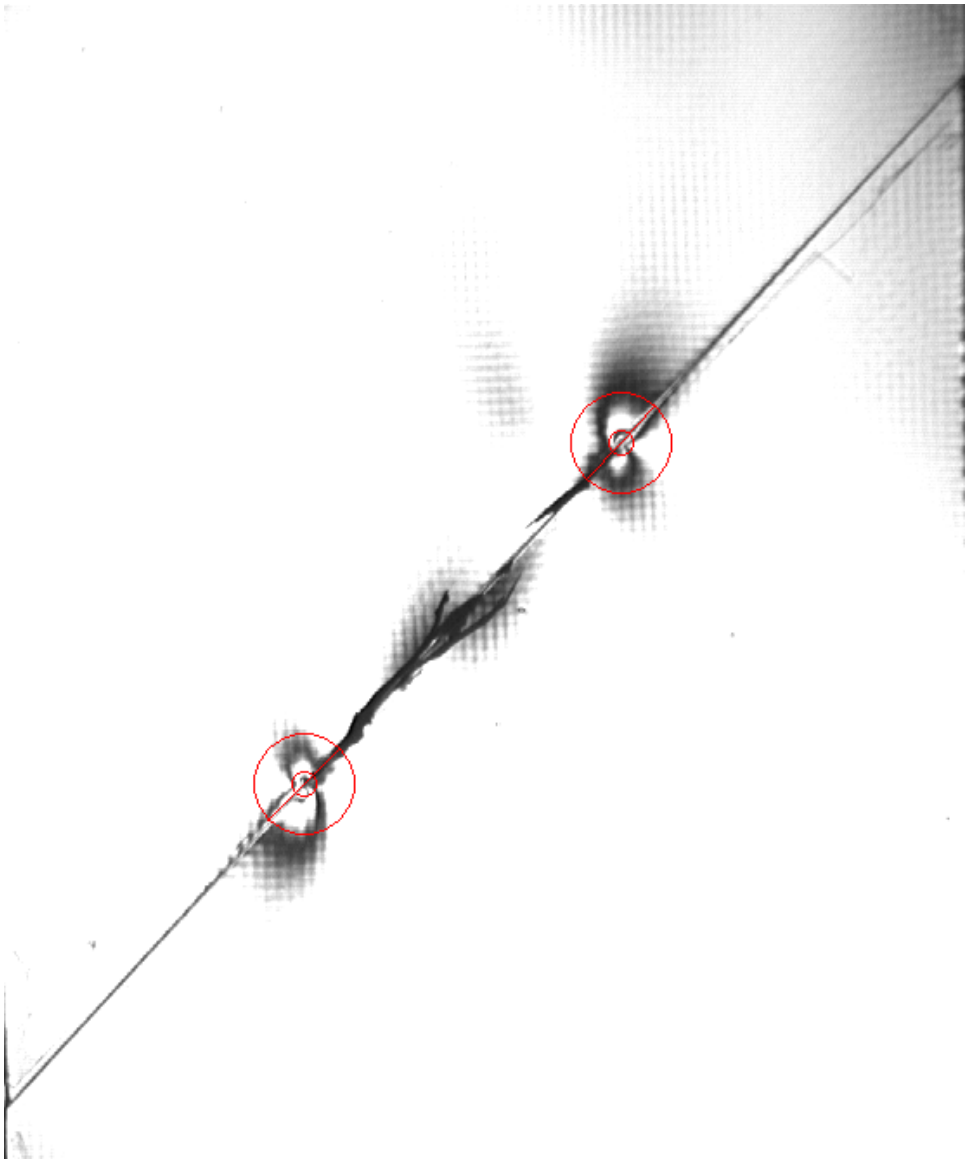

Figure 4.2.9 Interface Angle 45°, 0°/90° Composite - 0°/90° Composite Bimaterial, 2.7kN (600 lb) load, a/w = 0.33, w = 127 mm (5 in.)

2nd Quadrant (0°/90°)

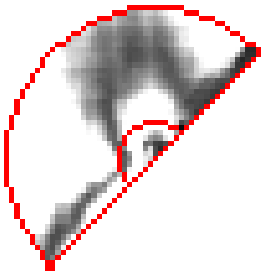

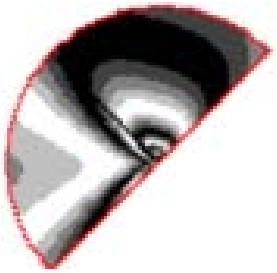

$K_I = 0.79MPa\sqrt{m}$

$K_{II} = 0.43MPa\sqrt{m}$

$\frac{K_{II}}{K_I} = 0.54$

$G = 15.8J/m^2$

1st Quadrant (0°/90°)

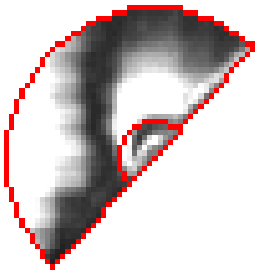

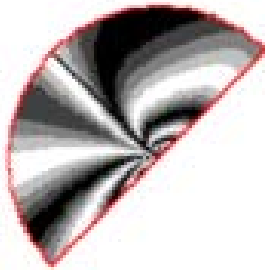

$K_I = 1.48MPa\sqrt{m}$

$K_{II} = 0.27MPa\sqrt{m}$

$\frac{K_{II}}{K_I} = 0.18$

$G = 44.7J/m^2$

3rd Quadrant (0°/90°)

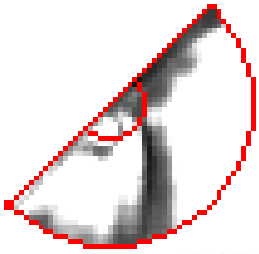

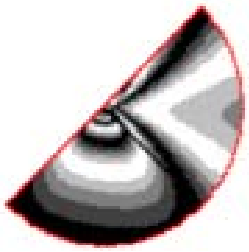

$K_I = 1.06MPa\sqrt{m}$

$K_{II} = 0.46MPa\sqrt{m}$

$\frac{K_{II}}{K_I} = 0.43$

$G = 26.6J/m^2$

4th Quadrant (0°/90°)

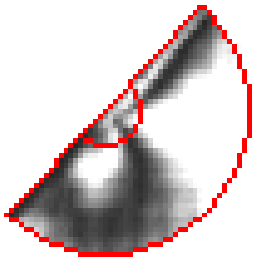

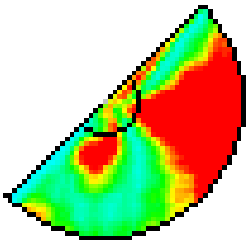

Unable to regenerate good pattern

Figure 4.2.10 Annular Regions and Regenerated Fringe Patterns for Specimen Shown in Figure 4.2.9

Brief Discussion of the Results for the Specimen Shown in Figure 4.2.9:

The experimentally obtained fringe patterns showed the expected asymmetry across the interface. There was a higher fringe count in Q1 and Q3 than in Q2 and Q4. There was diagonal symmetry between Q2 and Q4, but the expected diagonal symmetry between Q1 and Q3 was not present: As shown in Figure 4.2.11 the first order fringe in Q3 extends much farther out than the first order fringe in Q1, indicating that the stress states are not the same.

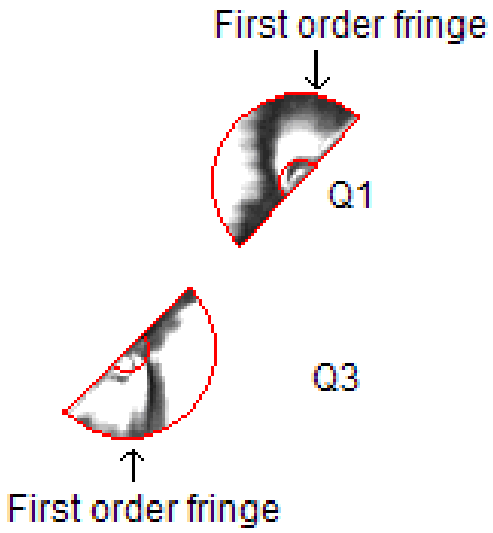

Figure 4.2.11 Discussion of Fringe Patterns in Figure 4.2.9

The mathematically regenerated fringes were a good match for Q1 and Q2. The mathematically regenerated fringes were a fair match for Q3. A satisfactory fringe regeneration was not obtained for Q4. Color fringe multiplication was applied for Q4 but did not help. Mode mixity was low in Q1, but high in Q2 and Q3.

4.2.2.2 Constant Interface Angle (45º), Varying Reinforcement Angle in One Bimaterial Half

In this segment the interface angle was kept constant at 45º. What vas varied were the reinforcement directions in one bimaterial half, while the reinforcement directions in the opposing bimaterial half were kept constant at 0º/90º.

The diagonal symmetry observed in the preceding section was not expected to be found here because the reinforcement directions were different between the diagonally opposed quadrants. That is, Q1 and Q3 had different reinforcement directions from each other, as did Q2 and Q4. However, there will still be asymmetry between quadrants in the same bimaterial half, that is, Q1 and Q2 will show different fringe counts, as will Q3 and Q4.

Therefore, it was expected that within each specimen there would be few common results between quadrants; each quadrant would differ from the others in either fringe count or fiber direction.

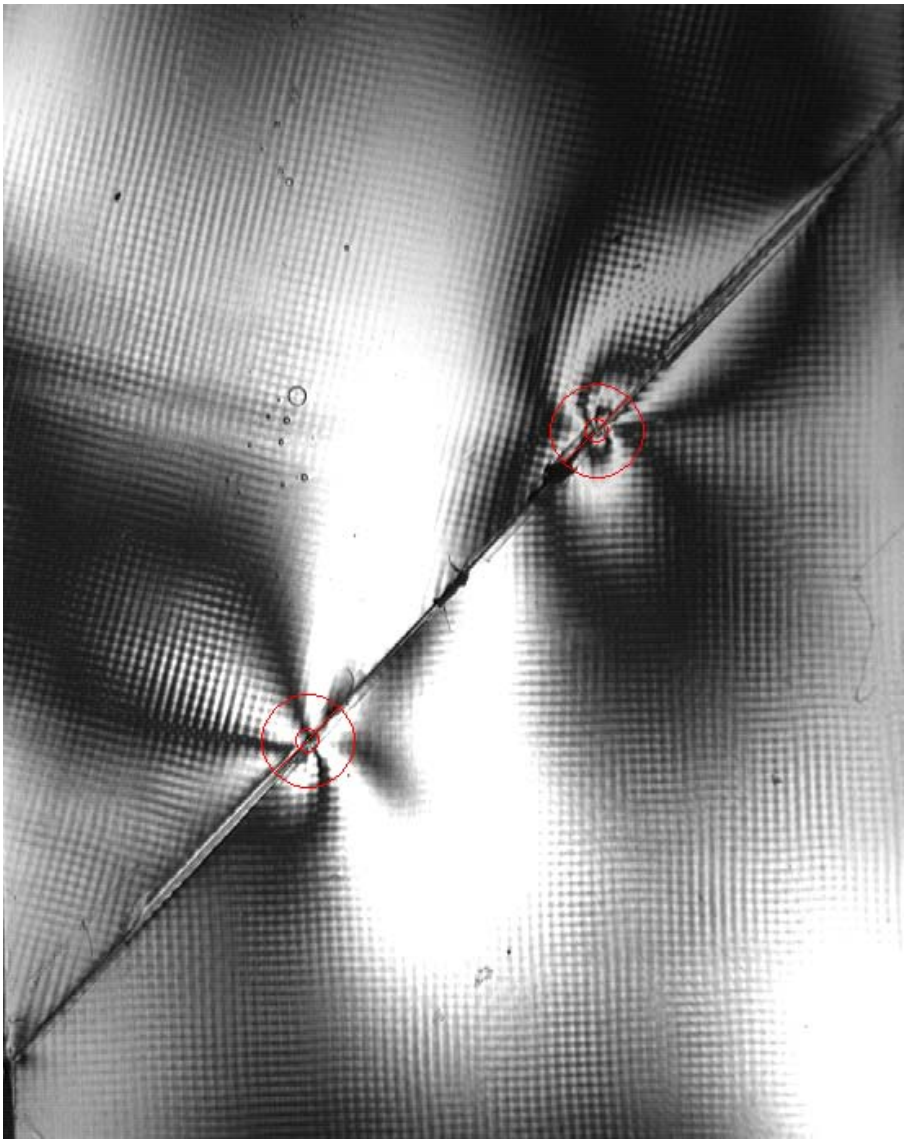

Figure 4.2.12 Interface Angle 45°, 15°/75° Composite - 0°/90° Composite Bimaterial, 4kN (900 lb) load, a/w = 0.33, w = 127 mm (5 in.)

2nd Quadrant (15°/75°)	**1st Quadrant (15°/75°)**
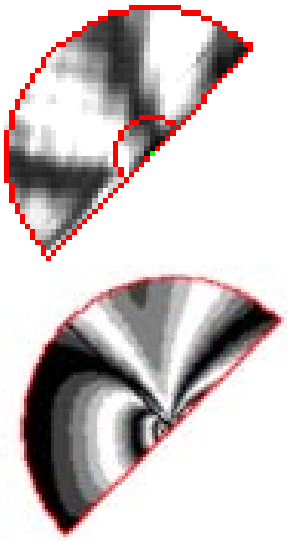	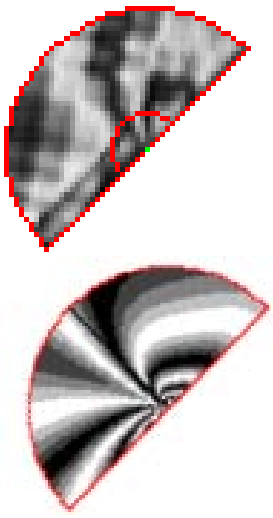
$K_I = 1.25MPa\sqrt{m}$ $K_{II} = -0.36MPa\sqrt{m}$ $\frac{K_{II}}{K_I} = 0.29$ $G = 38.1J/m^2$	$K_I = 1.63MPa\sqrt{m}$ $K_{II} = 0.33MPa\sqrt{m}$ $\frac{K_{II}}{K_I} = 0.20$ $G = 62.6J/m^2$
3rd Quadrant (0°/90°)	**4th Quadrant (0°/90°)**
$K_I = 1.54MPa\sqrt{m}$ $K_{II} = 0.27MPa\sqrt{m}$ $\frac{K_{II}}{K_I} = 0.18$ $G = 48.3J/m^2$	(Numerical results not reported)

Figure 4.2.13 Annular Regions and Regenerated Fringe Patterns for Specimen Shown in Figure 4.2.12

Brief Discussion of the Results for the Specimen Shown in Figure 4.2.12:

Q1 has a higher fringe count than Q2. Q4 has a higher fringe count than Q3. The fringe patterns in Q1 and Q3 were well regenerated. The fringe pattern in Q2 was regenerated to a fair match, while the fringe pattern in Q4 was regenerated poorly. The stress intensity factors for Q1 and Q3 agreed well with each other, which is reasonable considering the difference in reinforcement angles is small.

The energy release rates are mathematically a function of reinforcement angle; therefore they differed between Q1 and Q3. The numerical results for Q4 were not reported, as the regenerated fringe patterns were not a satisfactory match.

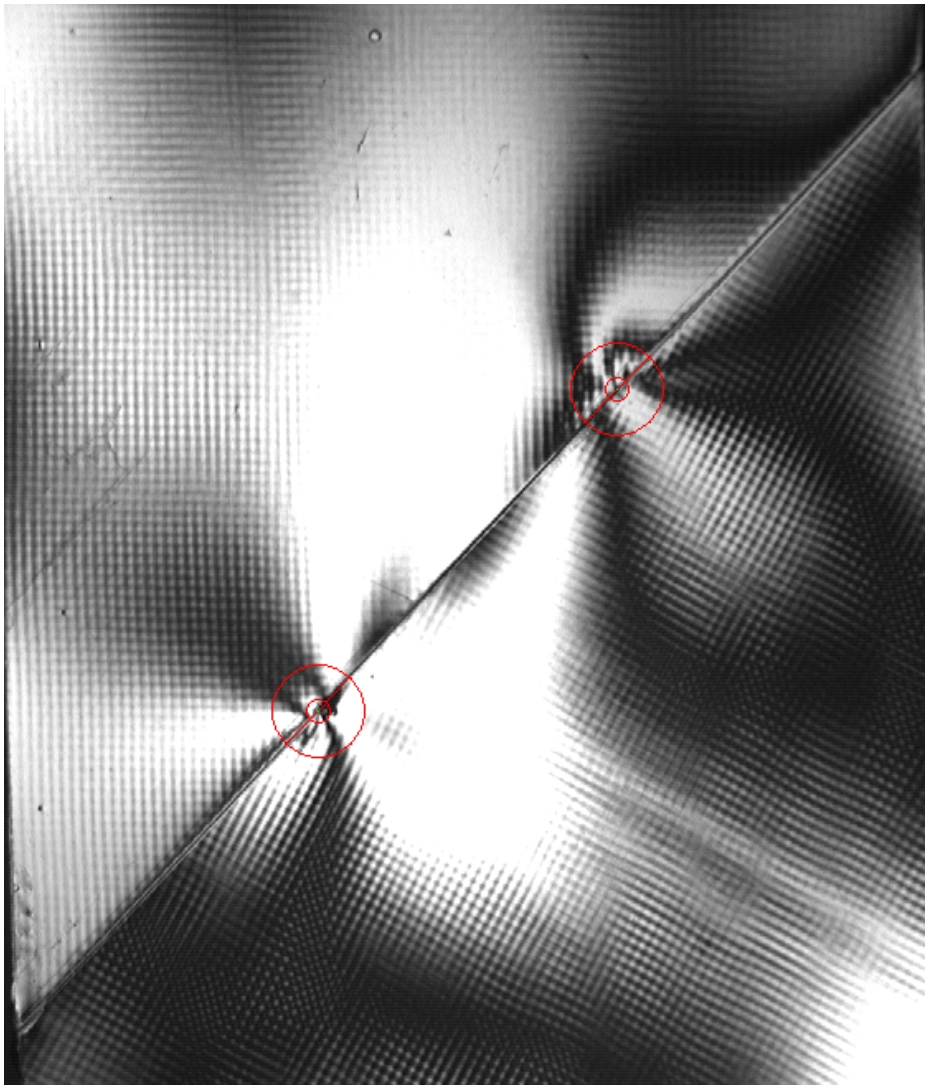

Figure 4.2.14 Interface Angle 45°, 0°/90° Composite - 30°/60° Composite Bimaterial, 4kN (900 lb) load, a/w = 0.33, w = 127 mm (5 in.)

2nd Quadrant (0°/90°)	**1st Quadrant (0°/90°)**
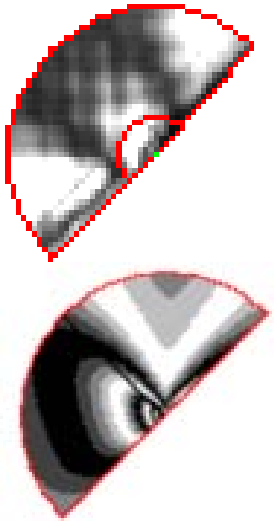	
$K_I = 0.76MPa\sqrt{m}$ $K_{II} = -0.41MPa\sqrt{m}$ $\frac{K_{II}}{K_I} = 0.54$ $G = 14.8J/m^2$	$K_I = 1.60MPa\sqrt{m}$ $K_{II} = 0.15MPa\sqrt{m}$ $\frac{K_{II}}{K_I} = 0.09$ $G = 50.9J/m^2$
3rd Quadrant (30°/60°)	**4th Quadrant (30°/60°)**
$K_I = 1.34MPa\sqrt{m}$ $K_{II} = 0.42MPa\sqrt{m}$ $\frac{K_{II}}{K_I} = 0.31$ $G = 54.6J/m^2$	$K_I = -0.59MPa\sqrt{m}$ $K_{II} = 0.57MPa\sqrt{m}$ $\frac{K_{II}}{K_I} = 0.97$ $G = 18.6J/m^2$

Figure 4.2.15 Annular Regions and Regenerated Fringe Patterns for Specimen Shown in Figure 4.2.14

Brief Discussion of the Results for the Specimen Shown in Figure 4.2.14:

The fringe count in Q1 is higher than in Q2. The fringe count in Q3 is higher than in Q4. The fringe patterns are satisfactorily regenerated in Q1 and Q3, and moderately well regenerated in Q2 and Q4.

The mode mixity in Q2 is higher than in Q1. Similarly, the mode mixity in Q4 is higher than in Q3. This follows the trend that high fringe count regions display lower mode mixity, and low fringe count regions display higher mode mixity.

The stress intensity factors and energy release rates were not expected to be similar between any quadrants, because each quadrant differed from each other in either fiber direction or fringe count.

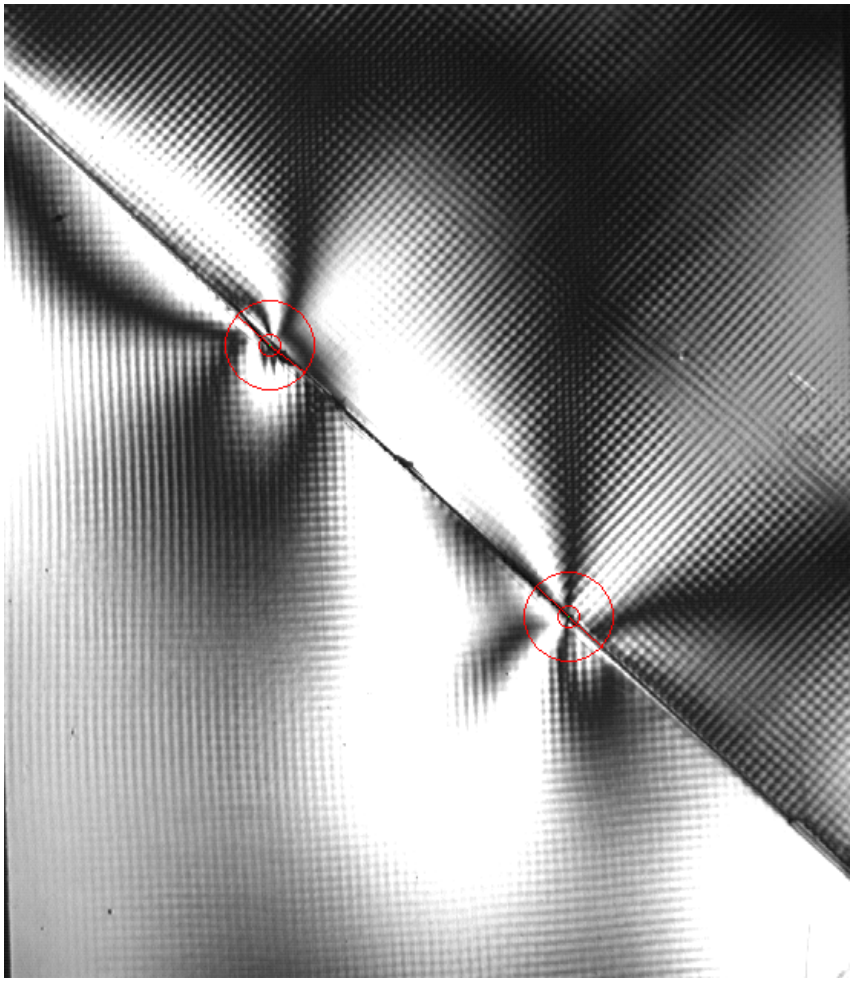

Figure 4.2.16 Interface Angle 45°, ±45° Composite - 0°/90° Composite Bimaterial, 4kN (900 lb) load, a/w = 0.33, w = 127 mm (5 in.)

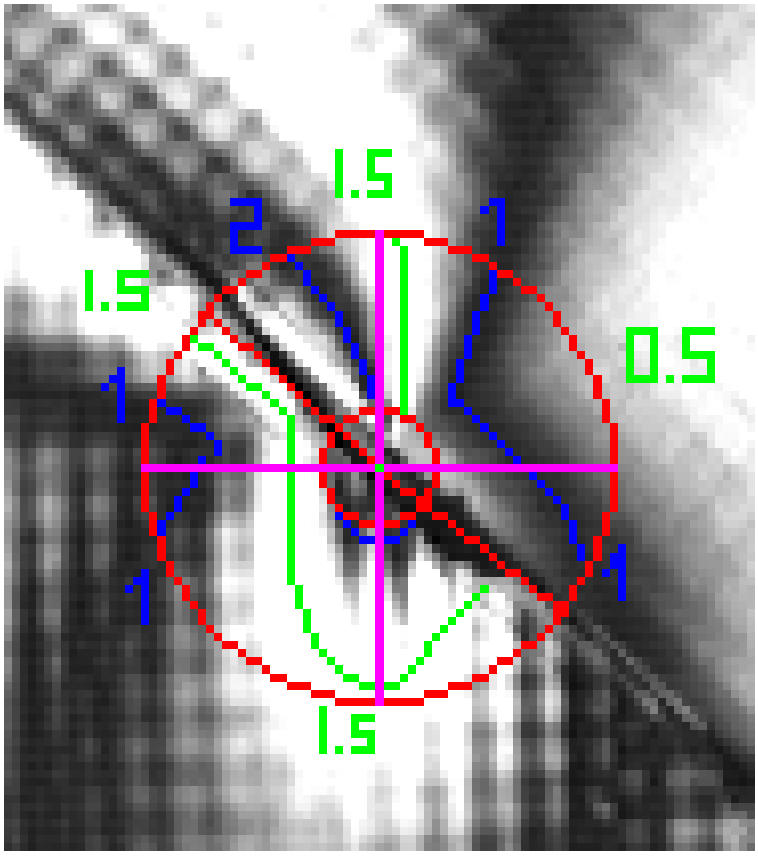

Figure 4.2.17 Identification of Fringe Orders, Data Points Taken, from Quadrant 2 and 3 from Specimen in Figure 4.2.16

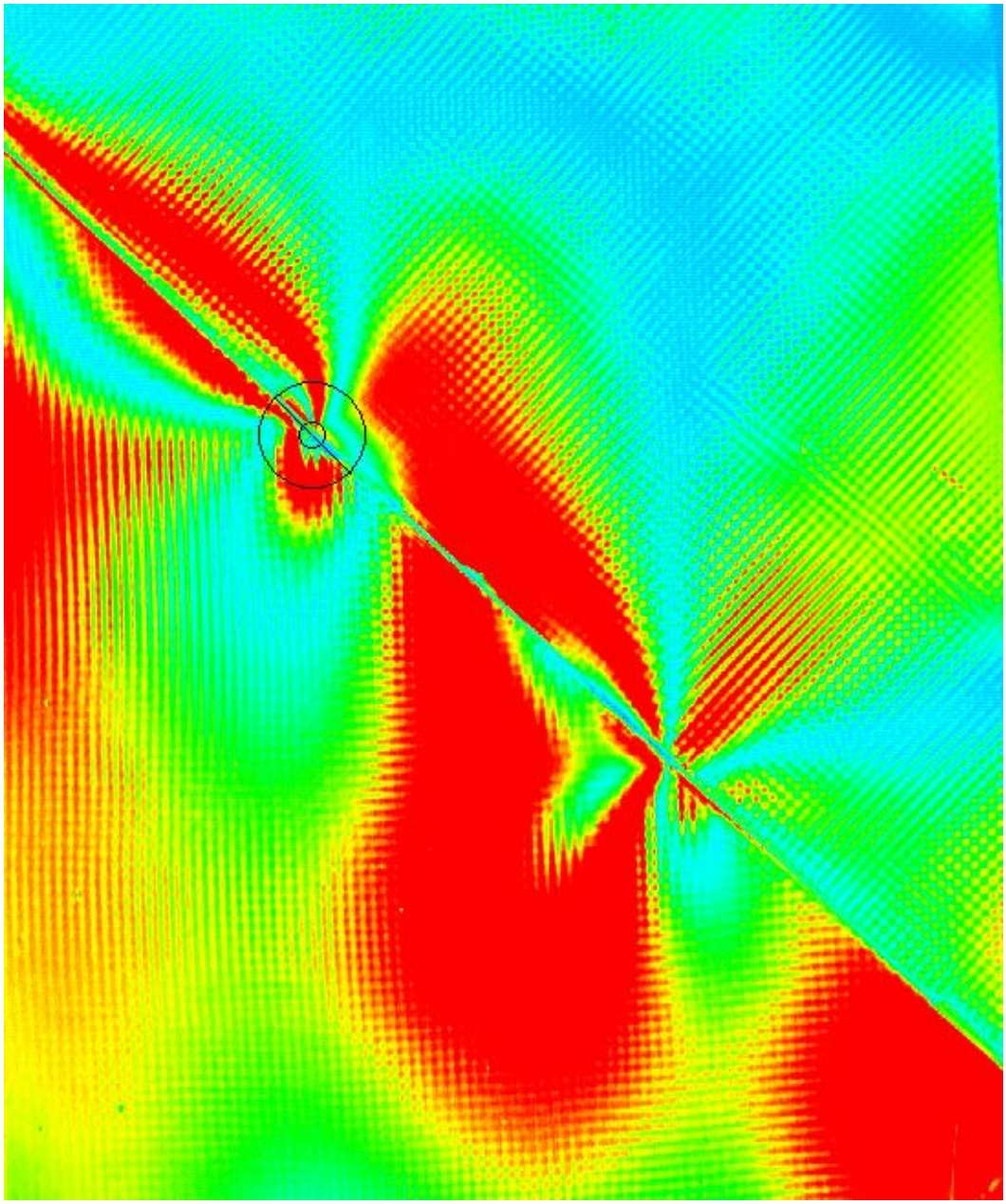

Figure 4.2.18 False-Color Fringe Multiplied Version of Figure 4.2.16

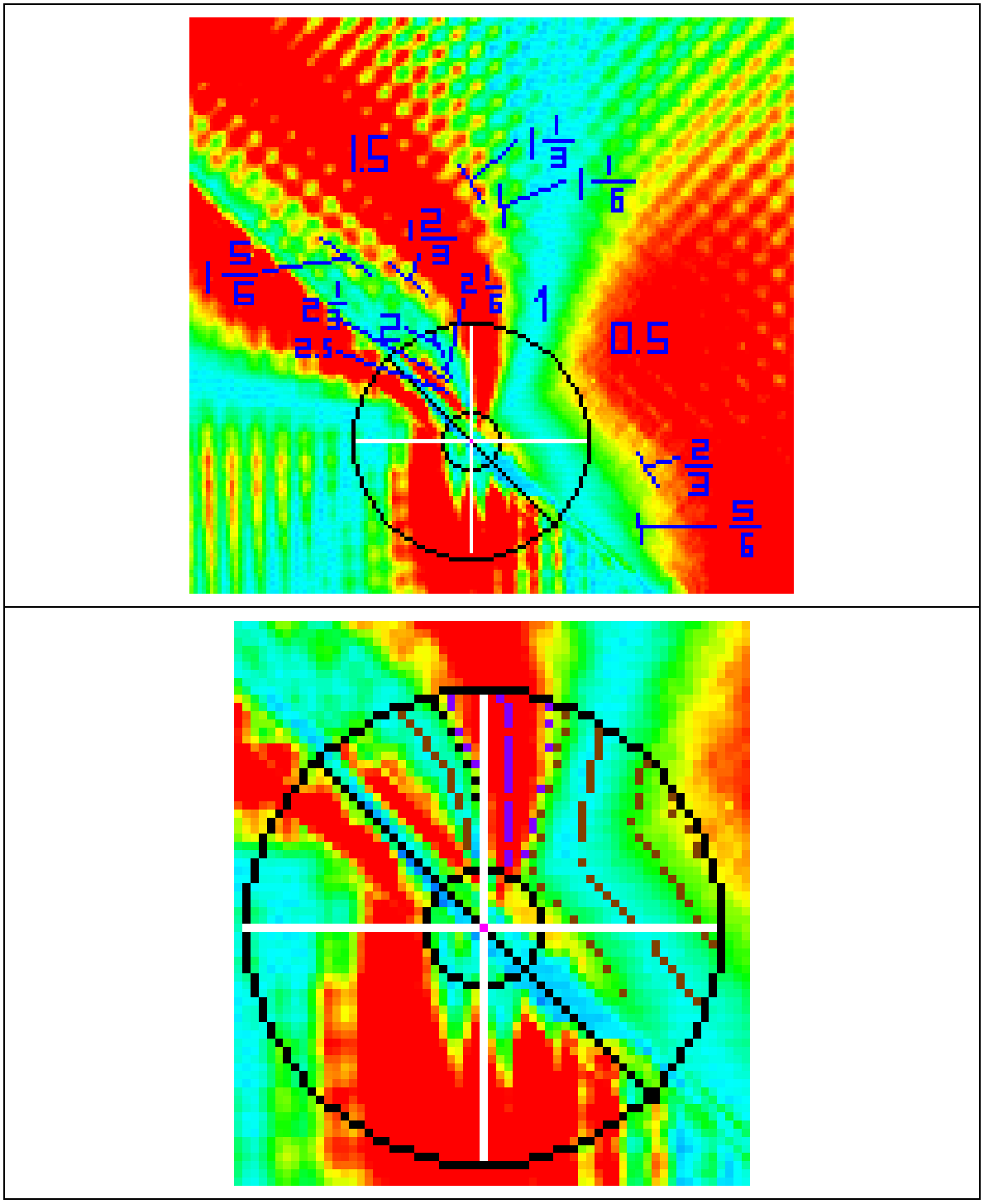

Figure 4.2.19 Identification of Fractional Fringe Orders, and Data Points, in Quadrant 2 of the False-Color Fringe Multiplied Specimen in Figure 4.2.16

<table>
<tr>
<td colspan="2">2nd Quadrant (±45°)</td>
<td>1st Quadrant (±45°)</td>
</tr>
<tr>
<td>

$K_I = 1.47 MPa\sqrt{m}$
$K_{II} = 0.12 MPa\sqrt{m}$
$\frac{K_{II}}{K_I} = 0.08$
$G = 66.3 J/m^2$</td>
<td> 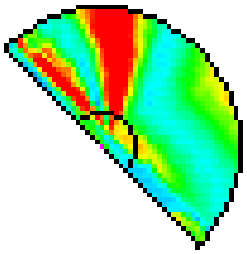

$K_I = 1.37 MPa\sqrt{m}$
$K_{II} = 0.12 MPa\sqrt{m}$
$\frac{K_{II}}{K_I} = 0.09$
$G = 59.2 J/m^2$</td>
<td>
 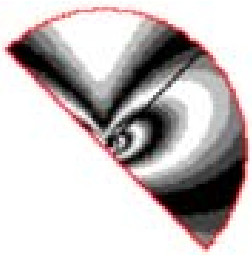
$K_I = 0.92 MPa\sqrt{m}$
$K_{II} = 0.57 MPa\sqrt{m}$
$\frac{K_{II}}{K_I} = 0.35$
$G = 36.2 J/m^2$</td>
</tr>
<tr>
<td colspan="2">3rd Quadrant (0°/90°)</td>
<td>4th Quadrant (0°/90°)</td>
</tr>
<tr>
<td>

$K_I = 0.66 MPa\sqrt{m}$
$K_{II} = -0.27 MPa\sqrt{m}$
$\frac{K_{II}}{K_I} = 0.41$
$G = 10.1 J/m^2$</td>
<td colspan="2"> 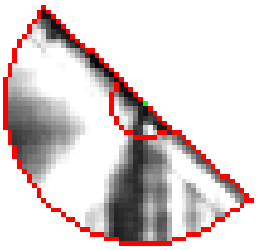

$K_I = 1.28 MPa\sqrt{m}$
$K_{II} = -0.23 MPa\sqrt{m}$
$\frac{K_{II}}{K_I} = 0.18$
$G = 33.2 J/m^2$</td>
</tr>
</table>

Figure 4.2.20 Annular Regions and Regenerated Fringe Patterns for Specimen Shown in Figure 4.2.16

Brief Discussion of the Results for the Specimen Shown in Figure 4.2.16:

Q2 had a higher fringe count than Q1. Q4 had a higher fringe count than Q3. As expected, Q2 had lower mode mixity than Q1, and Q4 had lower mode mixity than Q3. The mathematically regenerated fringe patterns matched well for Q2 and Q3, and were a satisfactory match for Q1 and Q4.

Q2 was also analyzed using false-color fringe multiplication. The numerical results and the corresponding mathematically regenerated fringe pattern match well with what was obtained using the "regular" method. The false-color analysis is thus shown to produce correct results when compared with results from the "regular" method.

The stress intensity factors and energy release rates were not expected to be similar between any quadrants, because each quadrant differed from each other in either fiber direction or fringe count.

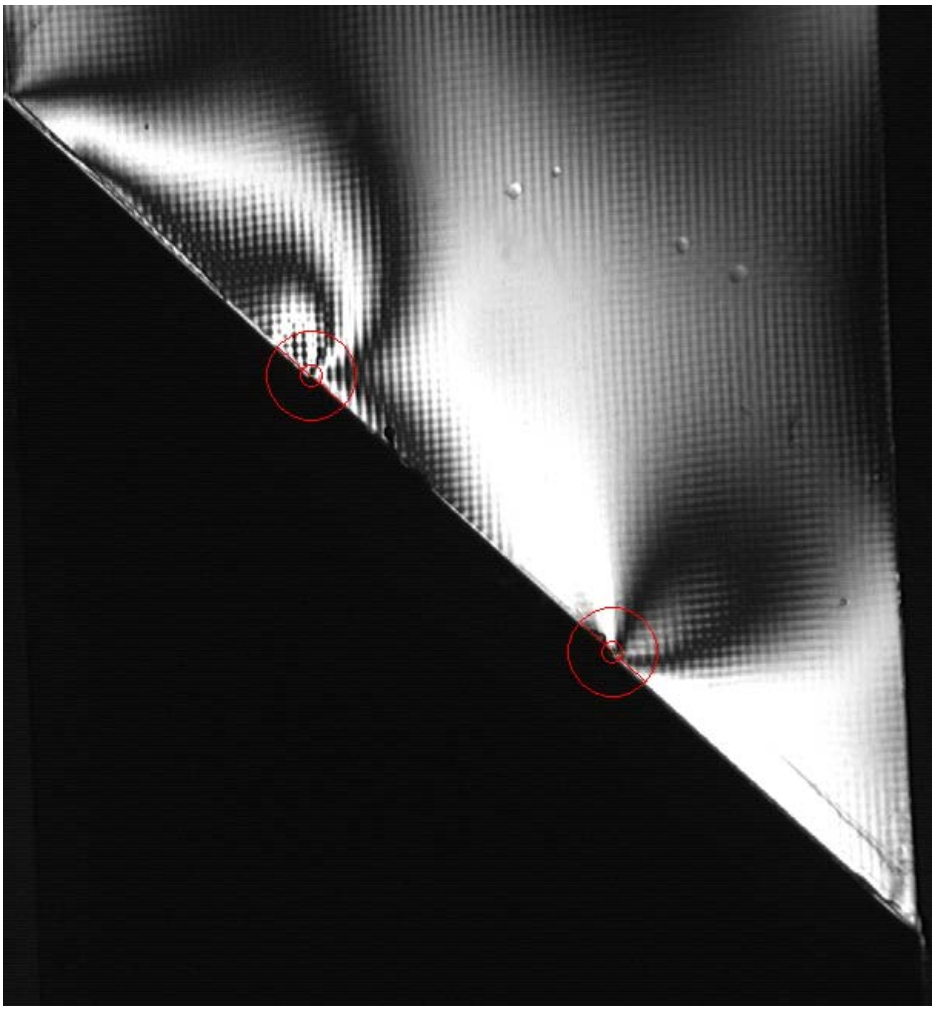

Figure 4.2.21 Interface Angle 45°, 0°/90° Composite – Aluminum Bimaterial, 4kN (900 lb) load, a/w = 0.33, w = 127 mm (5 in.)

2nd Quadrant (0°/90°)	**1st Quadrant (0°/90°)**
  $K_I = 1.67 MPa\sqrt{m}$ $K_{II} = -0.36 MPa\sqrt{m}$ $\frac{K_{II}}{K_I} = 0.22$ $G = 57.3 J/m^2$	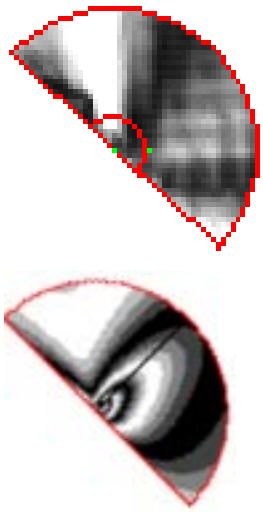 $K_I = 0.60 MPa\sqrt{m}$ $K_{II} = 0.52 MPa\sqrt{m}$ $\frac{K_{II}}{K_I} = 0.87$ $G = 12.4 J/m^2$
4th Quadrant (Aluminum – no fringe pattern)	**3rd Quadrant** (Aluminum – no fringe pattern)

Figure 4.2.22 Annular Regions and Regenerated Fringe Patterns for Specimen Shown in Figure 4.2.21

Brief Discussion of the Results for the Specimen Shown in Figure 4.2.21:

Q3 and Q4 were aluminum and thus no fringe patterns were produced. The fringes inside the annular region for Q2 showed a great deal of texture, thus it was helpful to look at the full-field image to determine the fringe orders. For reference, the fringe ordering and the data points taken are shown in Figure 4.2.23.

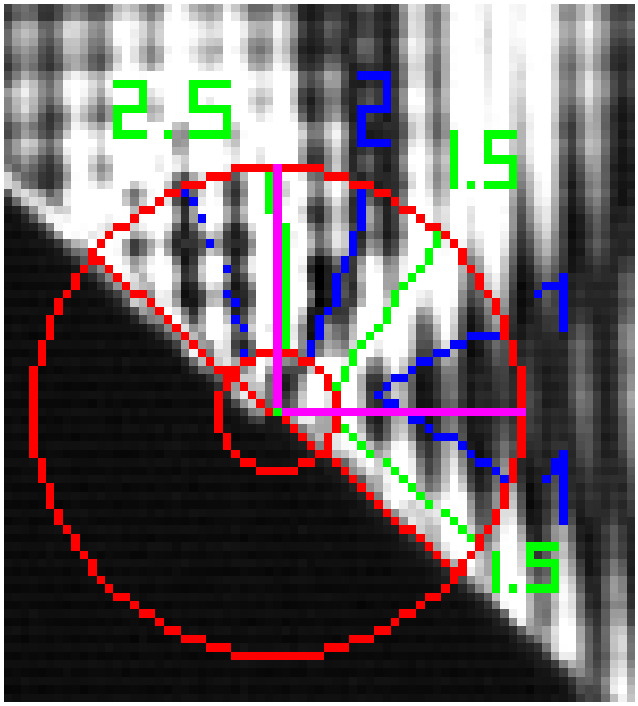

Figure 4.2.23 Fringe Ordering and Data Points taken from Q2 of Specimen in Figure 4.2.21

The fringe count was higher in Q2 than in Q1. The mode mixity in Q2 was lower than in Q1, which followed the established trend. The fringes were satisfactorily regenerated for Q1 and Q2.

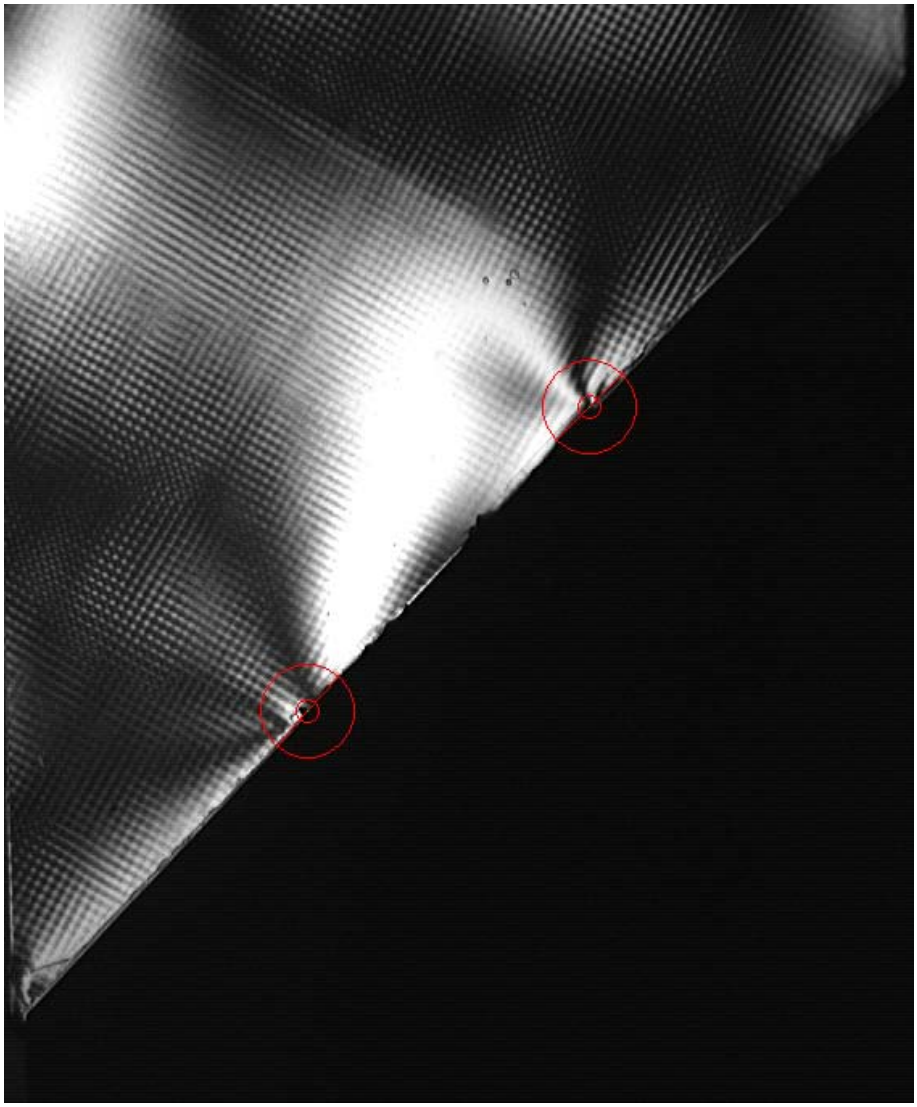

Figure 4.2.24 Interface Angle 45°, 30°/60° Composite – Aluminum Bimaterial, 3.8kN (850 lb) load, a/w = 0.33, w = 127 mm (5 in.)

2nd Quadrant (30°/60°)	**1st Quadrant (30°/60°)**
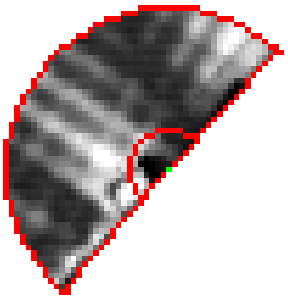 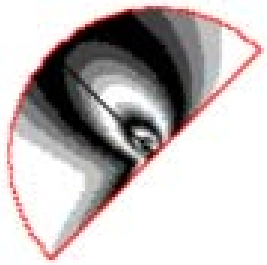 $K_I = 0.40 MPa\sqrt{m}$ $K_{II} = 0.51 MPa\sqrt{m}$ $\frac{K_{II}}{K_I} = 1.28$ $G = 11.9 J/m^2$	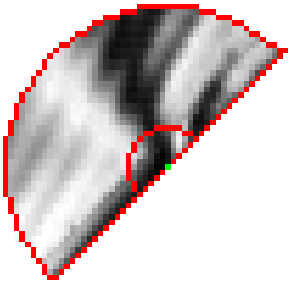 $K_I = 1.35 MPa\sqrt{m}$ $K_{II} = 0.29 MPa\sqrt{m}$ $\frac{K_{II}}{K_I} = 0.21$ $G = 53.5 J/m^2$
4th Quadrant (Aluminum – no fringe pattern)	**3rd Quadrant** (Aluminum – no fringe pattern)

Figure 4.2.25 Annular Regions and Regenerated Fringe Patterns for Specimen Shown in Figure 4.2.24

Brief Discussion of the Results for the Specimen Shown in Figure 4.2.24:

The fringe count was higher in Q1 than in Q2. The fringe patterns were satisfactorily regenerated for both quadrants. Q3 and Q4 were aluminum, so no fringes were produced. As expected from the observed trend, the mode mixity is low in Q1 (which had a high fringe count) and high in Q2 (which had a low fringe count.)

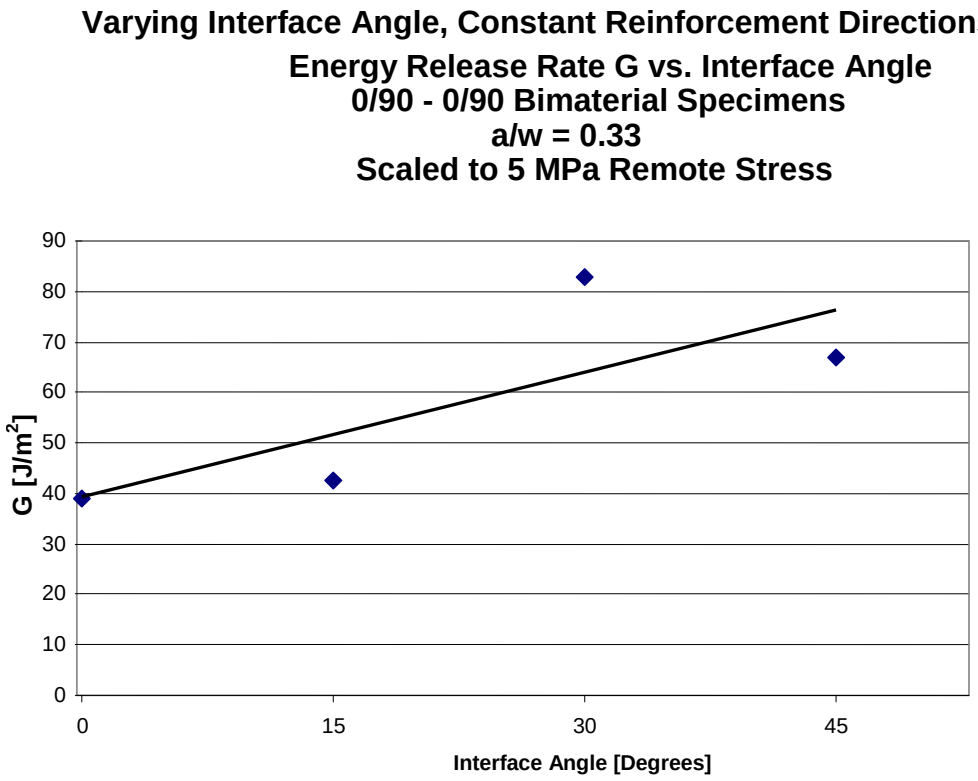

Figure 4.2.26 Energy Release Rate vs. Interface Angle for Bimaterials with Reinforcement Directions of 0/90 Degrees in Both Halves

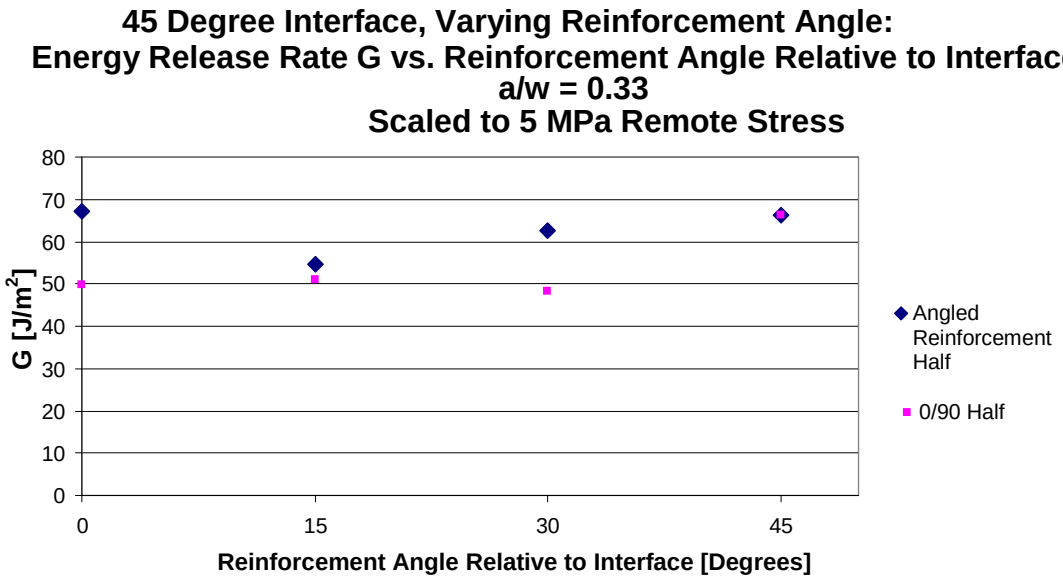

Figure 4.2.27 Energy Release Rate vs. Angle between Reinforcement and Interface, for Bimaterials with 45 Degree Interface Angle, a/w = 0.33

4.2.3 Discussion of Numerical Results

For the graphs, only results from “high” fringe count quadrants were used. Figure 4.2.26 shows what effect varying the interface angle has upon the energy release rate in bimaterial specimens that have reinforcement directions of 0º/90º in both halves. The data points are somewhat scattered, but it is reasonable to state that increasing the interface angle increases the energy release rate.

Figure 4.2.27 shows what effect varying the reinforcement directions has upon energy release rates, for specimens with an interface angle of 45º. The plot shows how the energy release rate changes when the angle between the reinforcement and the interface increases. Overall there appears to be no major influence of reinforcement angle upon energy release rates; though this plot alone only tells part of the story: Consider Figure 4.1.10 which shows what effect varying reinforcement directions has upon energy release rates in bimaterial specimens with horizontal interfaces. That figure shows that the energy release rate *decreases* with increasing angle between reinforcement and interface.

Therefore, Figure 4.2.27 actually shows the *interaction* between interface angle and reinforcement angle. The steeper interface angle tends to increase energy release rates, while the increased angle between reinforcement and interface tends to decrease the energy release rates.

For that reason the effect of varying the angle between reinforcement and interface in angled interface bimaterials appears to be small; however it is reasonable to conclude that the reinforcement angle change offsets the effects of increased bimaterial interface angles.

Finally, the mode mixity varies between quadrants. Quadrants that have a high number of fringes, and corresponding high stress intensities and energy release rates,

show a low degree of mode mixity (that is, K_{II} / K_I), usually around 0.1 - 0.2. Conversely, quadrants that have a low number of fringes, and low stress intensities and energy release rates, show high degrees of mode mixity, usually between 0.4 and 1.

4.2.4 Discussion of False-Color Fringe Multiplication Results

The false-color fringe multiplication (FCFM) was employed in two circumstances. The first circumstance was when an experimental pattern was well regenerated without fringe multiplication. This experimental pattern was then false-color fringe multiplied and regenerated based on the data obtained from the false-color fringe multiplied picture. The results obtained from the multiplied and un-multiplied images were then compared to verify that the false-color fringe multiplication method actually works. This was found to be the case, as demonstrated in Figure 4.2.16 to Figure 4.2.20 : Quadrant 2 was analyzed and regenerated both with data from the original isochromatic fringe patterns and data from the false-color fringe multiplied patterns (using the same values for the location of the crack tip). The regenerated fringe patterns based on results from the original isochromatic fringes and the false-color multiplied fringes both match well with the original isochromatic fringe patterns. The numerical results agree well with each other also, the stress intensity factors vary less than 10%.

FCFM was developed to increase the amount of data that could be extracted from isochromatic fringe patterns. Typically FCFM images allowed 1.5 to 3 times as many data points to be taken from a given isochromatic fringe pattern. The original isochromatic fringe patterns from Quadrant 2 of the specimen shown in Figure 4.2.16 yielded 76 data points, the FCFM image thereof yielded 119 data points.

Interestingly, in the cases where a good fringe pattern could not be regenerated based on data from the original isochromatic fringes, the fringe regeneration also failed when using data obtained from false-color fringe multiplied images.

4.2.5 Fracture Surface Topographic Examination of Angled Interface Bimaterial Specimens

In the same fashion as for horizontal interface bimaterial specimens, the fracture surfaces of some angled interface bimaterial specimens were inspected with a metallurgical microscope. There were interesting results here as well.

Figure 4.2.28 to Figure 4.2.30 show cracks growing from the fracture surface into the bimaterial half. This bimaterial half has reinforcement directions of 0º/90º and an interface angle of 45º. Thus, the fibers are at a 45º angle to the fracture surface. The cracks are growing into the bimaterial half and then grow horizontally. This is also what is expected, cracks that grow along an incline (mixed-mode cracking) try to become horizontally growing cracks, that is, primarily Mode I cracks.

Figure 4.2.31 show the fracture surface of a bimaterial half that also has an interface angle of 45º but reinforcement angles of 30º/60º, the angles between the interface and the fibers are thus much smaller than in the previously examined specimen. The fracture surface looks very different also; it is very smooth, revealing no tendency for the crack to grow into the bimaterial half.

These results correspond with what was observed in the bimaterial specimens with a horizontal interface: If reinforcement fibers are angled relative to the interface, the crack tries to grow into the bimaterial half. If there is little or no angle between the fibers and the interface, the cracks propagate along the interface.

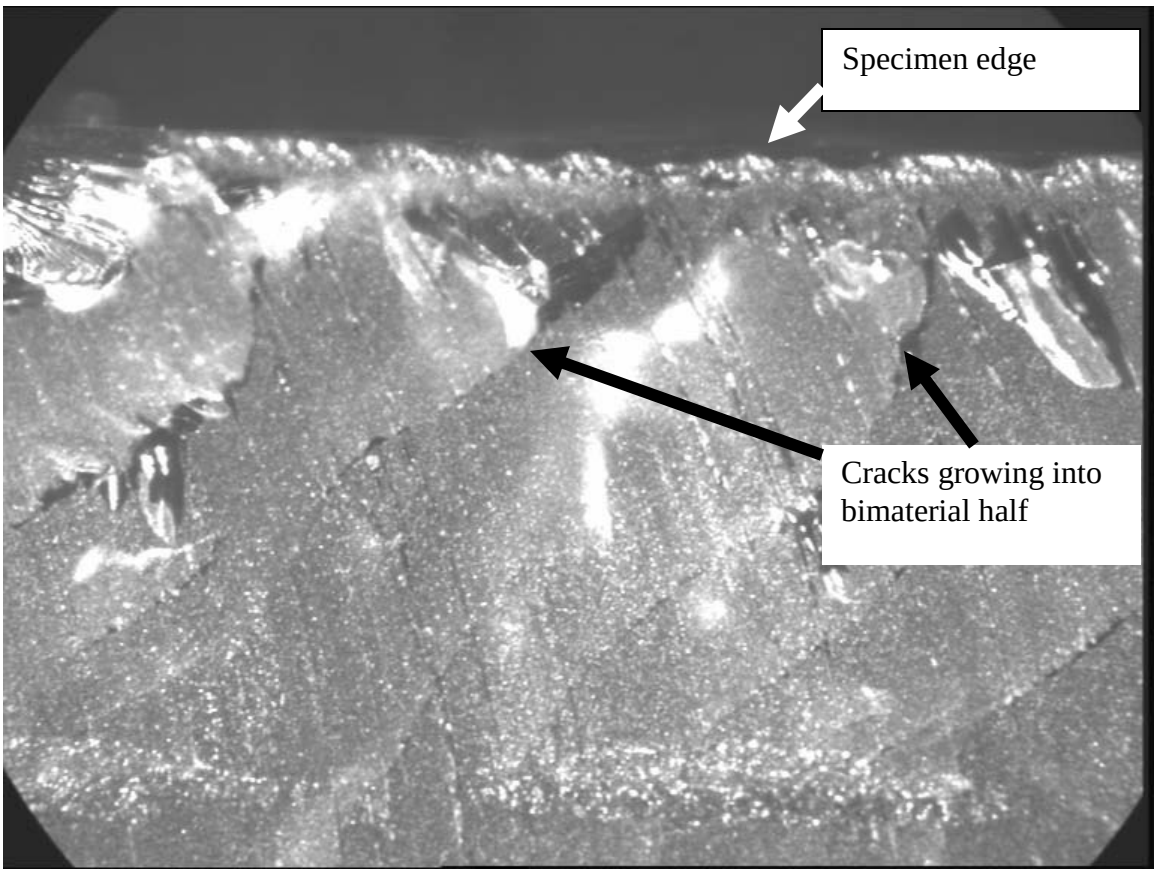

Figure 4.2.28 Fracture Surface (Viewing Fracture Surface Head-On) of Angled Interface Bimaterial Specimen. Interface Angle 45º, Reinforcement Directions 0º/90º

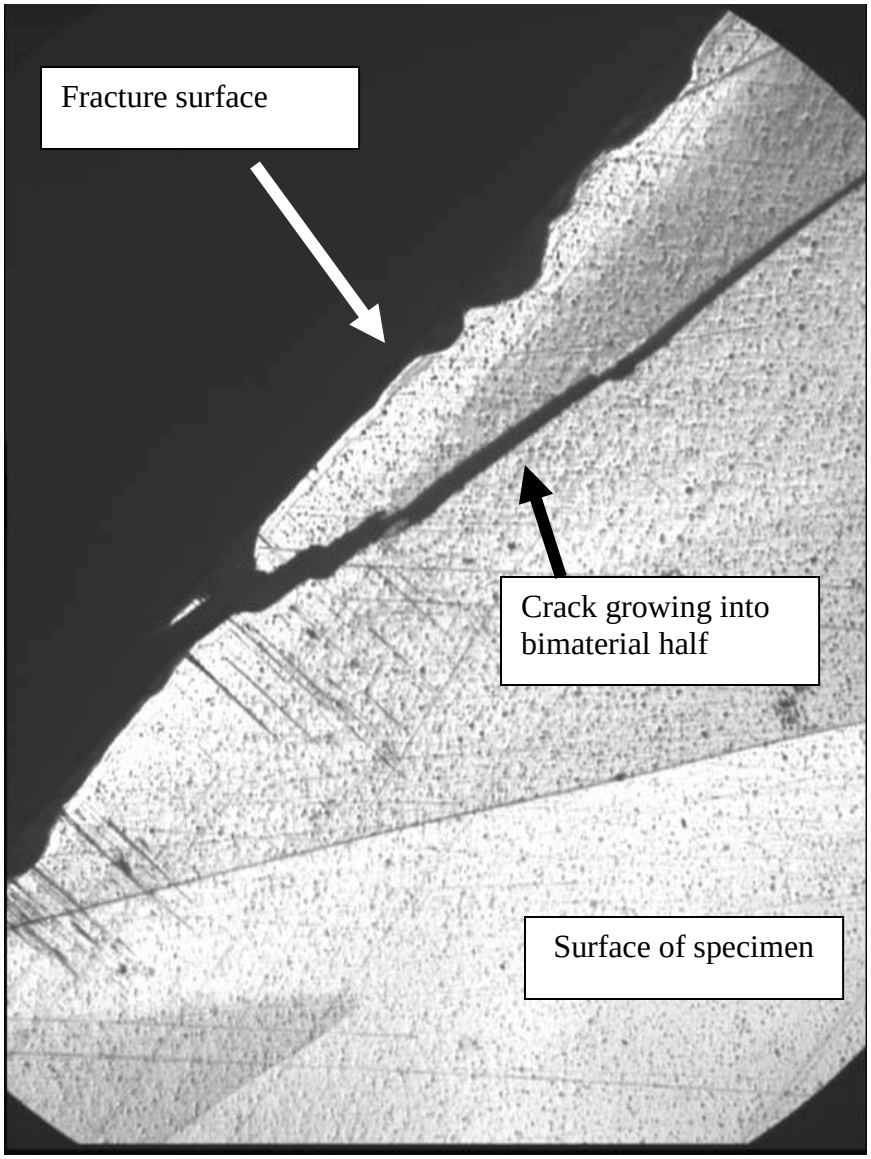

Figure 4.2.29 Side View of Crack Formation Shown in Figure 4.2.28

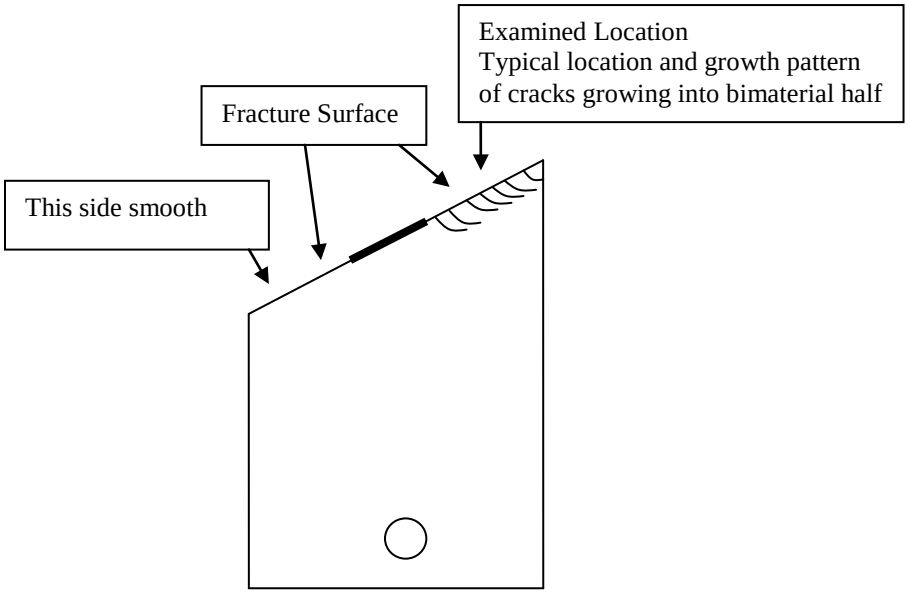

Figure 4.2.30 Schematic of Specimen View and Typical Crack Growth Patterns in Interface Angle 45º, Reinforcement Directions 0º/90º

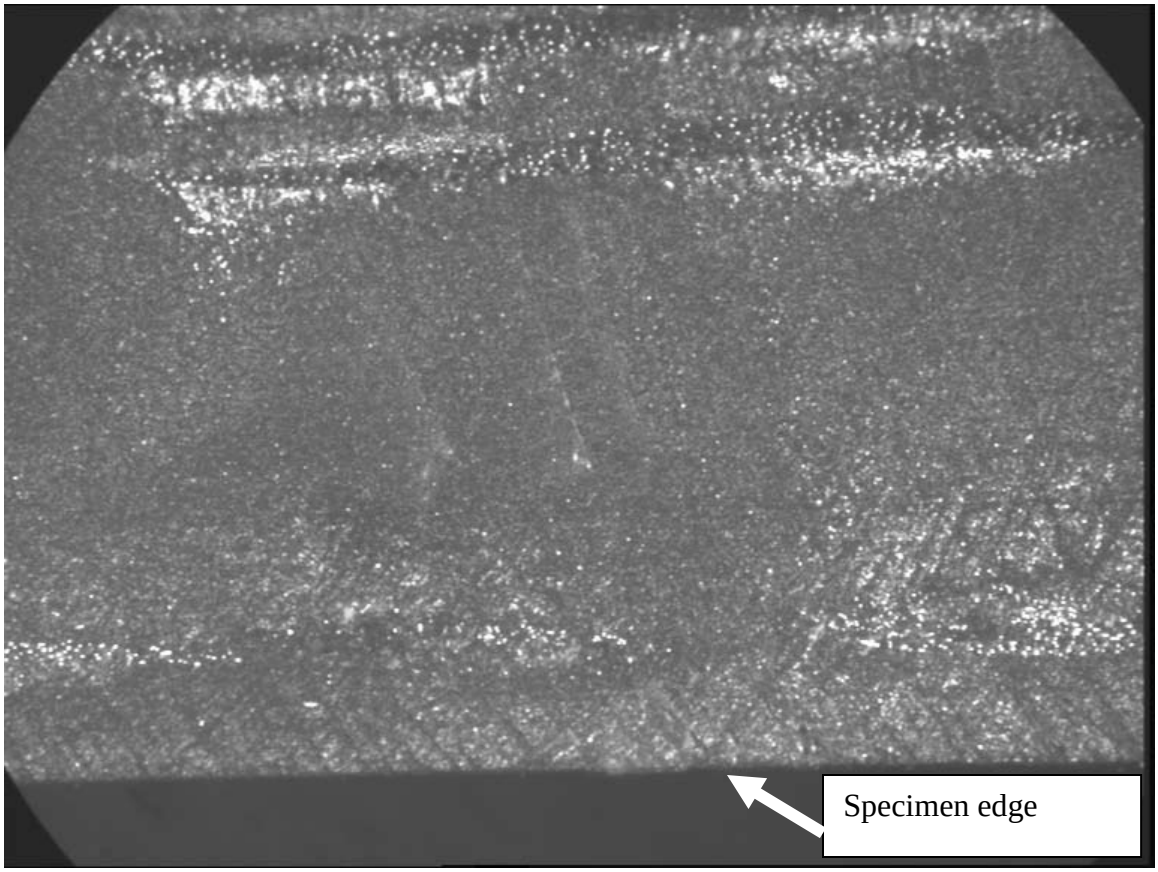

Figure 4.2.31 Fracture Surface (Viewing Fracture Surface Head-On) of Angled Interface Specimen. Interface Angle 45º, Reinforcement Directions 30º/60º

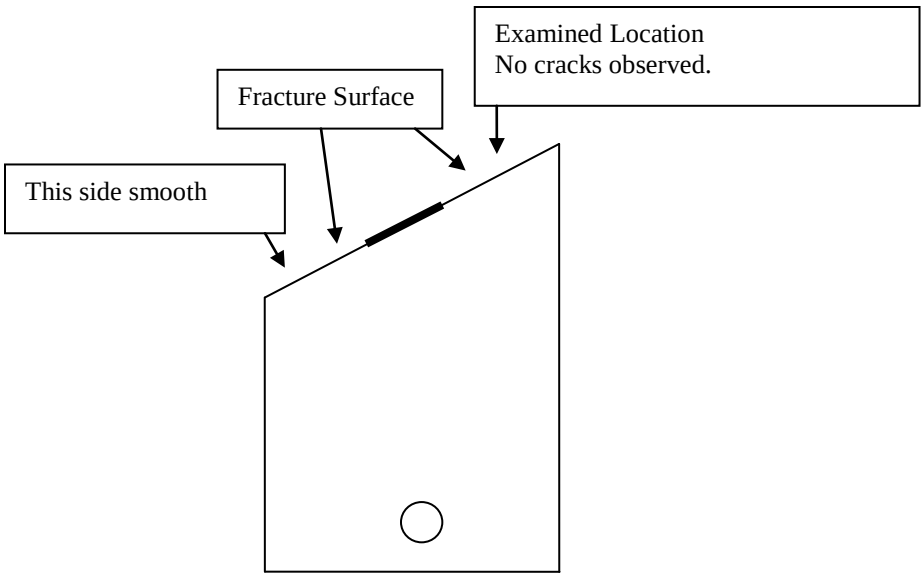

Figure 4.2.32 Schematic of Specimen View and Typical Crack Growth Patterns in Interface Angle 45º, Reinforcement Directions 30º/60º

5 Conclusions

The use of photoelasticity to investigate fracture in orthotropic-orthotropic bimaterials was established.

For fracture in bimaterials with horizontal interfaces, isochromatic fringe patterns were obtained and analyzed. The analyses yielded Mode I and Mode II stress intensity factors. Then the isochromatic fringe patterns were mathematically regenerated. There was very good agreement between the experimentally obtained fringe pattern and their mathematically regenerated counterparts. There is a linear or possibly weakly nonlinear relationship between relative crack length and energy release rates. As the crack length increases, so does the energy release rate. It was also found mathematically that changes in the fiber reinforcement directions in one bimaterial half lead to changes in the energy release rate in *both* bimaterial halves. Furthermore, it was also found that changes in relative crack length caused some changes in mode mixity.

For fracture in angled interface bimaterials there were also multiple successfully analyzed and mathematically regenerated isochromatic fringe patterns. As in the analysis of horizontal interface bimaterials it was found that the angle between reinforcement fibers and the bimaterial interface affects both crack growth directions and energy release rates. In addition, there is interaction between the reinforcement angles and the angle of the interface.

In both specimen types it was experimentally observed that when the reinforcement angles relative to the interface were small (0 - 15º) the cracks tended to grow along the interface. When the reinforcement angles relative to the interface were larger (30º - 45º) the cracks tended to try to grow into the bimaterial half.

Having the crack grow into the bimaterial half is beneficial for several reasons. First of all, the reinforcement is bidirectional so there is always bridging of the crack when it grows in the material rather than in the interface. Second, knowledge of this sort of behavior makes it possible to design composite structures to behave in a similar fashion, making them more resistant to interfacial cracking and potentially catastrophic failure: The structure can be designed to encourage any interfacial cracks to grow into the material rather than along the interface.

False-Color Fringe Multiplication (FCFM) was also established. The method does not introduce any artificially generated fringes or generate any new data; it simply makes more visible the fractional order fringes that are difficult for the human eye to discern. It greatly increases the amount of data that can be extracted from isochromatic fringe patterns.

The establishment of photoelasticity as an investigation method for interfacial fracture in composite-composite bimaterials has also opened new areas of inquiry, as will be discussed in the Future Works section.

6 Future Work

There are several aspects of interfacial fracture in orthotropic-orthotropic bimaterials that warrant investigation in the future. In particular:

6.1 Dynamic Fracture

The use of photoelasticity has already been established in investigations of static and dynamic interfacial fracture in isotropic-isotropic bimaterials. Now photoelasticity has been extended in the current investigation to use in static interfacial fracture in orthotropic-orthotropic bimaterials. A logical extension of this work is to investigate dynamic interfacial fracture in orthotropic-orthotropic bimaterials. Two main areas of investigation are: Dynamic crack growth, and the effect of stress waves impinging upon a stationary crack.

One commonly used specimen configuration is the bimaterial specimen with an interfacial edge crack:

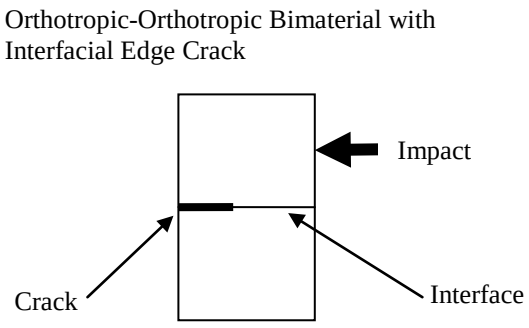

Figure 6.1.1 Specimen Configuration for Dynamic Fracture Studies in Bimaterials

One bimaterial half is impacted, for instance with a gas gun shooting a projectile against the edge of that bimaterial half. What happens upon impact depends on several factors, either the specimen fractures (dynamic crack growth), or the crack remains

stationary but stress waves travel through the bimaterial. In either case dynamic isochromatic patterns can be recorded with a high-speed camera system.

One aspect to investigate is determining the criteria for *when* cracks do propagate upon impact and with what *velocity* the cracks propagate: To they propagate transonically, supersonically; is there shear dominated crack growth or other mechanisms involved?

Another aspect is finding the dynamic stress intensity factors (K_{ID}, K_{IID}), both as functions of time, and as functions of crack velocity. Also, finding K_{ID}, K_{IID} as functions of loading.

6.2 Airy Stress Function – Westergaard Facture Analysis

The stress field equations used in this investigation limited the overdeterministic analysis to using two coefficients. The effects of trying to use more coefficients were demonstrated in Figure 3.5.1, using more coefficients did not improve the appearance of the regenerated fringe patterns. On the contrary, they became completely malformed.

If a suitable Airy stress function can be found then the Westergaard method for fracture analysis can be used, with several benefits as a result. The Westergaard method uses Airy Stress Functions in conjunction with complex variables, and the investigator can choose the number of unknown coefficients to use. Most of the unknown coefficients have no physical meaning, but as was found in a photoelastic investigation of fracture in monolithic composites [116], increasing the number of coefficients improved the accuracy of the analysis. A higher number of coefficients also improved the image regeneration, providing better matches between the observed isochromatic fringes and the mathematically regenerated fringes. Therefore it is reasonable to expect that a

Westergaard approach to bimaterial interface fracture analysis might also yield better matches between observed isochromatic fringes and mathematically regenerated fringes. In addition, it might be possible that a solution with a higher number of terms would allow for using a larger annular region.

Another reason for looking into the Westergaard approach is the sensitivity to crack tip mislocation in the current analysis. The photoelastic analysis of fracture in monolithic composites is quite robust and little sensitivity to crack tip mislocation was encountered, while here it has become a major confounding factor and extremely time-consuming to deal with. The computing time for analyzing and regenerating fringe patterns for the grid overlaying the crack tip area is many hours for each specimen, as explained in section 3.5.2.1.

6.3 Sensitivities, Annular Regions, and Interactions

The size of the annular region is a subject that bears further study. In this investigation a region size was arrived at by some trial and error. The main concern about using a smaller annular region is that this excludes a lot of fringe information; it would be beneficial to find the optimal size for the annular region. Such a region includes as much fringe information as possible while still yielding accurate results and well-regenerated fringes. Thus it would be beneficial to undertake a study specifically to determine the optimum size of the annular region.

The current method's sensitivity to crack tip mislocation has been well established. It would be useful to know if there is a connection between this sensitivity and the number of data points collected; will the crack tip mislocation sensitivity increase or decrease

with a higher number of data points? Also, is there interaction between that sensitivity and the size of the annular region?

Finally, is there a connection or interaction between the size of the annular region and how many data points are needed to obtain accurate results?

6.4 Automated Fringe Data Collection and Fringe Comparison

The manual data collection method has proven to be very time-consuming. Collecting data from one image (that is, one bimaterial specimen under one given load) can easily take an hour. There are some different possible ways to automate this process.

Three-Fringe Photoelasticity (TFP) has been developed for automating data collection, though the presentations thereof concern isotropic materials and relatively simple specimen geometries such as discs in compression [124-126]. However, it is well worth it to investigate if TFP can be extended to transparent composite materials and to more complex specimen geometries.

Geographic Information Systems (GIS) are widely used in situations analogous to analysis of isochromatic fringe patterns. Satellite images of land areas are computer analyzed based on color; various colors represent various types of land, such as soybean fields, corn fields, bracken land, forest, etc. Combinations of visible-light and infrared-light images are used to map the spread of plant-specific diseases: Trees infected by fungi appear slightly different than healthy trees, in ways too subtle for the human eye to see, but GIS captures these and make them visible with false color.

Such software should be possible to adapt to analysis of isochromatic fringes; perhaps with user assistance in determining the order of a specific fringe (while the software then follows the central contour of that fringe, recording the positions relative to the crack tip.)

Finally, such software could conceivably be adapted to compare the regenerated fringes with the experimentally obtained fringe patterns. Currently, this is a manual process, also very time consuming, on the order of several hours per specimen.

REFERENCES

Papers Presenting Analytical Methods and Equations:

1. Williams, M.L., 1959,"The Stresses Around a Fault or Crack in Dissimilar Media", Bulletin of the Seismological Society of America, **49**, (2), pp. 199-203
2. England, A.H., 1965, "A crack between dissimilar media", Journal of Applied Mechanics, **32**, pp. 400-402
3. Rice, J.R., 1988, "Elastic Fracture Mechanics Concepts for Interfacial Cracks", Journal of Applied Mechanics, **55**, pp. 98-103
4. Qu, J., Bassani, J.L., 1989, "Cracks on Bimaterial and Bicrystal Interfaces", Journal of the Mechanics and Physics of Solids, **37**, (4), pp. 417-433
5. Bassani, J.L., Qu, J., 1989, "Finite Crack on Bimaterial and Bicrystal Interfaces", Journal of the Mechanics and Physics of Solids, **37**, (4), pp. 435-453
6. Sun, C.T., Manoharan, M.G., 1989, "Strain Energy Release Rates of an Interfacial Crack Between Two Orthotropic Solids", Journal of Composite Materials, **23**, pp. 460-478
7. Sun, C.T., Manoharan, M.G., 1990, "Strain Energy Release Rates of an Interfacial Crack between Two Anisotropic Solids under Uniform Axial Strain, Composites Science and Technology, **39**, pp. 99-116
8. Wu, K-H., 1990, "Stress Intensity Factor and Energy Release Rate for Interfacial Cracks Between Dissimilar Anisotropic Materials", Journal of Applied Mechanics, **57**, pp. 882-886
9. Evans, A.G., Rühle, M., Dalgleish, B.J., Charalambides, P.G., 1989, "The Fracture Energy of Bimaterial Interfaces", Materials Science and Engineering, **A126**, pp. 53-64
10. Comninou, M., 1990, "An Overview of Interface Cracks", Engineering Fracture Mechanics, **37**, (1), pp. 197-208
11. Nakhmein, E.L., Nuller, B.M., 1990, "Dynamic Contact Problems for an Orthotropic Elastic Half-Plane and a Composite Plane", Prikl. Matem. Mekhan. U.S.S.R., English Translation, **54**, (4), pp. 523-530
12. Gao, H., 1991, "Weight Function Analysis of Interface Cracks: Mismatch Versus Oscillation", Journal of Applied Mechanics, **58**, pp. 931-938
13. Ma, C-C., Luo, J-J., 1993, "Analysis of the Interfacial Crack for Anisotropic Materials under Displacement-Displacement or Traction-Displacement Boundary Conditions", Journal of Applied Mechanics, **60**, pp. 777-781
14. Deng, X., 1993, "General Crack-Tip Fields for Stationary and Steadily Growing Interface Cracks in Anisotropic Bimaterials", Journal of Applied Mechanics, **60**, pp. 183-189
15. Lee, J., Gao, H., 1994, "A Generalized Comninou Contact Model for Interface Cracks in Anisotropic Elastic Solids", International Journal of Fracture, **67**, pp. 53-68

16. Deng, X, 1994, “An Asymptotic Analysis of Stationary and Moving Cracks with Frictional Contact Along Bimaterial Interfaces and in Homogeneous Solids”, International Journal of Solids and Structures, **31**, (17), pp. 2407-2429
17. Deng, X.., 1995, “Mechanics of Debonding and Delamination in Composites: Asymptotic Studies”, Composites Engineering, **5**, (10-11), pp. 1299-1315
18. Liu, C., Huang, Y., Rosakis, A.J., 1995, ”Shear Dominated Transonic Interfacial Crack Growth in a Bimaterial – II. Asymptotic Fields and Favorable Velocity Regimes”, Journal of the Mechanics and Physics of Solids, **43**, (2), pp. 189-206
19. Wang, T., 1996, “Micromechanics Analyses of Interface Crack”, Acta Mechanica Sinica (English Series), **12**, (1), pp. 47-54
20. Jha, M., Charalambides, P.G., Ballarini, R., 1997, “Near-Tip Mode-I Elastic Fields in Bimaterial Layered Systems”, International Journal of Solids and Structures, **34**, (15), pp. 1849-1871
21. Hu, Y., Huang, Y., Zhong, W., 1997, “Collinear Periodic Cracks in Anisotropic Bimaterials”, International Journal of Fracture, **85**, pp. 69-80
22. Hurang, H., Chengping, W., 1997, “A New Approach to Predicting Interfacial Crack Growth”, Applied Mathematics and Mechanics, English Edition, **18**, (1), pp. 37-44
23. Dundurs, J., Sotiropoulos, D.A., 1998, “On Stress Conditions and Computations at Bi-Material Interfaces”, Computational Mechanics, **21**, pp. 300-305
24. Shen, S., Kuang, Z-B., 1998, “Wave Scattering from an Interface Crack in Laminated Anisotropic Media”, Mechanics Research Communications, **25**, (5), pp. 509-517
25. Duduchava, R., Sändig, A.M., Wendland, W.L., 1999, “Interface Cracks in Anisotropic Composites, Mathematical Methods in the Applied Sciences, **22**, pp. 1413-1446
26. Kuang, J.S., Wang, Y.H., 1999, “Analysis of Interfacial Cracks Emanating from a Hole in a Bimaterial Plate”, European Journal of Mechanics A/Solids, **18**, pp. 465-479
27. Ma, C-C., Liao, C-Y., 1999, “Elastodynamic Analysis of Antiplane Anisotropic Interface Cracks”, Journal of Engineering Mechanics, **August,** pp.891-898
28. Ueda, S., 2000, “Dynamic Singular Stresses in Glassfiber Reinforced Plastics with a Broken Layer at Low Temperatures”, International Journal of Fracture, **106**, pp. 13-31
29. Ni, L., Nemat-Nasser, S., 2000, “Bridged Interface Cracks in Anisotropic Bimaterials”, Philosophical Magazine A, **80**, (11), pp. 2675-2693
30. Chaudhuri, R.A., Xie, M., 2000, “A Tale of Two Saints: St. Venant and ‘St. Nick’ – Does St. Venant’s Principle Apply to Bi-Material Straight-Edge and Wedge-Singularity Problems?”, Composites Science and Technology, **60**, pp. 2503-2515
31. Lee, K.H., 2000, “Stress and Displacement Fields for Propagating the Crack Along the Interface of Dissimilar Orthotropic Materials Under Dynamic Mode I and II Load”, Journal of Applied Mechanics, **67**, pp. 223-228
32. Lee, K.H., Hawong, J.S., Choi, S.H., 1996, “Dynamic Stress Intensity Factors K_I, K_{II}, and Dynamic Crack Propagation Characteristics of Orthotropic Materials”, Engineering Fracture Mechanics, **53**, (1), pp. 119-140

33. Huang, Y., Gao, H., 2001, “Intersonic Crack Propagation – Part I: The Fundamental Solution”, Journal of Applied Mechanics, **68**, pp. 169-175
34. Xu, J-Q., Wang, X-G., Mutoh, Y., 2001, “Stress Intensity Factors of a Surface Crack Near an Interface End”, International Journal of Fracture, **111**, pp. 251-264
35. Brock, L.M., 2002, “Interface Crack Extension at any Constant Speed in Orthotropic or Transversely Isotropic Bimaterials I – General Exact Solutions”, International Journal of Solids and Structures, **39**, pp. 1165-1182
36. Brock, L.M., Hanson, M.T., 2002, “Interface Crack Extension at any Constant Speed in Orthotropic or Transversely Isotropic Bimaterials II – Two Important Examples”, International Journal of Solids and Structures, **39**, pp. 1183-1198
37. Guo, C., Sun, C.T., 2003, “Stationary and Moving Interface Cracks with Contact in Anisotropic Bimaterials, The Chinese Journal of Mechanics – Series A, **19**, (1), pp. 31-39
38. Xu, J-Q, Mutoh, Y., 2003, “Analytical Solution for Interface Stresses due to Concentrated Surface Force”, International Journal of Mechanical Sciences, **45**, pp. 1877-1892
39. Wang, J., Qiao, P., 2004, “Interface Crack Between Two Shear Deformable Elastic Layers”, Journal of the Mechanics and Physics of Solids, **52**, pp. 891-905
40. Liu, L., Kardomateas, G.A., Holmes, J.W., 2004, “Mixed-Mode Stress Intensity Factors for a Crack in an Anisotropic Bimaterial Strip”, International Journal of Solids and Structures, **41**, pp. 3095-3107
41. Hasebe, N., Wang, X., Okumura, M., 2004, “Conditions for Cracking and Debond Development at Partially Bonded Bimaterial Half-Planes”, Mechanics of Composite Materials, **40**, (4), pp. 287-298
42. Shin, K.C., Liu, H., Lee, J.J., Choi, S.T., 2004, “Interfacial Crack Tip Field in Anisotropic/Isotropic Bimaterials”, Composite Structures, **66**, 673-676
43. Herrmann, K.P., Loboda, V.V., Komarov, A.V., 2004, ”Contact Zone Assessment for a Fast Growing Interface Crack in an Anisotropic Bimaterial”, Archive of Applied Mechanics, **74**, pp. 118-129
44. Kattis, M.A., Papanikos, P., Providas, E., 2004, ”Thermal Green’s Functions in Plane Anisotropic Bimaterials”, Acta Mechanica, **173**, pp. 65-76
45. Yin, W-L, 2005, “Green's Function of Bimaterials Comprising All Cases of Material Degeneracy”, International Journal of Solids and Structures, **42**, pp. 1-19
46. Brock, L.M., 2005, “The Coupled Thermoelastic Transversely Isotropic Bimaterial: Interface Crack Extension”, Journal of Applied Mechanics, **72**, pp. 68-75
47. Prasad, P.B.N., Hasebe, N., Wang, X.F., Shirai, Y., 2005, “Green’s Function of a Bimaterial with a Cavity on the Interface – Part I: Theory”, Journal of Applied Mechanics, **72**, pp. 389-393
48. Prasad, P.B.N., Hasebe, N., Wang, X.F., 2005, “Interaction Between Interfacial Cavity/Crack and Internal Crack – Part II: Simulation”, Journal of Applied Mechanics, **72**, pp. 394-399

49. Wang, J., Qiao, P., 2005, “Mechanics of Bimaterial Interface: Shear Deformable Split Bilayer Beam Theory and Fracture”, Journal of Applied Mechanics, **72**, pp. 674-682
50. Chaudhuri, R., 2006, “Three-Dimensional Asymptotic Stress Field in the Vicinity of the Circumference of a Bimaterial Penny-Shaped Interfacial Discontinuity”, International Journal of Fracture, **141**, pp. 211-225
51. Sudak, L.J., Wang, X., 2006, “Green's Function in Plane Anisotropic Bimaterials with Imperfect Interface”, Journal of Applied Mathematics, **71**, 783-794
52. Guo, S., Dillard, D.A., Nairn, J.A., 2006, “Effect of Residual Stress on the Energy Release Rate of Wedge and DCB Test Specimens”, International Journal of Adhesion & Adhesives, **26**, pp. 285-294
53. Agrawal, A.., Karlsson, A.M., 2006, Obtaining Mode Mixity for a Bimaterial Interface Crack Using the Virtual Crack Closure Technique”, International Journal of Fracture, **141**, pp. 75-98
54. Wu, K-H., Chen, S-H., 2007, “Transient Motion of an Anisotropic Elastic Bimaterial Due to a Line Source”, International Journal of Solids and Structures, **44**, pp. 2269-2284
55. Zhang, Z., Suo, Z., 2007, “Split Singularities and the Competition Between Crack Penetration and Debond at a Bimaterial Interface”, International Journal of Solids and Structures”, **44**, pp. 4559-4573
56. Wang, X., Pan, E., Feng, W.J., 2007, “Time-Dependent Green's Functions for an Anisotropic Bimaterial with Viscous Interface”, European Journal of Mechanics A / Solids, **26**, pp. 901-908
57. Liu, C-I., Chue, C-H., 2007, “Disappearance Conditions of Stress Singularities for Anisotropic Bimaterial Half-Plane Wedges Under Antiplane Shear”, Journal of Applied Mechanics, **74**, pp. 1-7
58. Kozinov, S.V., Loboda, V.V., Kharun, I.V., 2007, “Periodic Set of the Interface Cracks With Contact Zones in an Anisotropic Bimaterial Subjected to a Uniform Tension-Shear Loading”, International Journal of Solids and Structures, **44**, pp. 4646-4655
59. Ru, C.Q., 2008, “A Hybrid Complex-Variable Solution for Piezoelectric/Isotropic Elastic Interfacial Cracks”, International Journal of Fracture, **152**, pp. 169-178
60. Hou, P-F., Leung, A.Y.T., He, Y-J, 2008, “Three-Dimensional Green's Functions for Transversely Isotropic Thermoelastic Bimaterials”, International Journal of Solids and Structures, **45**, pp. 6100-6113
61. Ma, C-C., Wu, W-C., Lee, J-M., 2008, “Full-Field Analysis and Image Forces for Piezoelectric Bimaterials”, Acta Mechanica, **195**, pp. 275-294
62. Karkamkar, N.,, Bose, B., McLaughlin, P., Santhanam, S., 2008, “The Use of Interlayers in Modeling Interface Crack Propagation”, Engineering Fracture Mechanics, **75**, pp. 5087-5100
63. Ting, T.C.T., 2009, “Steady Waves in an Anisotropic Elastic Layer Attached to a Half-Space or Between Two Half-Spaces – A Generalization of Love Waves and Stoneley Waves”, Mathematics and Mechanics of Solids, **14**, pp. 52-71

64. Wang, J., Karihaloo, B.L., 1994, “Mode II and Mode III Stress Singularities and Intensities at a Crack Tip Terminating on a Transversely Isotropic-Orthotropic Bimaterial Interface”, Proceedings of the Royal Society of London A, **444**, pp. 447-460

Papers Primarily Using Numerical Methods:

65. Cho, S.B., Lee, K.B., Choy, Y.S., Yuuki, R., 1992, “Determination of Stress Intensity Factors and Boundary Element Analysis for Interface Cracks in Dissimilar Anisotropic Materials”, Engineering Fracture Mechanics, **43**, (4), pp. 603-614
66. Lo, C.Y., Nakamura, T., Kushner, A., 1994, “Computational Analysis of Dynamic Crack Propagation Along a Bimaterial Interface”, International Journal of Solids and Structures, **31**, (2), pp. 145-168
67. Akisanya, A.R., Fleck, N.A., 1997, “Interfacial Cracking from the Free-Edge of a Long Bimaterial Strip”, International Journal of Solids and Structures, **34**, (13), pp. 1645-1665
68. Berger, J.R., Tewary, V.K., 1997, “Boundary Integral Formulation For Interface Cracks in Anisotropic Bimaterials”, Computational Mechanics, **20**, pp. 261-266
69. Sun, C.T., Qian, W., 1997, “The Use of Finite Extension Strain Energy Release Rates in Fracture of Interfacial Cracks”, International Journal of Solids and Structures, **34**, (20), pp. 2595-2609
70. Lee, Y-D., Erdogan, F., 1998, “Interface Cracking of FGM Coatings Under Steady-State Heat Flow”, Engineering Fracture Mechanics, **59**, (3), pp. 361-380
71. Sun, C. T., Qian, W., 1998, “A Treatment of Interfacial Cracks in the Presence of Friction”, International Journal of Fracture, **94**, pp. 371-382
72. Chen, Y-H., Hasebe, N., 1998, “A Consistency Check for Strongly Interacting Multiple Crack Problems in Isotropic, Bimaterial, and Orthotropic Bodies”, International Journal of Fracture, **89**, pp. 333-353
73. Qian, W., Sun, C.T., 1998, “Methods for Calculating Stress Intensity Factors for Interfacial Cracks Between Two Orthotropic Solids”, International Journal of Solids and Structures, **35**, (25), pp. 3317-3330
74. Xu, J-Q., Liu, Y-H., Wang, X-G., 1999, “Numerical Methods for the Determination of Multiple Stress Singularities and Related Stress Intensity Coefficients”, Engineering Fracture Mechanics, **63**, pp. 775-790
75. Haixiao, L., Chuhan, Z., 2003, “Internal Stress Calculation in 2D Time Domain BEM for Wave Propagation in Anisotropic Media”, Communications in Numerical Methods in Engineering, **19**, pp. 637-643
76. Nagashima, T., Omoto, Y., Tani, S., 2003, “Stress Intensity Factor Analysis of Interface Cracks Using X-FEM”, International Journal for Numerical Methods in Engineering, **56**, pp. 1151-1173
77. Mahanta, B.B., Chakraborty, D., Dutta, A., 2004, “Accurate Prediction of Delamination in FRP Composite Laminates from Transverse Impact”, Composites Science and Technology, **64**, pp. 2341 – 2351

78. Kaye, R., Heller, M., 2006, “Finite Element-Based Three-Dimensional Stress Analysis of Composite Bonded Repairs to Metallic Aircraft Structure”, International Journal of Adhesion & Adhesives, **26**, pp. 261-273
79. Hosseini-Toudeshky, H., Mohammadi, B., Daghyani, H.R., 2006, “Mixed-Mode Fracture Analysis of Aluminium Repaired Panels Using Composite Patches”, Composites Science and Technology, **66**, pp 188-198
80. Xuan, Z., Feng, Z., Gao, D.Y., 2007, “Computing Lower and Upper Bounds on Stress Intensity Factors in Bimaterials”, International Journal of Non-Linear Mechanics, **42**, pp. 336-341
81. Xu, C-H., Qin, T-Y., Noda, N-A., 2007, “Numerical Solutions of Singular Integral Equations for Rectangular Interfacial Crack in Three Dimensional Bimaterials”, Applied Mathematics and Mechanics (English Edition), **28**, (6), pp. 751-757
82. Roham, S., Hight, T., 2007, “Role of Residual Stress on Crack Penetration and Deflection at a Bimaterial Interface in a 4-Point Bend Test, Microelectronics Engineering, **84**, pp. 72-79
83. Ayatollahi, M.R., Hashemi, R., 2007, “Computation of Stress Intensity Factors (*K*I, *K*II) and T-Stress for Cracks Reinforced by Composite Patching”, Composite Structures, **78**, pp. 602-609
84. Zhao, MH., Li, N., Fan, CY., 2008, “Solution Method of Interface Cracks in Three-Dimensional Transversely Isotropic Piezoelectric Bimaterials”, Engineering Analysis with Boundary Elements, **32**, pp. 545-555
85. Yang, Z.J., Deeks, A.J., 2008, “Calculation of Transient Dynamic Stress Intensity Factors at Bimaterial Interface Cracks Using a SBFEM-Based Frequency-Domain Approach”, Science in China Series G: Physics, Mechanics & Astronomy, **51**, (5), pp. 519-531
86. Profant, T., Sevecek, O., Kotoul, M., 2008, “Calculation of K-Factor and T-Stress for Cracks in Anisotropic Bimaterials”, Engineering Fracture Mechanics, **75**, pp. 3707-3726
87. Ma, S., Beroza, G.C., 2008, “Rupture Dynamics on a Bimaterial Interface for Dipping Faults”, Bulletin of the Seismological Society of America, **98**, (4), pp. 1642-1658
88. Freed, Y., Banks-Sills, L., 2008, “A New Cohesive Zone Model for Mixed-Mode Interface Fracture in Bimaterials”, Engineering Fracture Mechanics, **75**, pp. 4583-4593
89. Menshykov, O.V., Menshykov, V.A., Guz, I.A., 2009, “Elastodynamics of a Crack on the Bimaterial Interface”, Engineering Analysis with Boundary Elements, **33**, pp. 294-301
90. Nomura, Y. Ikeda, T., Miyazaki, N., 2009, “Stress Intensity Factor Analysis at an Interfacial Corner Between Anisotropic Bimaterials Under Thermal Stress”, Engineering Fracture Mechanics, **76**, pp. 221-235

Papers Discussing Specimen Configurations:

91. Suo, Z., 1990, “Delamination Specimens for Orthotropic Materials”, Journal of Applied Mechanics, **57**, pp. 627-634

92. O'Dowd, N.P., Shih, C.F., Stout, M.G., 1992, "Test Geometries for Measuring Interfacial Fracture Toughness", International Journal of Solids and Structures, **29**, (5), pp. 571-589
93. Hutchinson, J.W., Suo, Z., 1992, "Mixed Mode Cracking in Layered Materials", *Advances in Applied Mechanics*, **29**, pp. 64-163
94. Kim, Y-J., Budden, P.J., 2001, "Plastic η Factor Solution of Homogeneous and Bi-Material SE(T) Specimens for Toughness and Creep Crack Growth Testing", Fatigue and Fracture Engineering of Materials and Structures, **24**, pp. 751-760
95. Zhang, S., 2001, "T-Stress and Stress Intensities for the Interface Cracks in Some Specimen-Relevant Geometries", International Journal of Fracture, **111**, pp. L23-L28

Papers Reporting Actual Experiments:

96. Sampson, R.C., 1970, "A Stress-Optic Law for Photoelastic Analysis of Orthotropic Composites", Experimental Mechanics, **10**, (5), pp. 210-215
97. Sanford, R.J., Dally, J.W., 1979, "A general method for determining mixed-mode stress intensity factors from isochromatic fringe patterns", Engineering Fracture Mechanics, **11**, pp. 621-633
98. Dally, J.W., Sanford, R.J., 1978, "Classification of stress intensity factors from isochromatic fringe patterns", Experimental Mechanics, **18**, (12), pp. 441-448
99. Dally, J.W., 1979, "Dynamic photoelastic studies of fracture", Experimental Mechanics, **19**, (10), pp. 349-361
100. Gdoutos, E.E., Papakaliatakis, G., 1982, "Photoelastic Study of a Bimaterial Plate with a Crack along the Interface", Engineering Fracture Mechanics, **16**, (2), pp. 177-187
101. Prabhakaran, R., 1982, "Photo-orthotropic elasticity: a new technique for stress analysis of composites", Optical Engineering, **21**, (4), pp. 679-688
102. Lu, H., Chiang, F.P., 1993, "Photoelastic Determination of Stress Intensity Factor of an Interfacial Crack in a Bi-material", Journal of Applied Mechanics, **60**, pp. 93-100
103. Lambros, J., Rosakis, A.J., 1995, "Shear Dominated Transonic Interfacial Crack Growth in a Bimaterial – I. Experimental Observations", Journal of the Mechanics and Physics of Solids, **43**, (2), pp. 169-188
104. Singh, R.P., Shukla, A., 1996, "Characterization of isochromatic fringe patterns for a dynamically propagating interface crack", International Journal of Fracture, **76**, pp. 293-310
105. Singh, R.P, Lambros, J., Shukla, A., Rosakis, A.J., 1997, "Investigation of the mechanics of intersonic crack propagation along a bimaterial interface using coherent gradient sensing and photoelasticity", Proceedings of the Royal Society of London, **A, 453**, pp. 2649-2667
106. Shukla, A., Kavaturu, M., 1998, "Opening-Mode Dominated Crack Growth Along Inclined Interfaces: Experimental Observations", International Journal of Solids and Structures, **35**, (35), pp. 3961-3975

107. Haixiao, L., Chuhan, Z., Zheng, L., Xtreng, Z., 1999, "Photoelastic Studies for Composite Dynamics", Journal of Materials Science, **34**, pp. 3479-3487
108. Soh, A-K., 1999, "An improved photo-elastic technique for determining the mixed-mode stress-intensity factors for interfacial cracks in a bi-material", Composites Science and Technology, **59**, pp. 1033-1039
109. Mohammed, I., Liechti, K.M., 2000, "Cohesive Zone Modeling of Crack Nucleation at Bimaterial Corners", Journal of the Mechanics and Physics of Solids, **48**, 735-764
110. Hawong, J.S., Shin, D.C., Lee, O.S., Lee, H.J., Ha, J.K., 2000, "A Study on the Development of the Dynamic Photoelastic Experimental Method for Isotropic/Orthotropic Bimaterials", Key Engineering Materials, **183-187**, pp. 283-288
111. Shukla, A., 2001, "High-speed fracture studies on bimaterial interfaces using photoelasticity – a review", Journal of Strain Analysis for Engineering Design, **36**, (2), pp. 119-142
112. Gurumurthy, C.K., Kramer, E.J., Hui, C-Y., 2001, "Water-Assisted Sub-Critical Crack Growth Along an Interface Between Polyimide Passivation and Epoxy Underfill", International Journal of Fracture, **109**, pp. 1-28
113. Ricci, V., Shukla, A., Chalivendra, V.B., Lee, K.H., 2003, "Subsonic Interfacial Fracture Using Strain Gages in Isotropic-Orthotropic Bimaterial", Theoretical and Applied Fracture Mechanics, **39**, pp. 143-161
114. Ricci, V., Shukla, A., Kavaturu, M., 2003, "Using Strain Gages to Investigate Subsonic Dynamic Interfacial Fracture in an Isotropic-Isotropic Bimaterial", Engineering Fracture Mechanics, **70**, 2003, pp. 1303-1321
115. Coker, D., Rosakis, A.J., Needleman, A., 2003, "Dynamic crack growth along a polymer composite – Homalite interface", Journal of the Mechanics and Physics of Solids, **51**, pp. 425-460
116. Khanna, S.K., Ellingsen, M.D., Winter, R.M., 2004, "Investigation of Fracture in Transparent Glass Fiber Reinforced Polymer Composites Using Photoelasticity", ASME Journal of Engineering Materials and Technology, **126**, (1), pp. 1-7
117. Dally, J.W., Riley, W.F., 2005, *Experimental Stress Analysis*, 4th Ed., College House Enterprises, Knoxville, TN, USA, pp 401-486
118. Banks-Sills, L., Freed, Y., Eliasi, R., Fourman, V., 2006, "Fracture Toughness of the +45° / -45° Interface of a Laminate Composite", International Journal of Fracture, **141**, pp. 195-210
119. Rozenburg, K., Berger, J.R., Martin, P.A., Reimanis, I., 2007,"Analysis of Moirè Data for Near-Interface Cracks", International Journal of Fracture, **143**, pp. 207-217
120. Papadopoulos, G.A., Kravaritis, J., Badalouka, B., 2008, "Crack-Tip Principal Stresses by Isochromatic and Isopachic Fringes at a Bi-Material Interface", International Journal of Fracture, **148**, pp. 73-78
121. Shatil, G., Saimoto, A., Ren, X.J., 2008, "Ductile-Brittle Fatigue and Fracture Behaviour of Aluminium/PMMA Bimaterial 3PB Specimens", Engineering Fracture Mechanics, **75**, pp. 674-681

Other Experimental Methods:

122. Faust, R.C., 1955, "Refractive Index Determinations by the Central Illumination (Becke Line) Method", Proceedings of the Physical Society, **12**, (B), pp. 1081-1094
123. Chen, T.Y., 1995, "Digital Fringe Multiplication in Three-Dimensional Photoelasticity", Journal of Strain Analysis, **30**, (1), pp. 1-7
124. Ramesh, K., Deshmukh, S.S., 1996, "Three-Fringe Photoelasticity – Use of Colour Image Processing Hardware to Automate Ordering of Isochromatics", Strain, **32**, (3), pp. 79-86
125. Ravichandran, M., Ramesh, K., 2005, "Evaluation of Stress Field Parameters for an Interface Crack in a Bimaterial by Digital Photoelasticity", Journal of Strain Analysis for Engineering Design, **40**, (4), pp. 327-343
126. Madhu, K.R., Ramesh, K., 2007, "Noise Removal in Three-Fringe Photoelasticity by Adaptive Colour Difference Estimation", Optics and Lasers in Engineering, **45**, pp. 175-182

APPENDIX A

Maple Code for Overdeterministic Analysis and Fringe Regeneration, Single Analysis Run

This Maple 11 worksheet is a single-analysis implementation of

- Lee's equations
- Sampson's stress-optic law
- Overdeterministic analysis
- Image regeneration

The worksheet allows the user to specify the x- and y-offsets.
The output of this worksheet are

- A text file containing the Mode-I and Mode-II stress intensity factors calculated, and the energy release rate calculated
- A text file containing the fringe orders generated for each point in the grid overlaying the region surrounding the crack tip
- An image file, containing the regenerated fringe pattern yielded by the analysis

The equations themselves and their associated variables have already been discussed in the relevant section of the dissertation.
That also applies to the implementation of the overdeterministic analysis
Finally, specifics pertaining to use of Maple and its commands must be looked up in the Maple manual
and the Maple Help.

The worksheet begins here

```
> restart;
> Digits := 30;
```

Digits determines the floating-point precision to be used
If *Digits* is set to less than 30 the worksheet tends to crash with no explanation and no error messages

Load two packages necessary for the analysis

```
> with(VectorCalculus):
> with(LinearAlgebra):
```

Give the specimen name

```
> SpecName := w30 aw033 090 090ALPH15;
```

#Note: a) Always start specimen and file names with a letter
b) Specimen and file names must be in one word. Underscores did not show up here, but are there.

Enter which quadrant you area analyzing

```
> Quadrant := 1;
> #Enter stress-optic response (Do not change these regardless of fiber orientation)
> f1 := 55872;
> f2 := 55872;
> f12 := 32255;
> #Enter fiber angle
```

Fiber angle α is specified with respect to the interface. Keep this in mind when working with angled interfaces.

> $\alpha := \frac{15 \cdot \pi}{180};$

Enter the value for *ScaleFactor*

> *ScaleFactor* := **60;**

ScaleFactor determines size of regeneration grid. A value of 40 corresponds to having used an annular region with OD = 4t, while 60 yields OD = 3t and 80 yields OD = 2t

Enter the desired x- and y offsets.

> *xOffset* := 6;

> *yOffset* := 4;

The physical size these offsets represent vary with *ScaleFactor*, but are much less than 1 mm.

> *#Enter number of datapoints taken*

> *numdata* := 42;

Specify how many iterations to perform for finding the stress intensity factors.
From experience, if the solution does converge, it does so well before 20 iterations
Thus, 20 iterations work well without spending excessive computation time

> *numit* := 20;

> *#Set the size of matrix that is displayed fully (and not just as a placeholder)*

> *interface*(*rtablesize* = 200);

> *#Enter experimental data, in cartesian coordinates, in meters relative to crack tip, in order (x,y,N)*

The experimental data can be pasted directly into the matrix placeholder (the "[ ]"), e.g. from Excel.

>

$$InitialDataCartesian := Matrix\begin{pmatrix}
-0.002498361 & 0.002498361 & 0.5 \\
-0.006662295 & 0.006245902 & 0.5 \\
-0.004580328 & 0.004163934 & 0.5 \\
-0.003331148 & 0.002914754 & 0.5 \\
-0.005829508 & 0.005413115 & 0.5 \\
-0.006245902 & 0.005829508 & 0.5 \\
-0.003747541 & 0.003331148 & 0.5 \\
-0.002914754 & 0.002914754 & 0.5 \\
-0.004163934 & 0.003747541 & 0.5 \\
-0.004996721 & 0.004580328 & 0.5 \\
-0.005413115 & 0.004996721 & 0.5 \\
0.000416393 & 0.004163934 & 1.5 \\
0.001665574 & 0.003331148 & 1.5 \\
0.00124918 & 0.003747541 & 1.5 \\
0.000832787 & 0.004163934 & 1.5 \\
0.003331148 & 0.001665574 & 1 \\
0.006245902 & 0.006662295 & 1 \\
0.004996721 & 0.003747541 & 1 \\
0.003747541 & 0.002081967 & 1 \\
0.004163934 & 0.002498361 & 1 \\
0.004580328 & 0.002914754 & 1 \\
0.006245902 & 0.006245902 & 1 \\
0.006245902 & 0.005829508 & 1 \\
0.005829508 & 0.005413115 & 1 \\
0.005829508 & 0.004996721 & 1 \\
0.005413115 & 0.004580328 & 1 \\
0.005413115 & 0.004163934 & 1 \\
0.005413115 & 0.003331148 & 1 \\
-0.00124918 & 0.008744262 & 1 \\
-0.00124918 & 0.003331148 & 1 \\
-0.001665574 & 0.006662295 & 1 \\
-0.001665574 & 0.007911475 & 1 \\
-0.00124918 & 0.008327869 & 1 \\
-0.00124918 & 0.003747541 & 1 \\
-0.001665574 & 0.005413115 & 1 \\
-0.001665574 & 0.007078689 & 1 \\
-0.001665574 & 0.007495082 & 1 \\
-0.00124918 & 0.004163934 & 1 \\
-0.001665574 & 0.004580328 & 1 \\
-0.001665574 & 0.004996721 & 1 \\
-0.001665574 & 0.005829508 & 1 \\
-0.001665574 & 0.006245902 & 1
\end{pmatrix}$$

```
> DataCartesian := Matrix(numdata, 3):
> data := Matrix(numdata, 3):
> printlevel := 0;
```

The following **for** loop adds the desired x- and y offset to the dataset. An additional tiny offset is added so that one does not inadvertently step into singularities, that is, where x or y equal zero.
OffsetCount is just a counter

```
> for OffsetCount from 1 to numdata do
    DataCartesian[OffsetCount, 1] := InitialDataCartesian[OffsetCount, 1] + ((xOffset + 0.1)·2)/10000;
#Add x-offset in steps of 0.0002, that is, 0.2 mm. The factor of 0.1 is to avoid singularities
    DataCartesian[OffsetCount, 2] := InitialDataCartesian[OffsetCount, 2] + ((yOffset + 0.1)·2)/10000 #Ditto for y-offset
    DataCartesian[OffsetCount, 3] := InitialDataCartesian[OffsetCount, 3]; #The N-values do not change
    end do:
```

The following **for** loop converts the Cartesian coordinates to polar coordinates, while leaving *N* unchanged.
CartCount is just a counter
data is the matrix containing the data points in polar coordinates, along with the fringe orders at each data point, that is, each data point is now (r, θ, N), still relative to the crack tip.

```
#Convert data from cartesian to polar coordinates
  for CartCount from 1 to numdata do
   data[CartCount, 1] := sqrt((DataCartesian[CartCount, 1])^2 + (DataCartesian[CartCount, 2])^2);
   data[CartCount, 2] := arctan(DataCartesian[CartCount, 2]/DataCartesian[CartCount, 1]);
   data[CartCount, 3] := DataCartesian[CartCount, 3];
  end do:
```

```
> #Declare the stress field, start by creating an odd counter (we are using an odd power series)
```

```
> n := 2·count − 1;
> COUNT := 1;
> n2 := 2·COUNTB − 1;
> COUNTB := 1;
```

> #Sigma x

>

$$\sigma_{xSUM} := \sum_{count=1}^{COUNT} K0[n] \cdot \left((Mb - p^2) \left(e^{B(\pi - thetaL)} A2bar \cos\left(e \ln(rL) + \frac{1 (n-2) thetaL}{2} \right) + e^{-B(\pi - thetaL)} A2 \cos\left(e \ln(rL) - \frac{1 (n-2) thetaL}{2} \right) \right) rL^{\frac{(n-2)}{2}} - (Mb - q^2) \left(e^{B(\pi - thetaS)} B2bar \cos\left(e \ln(rS) + \frac{1 (n-2) thetaS}{2} \right) + e^{-B(\pi - thetaS)} B2 \cos\left(e \ln(rS) - \frac{1 (n-2) thetaS}{2} \right) \right) rS^{\frac{(n-2)}{2}} \right) \Gamma\left(2 \sqrt{2\pi}\ D2 \cosh(e\pi)\right) + \sum_{count=1}^{COUNTB} Kstar[n] \cdot \left(-(Mb - p^2) \left(e^{B(\pi - thetaL)} A2bar \sin\left(e \ln(rL) + \frac{1 (n-2) thetaL}{2} \right) + e^{-B(\pi - thetaL)} A2 \sin\left(e \ln(rL) - \frac{1 (n-2) thetaL}{2} \right) \right) rL^{\frac{(n-2)}{2}} + (Mb - q^2) \left(e^{B(\pi - thetaS)} B2bar \sin\left(e \ln(rS) + \frac{1 (n-2) thetaS}{2} \right) + e^{-B(\pi - thetaS)} B2 \sin\left(e \ln(rS) - \frac{1 (n-2) thetaS}{2} \right) \right) rS^{\left(\left(\frac{n-2}{2}\right)\right)} \right) \Gamma\left(2 \sqrt{2\pi}\ D2 \cosh(e\pi)\right);$$

> #Sigma y

>

$$\sigma_{ySUM} := \sum_{count=1}^{COUNT} K0[n] \cdot \left((1 + Ma) \left(e^{B(\pi - thetaL)} A2bar \cos\left(e \ln(rL) + \frac{1 (n-2) thetaL}{2} \right) + e^{-B(\pi - thetaL)} A2 \cos\left(e \ln(rL) - \frac{1 (n-2) thetaL}{2} \right) \right) rL^{\frac{(n-2)}{2}} - (1 + Ma) \left(e^{B(\pi - thetaS)} B2bar \cos\left(e \ln(rS) + \frac{1 (n-2) thetaS}{2} \right) + e^{-B(\pi - thetaS)} B2 \cos\left(e \ln(rS) - \frac{1 (n-2) thetaS}{2} \right) \right) rS^{\frac{(n-2)}{2}} \right) \Gamma\left(2 \sqrt{2\pi}\ D2 \cosh(e\pi)\right) + \sum_{count=1}^{COUNTB} Kstar[n] \cdot \left(-(1 + Ma) \left(e^{B(\pi - thetaL)} A2bar \sin\left(e \ln(rL) + \frac{1 (n-2) thetaL}{2} \right) + e^{-B(\pi - thetaL)} A2 \sin\left(e \ln(rL) - \frac{1 (n-2) thetaL}{2} \right) \right) rL^{\frac{(n-2)}{2}} + (1 + Ma) \left(e^{B(\pi - thetaS)} B2bar \sin\left(e \ln(rS) + \frac{1 (n-2) thetaS}{2} \right) + e^{-B(\pi - thetaS)} B2 \sin\left(e \ln(rS) - \frac{1 (n-2) thetaS}{2} \right) \right) rS^{\frac{(n-2)}{2}} \right) \Gamma\left(2 \sqrt{2\pi}\ D2 \cosh(e\pi)\right);$$

> #Tau xy

>

$$\tau_{xySIM} := \sum_{count=1}^{COUNT} K0[n] \cdot \left(alphaL \left(e^{e(\pi - thetaL)} A2bar \sin\left(e \ln(rL) + \frac{1\ (n-2)\ thetaL}{2} \right) - e^{-e(\pi - thetaL)} A2 \sin\left(e \ln(rL) - \frac{1\ (n-2)\ thetaL}{2} \right) \right) rL^{\frac{(n-2)}{2}} + alphaS \left(-e^{e(\pi - thetaS)} B2bar \sin\left(e \ln(rS) + \frac{1\ (n-2)\ thetaS}{2} \right) + e^{-e(\pi - thetaS)} B2 \sin\left(e \ln(rS) - \frac{1\ (n-2)\ thetaS}{2} \right) \right) rS^{\frac{(n-2)}{2}} \right) \Gamma\left(2\sqrt{2\pi}\ D2 \cosh(e\pi) \right) + \sum_{count=1}^{COUNTB} Kstar[n] \cdot \left(alphaL \left(e^{e(\pi - thetaL)} A2bar \cos\left(e \ln(rL) + \frac{1\ (n-2)\ thetaL}{2} \right) - e^{-e(\pi - thetaL)} A2 \cos\left(e \ln(rL) - \frac{1\ (n-2)\ thetaL}{2} \right) \right) rL^{\frac{(n-2)}{2}} + alphaS \left(-e^{e(\pi - thetaS)} B2bar \cos\left(e \ln(rS) + \frac{1\ (n-2)\ thetaS}{2} \right) + e^{-e(\pi - thetaS)} B2 \cos\left(e \ln(rS) - \frac{1\ (n-2)\ thetaS}{2} \right) \right) rS^{\frac{(n-2)}{2}} \right) \Gamma\left(2\sqrt{2\pi}\ D2 \cosh(e\pi) \right);$$

> #Declare and specify a lot of variables

> $A2 := alphaS + (1 + Ma)\,\eta;$

$A2bar := alphaS - (1 + Ma)\,\eta;$

$B2 := alphaL + (1 + Ma)\,\eta;$

$B2bar := alphaL - (1 + Ma)\,\eta;$

$$e := \frac{1 \ln\left(\frac{1-\beta}{1+\beta} \right)}{2\pi};$$

$$\beta := \frac{h11}{\sqrt{h12\ h21}};$$

$h11 := l11_1 - l11_2;$

$h12 := l12_1 + l12_2;$

$h21 := l21_1 + l21_2;$

$thetaL := \arctan(p \tan(\theta));$

$thetaS := \arctan(q \tan(\theta));$

$$\eta := \sqrt{\frac{h21}{h12}};$$

$$rL := r\sqrt{\cos(\theta)^2 + p^2 \sin(\theta)^2};$$

$$rS := r\sqrt{\cos(\theta)^2 + q^2\sin(\theta)^2};$$

$$p := \sqrt{B12 - \sqrt{B12^2 - K66}};$$
$$q := \sqrt{B12 + \sqrt{B12^2 - K66}};$$

$$B12 := \frac{1\left(2\,a12 + a66 + \rho\,c^2\left(a12^2 - a11\,a66 - a11\,a22\right)\right)}{2\,a11};$$
$$K66 := \frac{a22 + \rho\,c^2\left(a12^2 - a22\,a66 - a11\,a22 + \rho\,c^2\,a66\left(a11\,a22 - a12^2\right)\right)}{a11};$$

$$alphaL := p + \frac{a22\,\rho\,c^2}{p} - p\,\rho\,c^2\,a11 - \frac{\rho^2\,c^4\left(a11\,a22 - a12^2\right)}{p};$$
$$alphaS := q + \frac{a22\,\rho\,c^2}{q} - q\,\rho\,c^2\,a11 - \frac{\rho^2\,c^4\left(a11\,a22 - a12^2\right)}{q};$$

$$Ma := \rho\,c^2\,(a12 - a11);$$
$$Mb := \rho\,c^2\,(a12 - a22);$$

$$l11_1 := \frac{qS - qL}{alphaS - alphaL};$$
$$l12_1 := \frac{(1 + Ma)\,(pL - pS)}{D2};$$
$$l21_1 := \frac{alphaS\,qL - alphaL\,qS}{D2};$$
$$l11_2 := \frac{qS - qL}{alphaS - alphaL};$$
$$l21_2 := \frac{alphaS\,qL - alphaL\,qS}{D2};$$
$$l12_2 := \frac{(1 + Ma)\,(pL - pS)}{D2};$$

$$qS := \frac{a12\left(Mb - q^2\right) + a22\,(1 + Ma)}{q};$$
$$qL := \frac{a12\left(Mb - p^2\right) + a22\,(1 + Ma)}{p};$$

$$pS := a11\left(Mb - q^2\right) + a12\,(1 + Ma);$$
$$pL := a11\left(Mb - p^2\right) + a12\,(1 + Ma);$$

$$D2 := (1 + Ma)\,(alphaS - alphaL);$$

$$a11 := \frac{\cos(\alpha)^4}{EL} + \frac{\sin(\alpha)^4}{ET};$$
$$a12 := -\frac{nuLT}{EL};$$
$$a66 := \frac{1}{\mu LT};$$
$$a22 := \frac{\cos(\alpha)^4}{ET} + \frac{\sin(\alpha)^4}{EL};$$

$\rho := 1100;$

$cL := 700;$
$cS := 300;$
$c := 20;$

$\rho 2 := 1001;$
$\rho 1 := 1001;$

$nuLT := 0.49;$
$\nu := 0.26;$

$\mu LT := 2.10000000\ 10^9;$
$\mu 2 := 2.100000000\ 10^9;$
$\mu := 2.100000000\ 10^9;$

$EL := 9.652613305\ 10^9;$
$ET := 9.652613305\ 10^9;$

$h := d;$
$d := 0.006350;$

Here we begin the procedure for applying the overdeterministic analysis
Start by expressing Sampson's stress-optic law as an error function *g*

> $$g := evalf\left(\left(\frac{\sigma_{ySIM}}{f1} - \frac{\sigma_{xSIM}}{f2}\right)^2 + \left(\frac{2\,\tau_{xySIM}}{f12}\right)^2 - \frac{NT^2}{h^2}\right):$$

Take partial derivatives of the error function with respect to the coefficients that we are seeking:

> $parK01 := diff(g, K0[1]);$
> $parKstar1 := diff(g, Kstar[1]);$

Make Maple functions from the error function and the partial derivatives, using **unapply**

```
> gFunc := unapply(evalf(g), K0[1], Kstar[1], r, theta, NT);
> mk01 := unapply((parK01), K0[1], Kstar[1], r, theta);
> mkstar1 := unapply((parKstar1), K0[1], Kstar[1], r, theta);
```

Define the matrices used in the least-squares approach
As yet, they are just "empty" matrices with the number of rows and columns given

```
> C := Matrix(numdata, 2);
> gmat := Matrix(numdata, 1);
> coef := Matrix(numit + 1, 3);
> DIFFERENCE := Matrix(3, 1);
> difference := Matrix(numit, 3);

> #State initial guesses for the coefficients
> coef[1, 2] := 1e6; coef[1, 3] := 1e5;
```

Perform the least squares method:

```
>
 for i from 1 to numit do
difference_{i,1} := 1;
coef_{i,1} := 1;
for j to numdata do
gmat_{j,1} := evalf(-gFunc(coef_{i,2}, coef_{i,3}, data_{j,1}, data_{j,2}, data_{j,3}));
C_{j,1} := evalf(mk01(coef_{i,2}, coef_{i,3}, data_{j,1}, data_{j,2}));
C_{j,2} := evalf(mkstar1(coef_{i,2}, coef_{i,3}, data_{j,1}, data_{j,2}));

        end do:
ctran := evalf(Transpose(C));
dee := evalf(MatrixMatrixMultiply(ctran, C));
deeInv := evalf(MatrixInverse(dee));
deeInvC := evalf(MatrixMatrixMultiply(deeInv, ctran));
DIFFERENCE := evalf(MatrixMatrixMultiply(deeInvC, gmat));
for k from 2 to 3 do
difference_{i,k} := DIFFERENCE_{k-1,1};
coef_{i+1,k} := evalf(coef_{i,k} + DIFFERENCE_{k-1,1})
end do:
end do:
```

The *coef* matrix contains the coefficients we were seeking
The last row contains the values calculated in the last iteration
Now tell Maple which matrix element corresponds to which coefficient

```
> K0_1 := coef[21, 2]; Kstar_1 := coef[21, 3];
```

Show the coefficient matrix

> print(coef);

Perform a simple convergence check
There is a fixed number of iterations.
The check is simply to see if the solution converged.
Convergence can be visually checked (by looking at the *coef* matrix) for the single-pass worksheet,
These values (*true* or false) are stored in a file in the multi-pass worksheet

> **if** $\left(0.97 \le \frac{coef[21,2]}{coef[20,2]} < 1.03\right)$ **then** *Converg* := *True* **else** *Converg* := *False* **end if**;

> $EnergyReleaseRate := evalf\left(\frac{\left((K0_1)^2 + (Kstar_1)^2\right)\cdot h21}{(4\cdot\cosh(epsilon\cdot\pi))^2}\right)$;

> #Now generate image matrix

First define the stress-optic law

> $Nplot := \sqrt{evalf\left(\left(\left(\frac{\sigma_{ySIM}}{f1} - \frac{\sigma_{xSIM}}{f2}\right)^2 + \left(\frac{2\,\tau_{xySIM}}{f12}\right)^2\right)\cdot h^2\right)}$:

Make the stress-optic law into a function of *r* and *theta*
> Nplo2 := unapply(evalf(Nplot), r, theta);

Specify the image parameters (width and height)
WidthParam and *HeightParam* are variables used to simplify code later
> picwidth := 300;
> $WidthParam := \frac{picwidth}{2}$;

> picheight := 300;
> $HeightParam := \frac{picheight}{2}$;

Setting *Digits* to 20 cuts down on the image generation time, while not reducing accuracy.
The *MathCad* comment applies if one desires to import matrices into MathCad 2000.
That is no longer done for these purposes

> Digits := 20#MathCad is only able to import matrix files with digits = 10
> replo := Matrix(picheight, picwidth) :

For each point in the image matrix, calculate the fringe order (*N*-value)
> **for** *aa* **from** 1 **to** *picheight* **do**
for *bb* **from** 1 **to** *picwidth* **do**

$wpar := \frac{(bb - WidthParam)}{ScaleFactor\cdot picwidth}$;
$hpar := \frac{(HeightParam - aa)}{ScaleFactor\cdot picheight}$;

```
if wpar ≠ 0 then
if hpar ≠ 0 then

r := sqrt(wpar^2 + hpar^2);
theta := arctan(hpar/wpar);
replo[bb, aa] := evalf(Nplo2(r, theta)); #This is where the N-value is calculated

else
replo[aa, bb] := 0; # If a singularity occurs then simply set the N-value to zero.
end if
end if
od:
od:
```

The following segments of code create several output files.
There is one important issue to know about Maple and output files:
First a *variable* containing the variables going into the file name must be declared (e.g. "ResultsNum").
Then the file creation function is invoked using that *variable* where the file name goes.

The output files have names containing some variables:
The specimen name, the x-offset, the y-offset, and the quadrant number.
That way, for each offset a new, uniquely named set of files are created.
The files pertaining to a particular specimen, specimen quadrant, and offset are thus easily found later.

The following segment creates a text-format file whose NAME contains "2TRESULT", the x-offset, y-offset, specimen name, and quadrant number. "2TRESULT" denotes the results from a 2-term solution.
The FILE CONTENTS are the values for the x-offset, y-offset, K_1^0, K_1^*, and energy release rate. These values are preceded by "xOffset=", "yOffset=", "K01=", "Kstar1=", and "EnergyReleaseRate=", respectively.
Always remember *fclose* when using *fopen* to create a file. *fopen* closes the file properly. Otherwise the output file will be corrupted and unreadable.

```
>
ResultsNum := nprintf("2TRESULT xoffset=%g yoffset=%g spec=%a Quad%g", xOffset, yOffset, SpecName,
Quadrant);
stuff := fopen(ResultsNum, WRITE);
fprintf(stuff, "xOffset=%g yOffset=%g K01=%e Kstar1=%e EnergyReleaseRate=%g", xOffset, yOffset, K0_1, Kstar_1,
EnergyReleaseRate);
fclose(stuff);
```

The following segment creates a text-format file whose NAME contains "2TNMATRIX", the x-offset, the y-offset, the specimen name, and the quadrant number.
The word "2TNMATRIX" indicates that this is the *N*-value matrix generated with a 2-term solution.
The FILE CONTENTS are the *N*-values for each point in the grid
The FILE FORMAT is a comma-delimited text file
The function *ExportMatrix* exports the numerical data in text format, the elements arranged properly like in the matrix, and here the delimiter is specified to be a comma.
fclose is not necessary when using *ExportMatrix*

>

```
ResultMatr := nprintf("2TNMATRIX xoffset=%g yoffset=%g spec=%a quad%a", xOffset, yOffset, SpecName,
Quadrant);
ExportMatrix(ResultMatr, replo, target = delimited, delimiter = ",");
```

> #Image generation procedure

The following segment creates a FILE NAME that contains “2TIMAGE”, the x-offset, the y-offset, the specimen name, and the quadrant number.
“2TIMAGE” indicates that this is the image file generated with the 2-term solution

>

```
ResultPicName := sprintf("2TIMAGE xoffset=%g yoffset=%g spec=%a Quad%g .bmp", xOffset, yOffset,
SpecName, Quadrant);
```

The *N*-matrix has been generated.
Now a two-step process will generate a bitmap image from the *N*-matrix

```
> WordMatrix := Matrix(picheight, picwidth):
> BitMatrix := Matrix(picheight, picwidth):
```

This is the first step :
The following worksheet segment looks at each *N*-value in the *N*-matrix
The function *frac* looks only at the numbers behind the decimal point
Whether an *N*-value is 1.3, 2.3, or 3.3 is not important in this context, the .3 part is what is important, as this indicates which *order-type* the fringe is, that is, if it is whole-order, half-order, or something in between.
For each order-type a corresponding grayscale value is assigned, as a word

```
> for qq from 1 to picheight do
  for rr from 1 to picwidth do
if (9/10) < frac(replo[rr, qq]) ≤ 1 then WordMatrix[rr, qq] := BLK
  elif (8/10) < frac(replo[rr, qq]) ≤ (9/10) then WordMatrix[rr, qq] := DKGY
  elif (7/10) < frac(replo[rr, qq]) ≤ (8/10) then WordMatrix[rr, qq] := MDGY
  elif (6/10) < frac(replo[rr, qq]) ≤ (7/10) then WordMatrix[rr, qq] := LTGY
  elif (4/10) < frac(replo[rr, qq]) ≤ (6/10) then WordMatrix[rr, qq] := WHT
  elif (3/10) < frac(replo[rr, qq]) ≤ (4/10) then WordMatrix[rr, qq] := LTGY
  elif (2/10) < frac(replo[rr, qq]) ≤ (3/10) then WordMatrix[rr, qq] := MDGY
  elif (1/10) < frac(replo[rr, qq]) ≤ (2/10) then WordMatrix[rr, qq] := DKGY
  elif (0) < frac(replo[rr, qq]) ≤ (1/10) then WordMatrix[rr, qq] := BLK

  end if;

  end do:
 end do:
```

We now have a “word matrix”
The meanings of the words are
BLK = black (whole order)
DKGY = dark gray (intermediate order)
MDGY = medium gray (intermediate order)
LTGY = light gray (intermediate order)
WHT = white (half order)

Each point in the grid overlaying the region surrounding the crack tip now has a word associated with it.
That words is the name of the grayscale at that point
The following segment converts these words into numerical grayscale values
We then get a bit matrix where each element has a grayscale value

```
>
#The preceding ascribes a word value to each point, depending on whether the N-value is whole, half, or something in
between.
#The following converts those words to grayscales

> for qqqq from 1 to picheight do
for rrrr from 1 to picwidth do

if WordMatrix[rrrr, qqqq] = BLK then BitMatrix[rrrr, qqqq] := 0
elif WordMatrix[rrrr, qqqq] = DKGY then BitMatrix[rrrr, qqqq] := 64/255
elif WordMatrix[rrrr, qqqq] = MDGY then BitMatrix[rrrr, qqqq] := 127/255
elif WordMatrix[rrrr, qqqq] = LTGY then BitMatrix[rrrr, qqqq] := 191/255
elif WordMatrix[rrrr, qqqq] = WHT then BitMatrix[rrrr, qqqq] := 255/255
end if

end do;
end do;
```

The following code generates a bitmap file from the bit matrix
The file name was specified earlier in the worksheet

```
> #Write image to file

> ResultBitmap := ImageTools[Create](picheight, picwidth, BitMatrix):
> ImageTools[Write](ResultPicName, ResultBitmap, format = BMP);
```

End of the worksheet

APPENDIX B

Maple Code for Overdeterministic Analysis and Fringe Regeneration, Multiple Analysis Run (Stepping Through Grid Surrounding Crack Tip)

The main difference between this worksheet and the Single-Pass worksheet is
that this worksheet steps through a user-specified range of offsets and generates many images, one for
each offset.

Each image generated is also lower resolution (to save calculation time)
Once the proper offset has been located, use the single-pass worksheet to generate a larger image

For each offset the following are calculated:

- Mode-I and Mode-II stress intensity factors
- Convergence of the stress intensity factors is checked (*true* or *false*)
- Energy release rate
- Fringe order at each point in the grid overlaying the region surrounding the crack tip

#Also for each offset several files are generated
Each file has a name containing the offset in question, the specimen name, and the quadrant number
The files generated are:

- An image file containing the regenerated fringe pattern for the offset in question
- A text file containing the x- and y-offset, Mode-I and Mode-II stress intensity factors, the energy release rate, and the result of the convergence check
- A text file containing the fringe orders at each point in the grid overlaying the region surrounding the crack tip

In addition, a text file is generated that contains a running tab of the x- and y-offset, Mode-I and Mode-II stress intensity factors, the energy release rate, and the result of the convergence check

#This worksheet will be commented only where it differs from the Single-Pass worksheet

```
> restart;
> Digits := 30;
> with(VectorCalculus):
> with(LinearAlgebra):
> SpecName := w30 aw033 090 090ALPH15;
> Quadrant := 1;
> ScaleFactor := 60;
> #Enter stress-optic response (Do not change these, regardless of fiber orientation)
> f1 := 55872;
> f2 := 55872;
> f12 := 32255;
> #Enter fiber angle
> alpha := 15*Pi/180;
> #Enter number of datapoints taken
> numdata := 42;
```

```
> numit := 20;
> #Set the size of matrix that is displayed fully (and not just as a placeholder)
> interface(rtablesize = 200);
> #Enter experimental data, in cartesian coordinates, in meters relative to crack tip, in order (x,y,N)
>
```

$$InitialDataCartesian := Matrix$$

-0.002498361	0.002498361	0.5
-0.006662295	0.006245902	0.5
-0.004580328	0.004163934	0.5
-0.003331148	0.002914754	0.5
-0.005829508	0.005413115	0.5
-0.006245902	0.005829508	0.5
-0.003747541	0.003331148	0.5
-0.002914754	0.002914754	0.5
-0.004163934	0.003747541	0.5
-0.004996721	0.004580328	0.5
-0.005413115	0.004996721	0.5
0.000416393	0.004163934	1.5
0.001665574	0.003331148	1.5
0.00124918	0.003747541	1.5
0.000832787	0.004163934	1.5
0.003331148	0.001665574	1
0.006245902	0.006662295	1
0.004996721	0.003747541	1
0.003747541	0.002081967	1
0.004163934	0.002498361	1
0.004580328	0.002914754	1
0.006245902	0.006245902	1
0.006245902	0.005829508	1
0.005829508	0.005413115	1
0.005829508	0.004996721	1
0.005413115	0.004580328	1
0.005413115	0.004163934	1
0.005413115	0.003331148	1
-0.00124918	0.008744262	1
-0.00124918	0.003331148	1
-0.001665574	0.006662295	1
-0.001665574	0.007911475	1
-0.00124918	0.008327869	1
-0.00124918	0.003747541	1
-0.001665574	0.005413115	1
-0.001665574	0.007078689	1
-0.001665574	0.007495082	1
-0.00124918	0.004163934	1
-0.001665574	0.004580328	1
-0.001665574	0.004996721	1
-0.001665574	0.005829508	1
-0.001665574	0.006245902	1

> $DataCartesian := Matrix(numdata, 3):$

> $data := Matrix(numdata, 3):$

> $printlevel := 0;$

> *#Now start the loop that will step through several offsets and generate one image matrix per offset*

This begins the loop that will step through the range of offsets that the user selects
The user can select the size of each step (using **by**)
The range is specified with **from** and **to**

> **for** *xOffset* **from** -6 **by** 0.5 **to** 6 **do**

for *yOffset* **from** -6 **by** 0.5 **to** 6 **do**

for *OffsetCount* **from** 1 **to** *numdata* **do**

$$DataCartesian_{OffsetCount,1} := InitialDataCartesian_{OffsetCount,1} + \left(\frac{(xOffset + 0.1)\cdot 2}{10000}\right);$$

#Add x-offset in steps of 0.0002, that is, 0.2 mm. The factor of 0.1 is to avoid singularities

$$DataCartesian_{OffsetCount,2} := InitialDataCartesian_{OffsetCount,2} + \left(\frac{(yOffset + 0.1)\cdot 2}{10000}\right) \#Ditto\ for\ y\text{-}offset$$

$$DataCartesian_{OffsetCount,3} := InitialDataCartesian_{OffsetCount,3}; \#The\ N\text{-}values\ do\ not\ change$$

end do;

for *CartCount* **from** 1 **to** *numdata* **do**

$$data_{CartCount,1} := \mathrm{sqrt}\left(\left(DataCartesian_{CartCount,1}\right)^2 + \left(DataCartesian_{CartCount,2}\right)^2\right);$$

$$data_{CartCount,2} := \arctan\left(\frac{DataCartesian_{CartCount,2}}{DataCartesian_{CartCount,1}}\right);$$

$$data_{CartCount,3} := DataCartesian_{CartCount,3};$$

end do;

#Declare the stress field, start by creating an odd counter (we are using an odd power series)

$n := 2\cdot count - 1;$

$COUNT := 1;$

$n2 := 2\cdot COUNTB - 1;$

$COUNTB := 1;$

#Sigma x

$$\sigma_{xSIM} := \sum_{count=1}^{COUNT} K0[n] \cdot \left((Mb - p^2) \left(e^{B(\pi - thetaL)} A2bar \cos\left(e \ln(rL) + \frac{1 (n-2) thetaL}{2} \right) + e^{-B(\pi - thetaL)} A2 \cos\left(e \ln(rL) - \frac{1 (n-2) thetaL}{2} \right) \right) rL^{\frac{(n-2)}{2}} - (Mb - q^2) \left(e^{B(\pi - thetaS)} B2bar \cos\left(e \ln(rS) + \frac{1 (n-2) thetaS}{2} \right) + e^{-B(\pi - thetaS)} B2 \cos\left(e \ln(rS) - \frac{1 (n-2) thetaS}{2} \right) \right) rS^{\frac{(n-2)}{2}} \right) \Gamma\left(2 \sqrt{2\pi} D2 \cosh(e\pi) \right) + \sum_{count=1}^{COUNTB} Kstar[n] \cdot \left(-(Mb - p^2) \left(e^{B(\pi - thetaL)} A2bar \sin\left(e \ln(rL) + \frac{1 (n-2) thetaL}{2} \right) + e^{-B(\pi - thetaL)} A2 \sin\left(e \ln(rL) - \frac{1 (n-2) thetaL}{2} \right) \right) rL^{\frac{(n-2)}{2}} + (Mb - q^2) \left(e^{B(\pi - thetaS)} B2bar \sin\left(e \ln(rS) + \frac{1 (n-2) thetaS}{2} \right) + e^{-B(\pi - thetaS)} B2 \sin\left(e \ln(rS) - \frac{1 (n-2) thetaS}{2} \right) \right) rS^{\left(\left[\frac{n-2}{2} \right] \right)} \right) \Gamma\left(2 \sqrt{2\pi} D2 \cosh(e\pi) \right);$$

#Sigma y

$$\sigma_{ySIM} := \sum_{count=1}^{COUNT} K0[n] \cdot \left((1 + Ma) \left(e^{B(\pi - thetaL)} A2bar \cos\left(e \ln(rL) + \frac{1 (n-2) thetaL}{2} \right) + e^{-B(\pi - thetaL)} A2 \cos\left(e \ln(rL) - \frac{1 (n-2) thetaL}{2} \right) \right) rL^{\frac{(n-2)}{2}} - (1 + Ma) \left(e^{B(\pi - thetaS)} B2bar \cos\left(e \ln(rS) + \frac{1 (n-2) thetaS}{2} \right) + e^{-B(\pi - thetaS)} B2 \cos\left(e \ln(rS) - \frac{1 (n-2) thetaS}{2} \right) \right) rS^{\frac{(n-2)}{2}} \right) \Gamma\left(2 \sqrt{2\pi} D2 \cosh(e\pi) \right) + \sum_{count=1}^{COUNTB} Kstar[n] \cdot \left(-(1 + Ma) \left(e^{B(\pi - thetaL)} A2bar \sin\left(e \ln(rL) + \frac{1 (n-2) thetaL}{2} \right) + e^{-B(\pi - thetaL)} A2 \sin\left(e \ln(rL) - \frac{1 (n-2) thetaL}{2} \right) \right) rL^{\frac{(n-2)}{2}} + (1 + Ma) \left(e^{B(\pi - thetaS)} B2bar \sin\left(e \ln(rS) + \frac{1 (n-2) thetaS}{2} \right) + e^{-B(\pi - thetaS)} B2 \sin\left(e \ln(rS) - \frac{1 (n-2) thetaS}{2} \right) \right) rS^{\frac{(n-2)}{2}} \right) \Gamma\left(2 \sqrt{2\pi} D2 \cosh(e\pi) \right);$$

#Tau xy

$$\tau_{xySIM} := \sum_{count=1}^{COUNT} K0[n] \cdot \left(alphaL \left(e^{e(\pi - thetaL)} A2bar \sin\left(e \ln(rL) + \frac{1\ (n-2)\ thetaL}{2} \right) - e^{-e(\pi - thetaL)} A2 \sin\left(e \ln(rL) - \frac{1\ (n-2)\ thetaL}{2} \right) \right) rL^{\frac{(n-2)}{2}} + alphaS \left(-e^{e(\pi - thetaS)} B2bar \sin\left(e \ln(rS) + \frac{1\ (n-2)\ thetaS}{2} \right) + e^{-e(\pi - thetaS)} B2 \sin\left(e \ln(rS) - \frac{1\ (n-2)\ thetaS}{2} \right) \right) rS^{\frac{(n-2)}{2}} \right) \Gamma\left(2\sqrt{2\pi}\ D2 \cosh(e\pi) \right) + \sum_{count=1}^{COUNTB} Kstar[n] \cdot \left(alphaL \left(e^{e(\pi - thetaL)} A2bar \cos\left(e \ln(rL) + \frac{1\ (n-2)\ thetaL}{2} \right) - e^{-e(\pi - thetaL)} A2 \cos\left(e \ln(rL) - \frac{1\ (n-2)\ thetaL}{2} \right) \right) rL^{\frac{(n-2)}{2}} + alphaS \left(-e^{e(\pi - thetaS)} B2bar \cos\left(e \ln(rS) + \frac{1\ (n-2)\ thetaS}{2} \right) + e^{-e(\pi - thetaS)} B2 \cos\left(e \ln(rS) - \frac{1\ (n-2)\ thetaS}{2} \right) \right) rS^{\frac{(n-2)}{2}} \right) \Gamma\left(2\sqrt{2\pi}\ D2 \cosh(e\pi) \right);$$

#Declare and specify a lot of variables

$$A2 := alphaS + (1 + Ma)\,\eta;$$
$$A2bar := alphaS - (1 + Ma)\,\eta;$$
$$B2 := alphaL + (1 + Ma)\,\eta;$$
$$B2bar := alphaL - (1 + Ma)\,\eta;$$

$$e := \frac{1 \ln\left(\frac{1-\beta}{1+\beta} \right)}{2\pi};$$
$$\beta := \frac{h11}{\sqrt{h12\ h21}};$$

$$h11 := l11_1 - l11_2;$$
$$h12 := l12_1 + l12_2;$$
$$h21 := l21_1 + l21_2;$$

$$thetaL := \arctan(p \tan(\theta));$$
$$thetaS := \arctan(q \tan(\theta));$$

$$\eta := \sqrt{\frac{h21}{h12}};$$

$$rL := r\sqrt{\cos(\theta)^2 + p^2 \sin(\theta)^2};$$
$$rS := r\sqrt{\cos(\theta)^2 + q^2 \sin(\theta)^2};$$

$$p := \sqrt{B12 - \sqrt{B12^2 - K66}};$$
$$q := \sqrt{B12 + \sqrt{B12^2 - K66}};$$

$$B12 := \frac{1\left(2\,a12 + a66 + \rho\,c^2\left(a12^2 - a11\,a66 - a11\,a22\right)\right)}{2\,a11};$$
$$K66 := \frac{a22 + \rho\,c^2\left(a12^2 - a22\,a66 - a11\,a22 + \rho\,c^2\,a66\left(a11\,a22 - a12^2\right)\right)}{a11};$$

$$alphaL := p + \frac{a22\,\rho\,c^2}{p} - p\,\rho\,c^2\,a11 - \frac{\rho^2\,c^4\left(a11\,a22 - a12^2\right)}{p};$$
$$alphaS := q + \frac{a22\,\rho\,c^2}{q} - q\,\rho\,c^2\,a11 - \frac{\rho^2\,c^4\left(a11\,a22 - a12^2\right)}{q};$$

$$Ma := \rho\,c^2\,(a12 - a11);$$
$$Mb := \rho\,c^2\,(a12 - a22);$$

$$l11_1 := \frac{qS - qL}{alphaS - alphaL};$$
$$l12_1 := \frac{(1 + Ma)\,(pL - pS)}{D2};$$
$$l21_1 := \frac{alphaS\,qL - alphaL\,qS}{D2};$$
$$l11_2 := \frac{qS - qL}{alphaS - alphaL};$$
$$l21_2 := \frac{alphaS\,qL - alphaL\,qS}{D2};$$
$$l12_2 := \frac{(1 + Ma)\,(pL - pS)}{D2};$$

$$qS := \frac{a12\left(Mb - q^2\right) + a22\,(1 + Ma)}{q};$$
$$qL := \frac{a12\left(Mb - p^2\right) + a22\,(1 + Ma)}{p};$$

$$pS := a11\left(Mb - q^2\right) + a12\,(1 + Ma);$$
$$pL := a11\left(Mb - p^2\right) + a12\,(1 + Ma);$$

$$D2 := (1 + Ma)\,(alphaS - alphaL);$$

$$a11 := \frac{\cos(\alpha)^4}{EL} + \frac{\sin(\alpha)^4}{ET};$$
$$a12 := -\frac{nuLT}{EL};$$

$$a66 := \frac{1}{\mu LT};$$

$$a22 := \frac{\cos(\alpha)^4}{ET} + \frac{\sin(\alpha)^4}{EL};$$

$$\rho := 1100;$$

$$cL := 700;$$

$$cS := 300;$$

$$c := 20;$$

$$\rho 2 := 1001;$$

$$\rho 1 := 1001;$$

$$nuLT := 0.49;$$

$$\nu := 0.26;$$

$$\mu LT := 2.10000000\,10^9;$$

$$\mu 2 := 2.100000000\,10^9;$$

$$\mu := 2.100000000\,10^9;$$

$$EL := 9.652613305\,10^9;$$

$$ET := 9.652613305\,10^9;$$

$$h := d;$$

$$d := 0.006350;$$

#Sampson's stress-optic law:

$$g := evalf\left(\left(\frac{\sigma_{ySIM}}{f1} - \frac{\sigma_{xSIM}}{f2}\right)^2 + \left(\frac{2\,\tau_{xySIM}}{f12}\right)^2 - \frac{NT^2}{h^2}\right);$$

$$parK01 := diff(g, K0[1]);$$

$$parKstar1 := diff(g, Kstar[1]);$$

$$gFunc := unapply(evalf(g), K0[1], Kstar[1], r, \text{theta}, NT);$$

$$mk01 := unapply((parK01), K0[1], Kstar[1], r, \text{theta});$$

$$mkstar1 := unapply((parKstar1), K0[1], Kstar[1], r, \text{theta});$$

$C := Matrix(numdata, 2);$
$gmat := Matrix(numdata, 1);$
$coef := Matrix(numit + 1, 3);$
$DIFFERENCE := Matrix(3, 1);$
$difference := Matrix(numit, 3);$

#State initial guesses for the coefficients

$coef[1, 2] := 1e6;$
$coef[1, 3] := 1e5;$

for i **from** 1 **to** $numit$ **do**
$difference_{i,1} := 1;$
$coef_{i,1} := 1;$
for j **to** $numdata$ **do**
$gmat_{j,1} := evalf(-gFunc(coef_{i,2}, coef_{i,3}, data_{j,1}, data_{j,2}, data_{j,3}));$
$C_{j,1} := evalf(mk01(coef_{i,2}, coef_{i,3}, data_{j,1}, data_{j,2}));$
$C_{j,2} := evalf(mkstar1(coef_{i,2}, coef_{i,3}, data_{j,1}, data_{j,2}));$
end do;
$ctran := evalf(Transpose(C));$
$dee := evalf(MatrixMatrixMultiply(ctran, C));$
$deeInv := evalf(MatrixInverse(dee));$
$deeInvC := evalf(MatrixMatrixMultiply(deeInv, ctran));$
$DIFFERENCE := evalf(MatrixMatrixMultiply(deeInvC, gmat));$
for k **from** 2 **to** 3 **do**
$difference_{i,k} := DIFFERENCE_{k-1,1};$
$coef_{i+1,k} := evalf(coef_{i,k} + DIFFERENCE_{k-1,1})$
end do
end do;

$K0_1 := coef[21, 2];$
$Kstar_1 := coef[21, 3];$

#Check for convergence
if $\left(0.98 \le \frac{coef[21, 2]}{coef[20, 2]} < 1.02\right)$ **then** $Converg := True$
else $Converg := False$
end if;

$$EnergyReleaseRate := \frac{\left((K0_1)^2 + (Kstar_1)^2\right) \cdot h21}{(4 \cdot \cosh(\text{epsilon} \cdot \pi))^2};$$

```
#Now generate image matrix

Nplot := sqrt(evalf((((sigma_ySIM/f1 - sigma_xSIM/f2)^2 + (2*tau_xySIM/f12)^2)*h^2));

Nplo2 := unapply(evalf(Nplot), r, theta);

picwidth := 100;
picheight := 100;

Digits := 20#MathCad is only able to import matrix files with digits = 10
WidthParam := picwidth/2;
HeightParam := picheight/2;

replo := Matrix(picheight, picwidth):

for aa from 1 to picheight do
for bb from 1 to picwidth do
wpar := (bb - WidthParam)/(ScaleFactor*picwidth);
hpar := (HeightParam - aa)/(ScaleFactor*picheight);

if wpar <> 0 then
if hpar <> 0 then

r := sqrt(wpar^2 + hpar^2);
theta := arctan(hpar/wpar);
replo[bb, aa] := evalf(Nplo2(r, theta));

else
replo[bb, aa] := 0#Simply assigns a zero order to singularities
end if
end if
od:
od:

ResultsNum := nprintf("2TRESULT xoffset=%g yoffset=%g spec=%a Quad%g", xOffset, yOffset, SpecName,
Quadrant);
stuff := fopen(ResultsNum, WRITE);
fprintf(stuff, "xOffset=%g yOffset=%g K01=%e Kstar1=%e EnergyReleaseRate=%g Conv=%a", xOffset, yOffset,
K0_1, Kstar_1, EnergyReleaseRate, Converg);
fclose(stuff);
```

This code segment generates the file that keeps a running tab of the calculation results for each offset.

This segment appends the information to the file for each offset step calculation

```
ResultsCumul := nprintf("2TCMLRESULT  spec=%a Quad%g", SpecName, Quadrant);
stuffcumul := fopen(ResultsCumul, APPEND);
fprintf(stuffcumul, "xOffset=%g yOffset=%g K01=%e Kstar1=%e EnergyReleaseRate=%g Converg=%a \n", xOffset,
yOffset, K0_1, Kstar_1, EnergyReleaseRate, Converg);
fclose(stuffcumul);


ResultMatr := nprintf("2TNMAT xoff=%g yoff=%g conv=%a spec=%a quad%a", xOffset, yOffset, Converg,
SpecName, Quadrant );
ExportMatrix(ResultMatr, replo, target = delimited, delimiter = ",");


#Image generation procedure

-

_ResultPicName := sprintf("2TRIMG  xoff=%g yoff=%g conv=%a spec=%a Quad%g .bmp", xOffset, yOffset,
Converg, SpecName, Quadrant);


WordMatrix := Matrix(picheight, picwidth) :
BitMatrix := Matrix(picheight, picwidth) :

WordMatrix := Matrix(picheight, picwidth) :
BitMatrix := Matrix(picheight, picwidth) :
```

for qq **from** 1 **to** $picheight$ **do**
  for rr **from** 1 **to** $picwidth$ **do**

  if $\left(\left(\frac{9}{10}\right) < \text{frac}(replo[rr, qq]) \leq 1\right)$ **then** $WordMatrix[rr, qq] := BLK$
  elif $\left(\left(\frac{8}{10}\right) < \text{frac}(replo[rr, qq]) \leq \left(\frac{9}{10}\right)\right)$ **then** $WordMatrix[rr, qq] := DKGY$
  elif $\left(\left(\frac{7}{10}\right) < \text{frac}(replo[rr, qq]) \leq \left(\frac{8}{10}\right)\right)$ **then** $WordMatrix[rr, qq] := MDGY$
  elif $\left(\left(\frac{6}{10}\right) < \text{frac}(replo[rr, qq]) \leq \left(\frac{7}{10}\right)\right)$ **then** $WordMatrix[rr, qq] := LTGY$
  elif $\left(\left(\frac{4}{10}\right) < \text{frac}(replo[rr, qq]) \leq \left(\frac{6}{10}\right)\right)$ **then** $WordMatrix[rr, qq] := WHT$
  elif $\left(\left(\frac{3}{10}\right) < \text{frac}(replo[rr, qq]) \leq \left(\frac{4}{10}\right)\right)$ **then** $WordMatrix[rr, qq] := LTGY$
  elif $\left(\left(\frac{2}{10}\right) < \text{frac}(replo[rr, qq]) \leq \left(\frac{3}{10}\right)\right)$ **then** $WordMatrix[rr, qq] := MDGY$
  elif $\left(\left(\frac{1}{10}\right) < \text{frac}(replo[rr, qq]) \leq \left(\frac{2}{10}\right)\right)$ **then** $WordMatrix[rr, qq] := DKGY$
  elif $\left((0) < \text{frac}(replo[rr, qq]) \leq \left(\frac{1}{10}\right)\right)$ **then** $WordMatrix[rr, qq] := BLK$

  end if;

  end do;
 end do;

for $qqqq$ **from** 1 **to** $picheight$ **do**
for $rrrr$ **from** 1 **to** $picwidth$ **do**

if $WordMatrix[rrrr, qqqq] = BLK$ **then** $BitMatrix[rrrr, qqqq] := 0$
elif $WordMatrix[rrrr, qqqq] = DKGY$ **then** $BitMatrix[rrrr, qqqq] := \frac{64}{255}$
elif $WordMatrix[rrrr, qqqq] = MDGY$ **then** $BitMatrix[rrrr, qqqq] := \frac{127}{255}$
elif $WordMatrix[rrrr, qqqq] = LTGY$ **then** $BitMatrix[rrrr, qqqq] := \frac{191}{255}$
elif $WordMatrix[rrrr, qqqq] = WHT$ **then** $BitMatrix[rrrr, qqqq] := \frac{255}{255}$
end if

 end do;
end do;

#Write image to file

$ResultBitmap := ImageTools[Create](picheight, picwidth, BitMatrix)$;

$ImageTools[Write](ResultPicName, ResultBitmap, format = BMP)$;

#Clear previously calculated values for the following, they must be declared afresh for each iteration

```
unassign('σxSUM');
unassign('σySUM');
unassign('τxySUM');
unassign('g');
unassign('gFunc');
unassign('Nplot');
unassign('Nplo2');

unassign('K0[1]');
unassign('K0[3]');
unassign('Kstar[1]');
unassign('Kstar[3]');
unassign('theta');
unassign('r');

unassign('parK01');
unassign('parKstar1');

unassign('mk01');
unassign('mkstar1');

unassign('A2');
unassign('A2bar');
unassign('B2');
unassign('B2bar');

unassign('e');
unassign('β');

unassign('h11');
unassign('h12');
unassign('h21');

unassign('thetaL');
unassign('thetaS');

unassign('η');

unassign('rL');
unassign('rS');

unassign('p');
unassign('q');
```

```
unassign('B12');
unassign('K66');

unassign('alphaL');
unassign('alphaS');

unassign('Ma');
unassign('Mb');

unassign('l11_1');
unassign('l12_1');
unassign('l21_1');
unassign('l11_2');
unassign('l12_2');
unassign('l21_2');

unassign('qS');
unassign('qL');

unassign('pS');
unassign('pL');

unassign('D2');

unassign('a11');
unassign('a12');
unassign('a66');
unassign('a22');

Digits := 30:#Set digits back to 30, otherwise program malfunction

end do;
end do;
```

End of worksheet.

APPENDIX C

MathCad Worksheet for False-Color Fringe Multiplication

#Begin worksheet

$M_{no_load} := READ_IMAGE("C:\allblack.bmp")$

$M_{loaded} := READ_IMAGE("angledttFeb2009_both090_30degA__600lbs_24bit.bmp")$

$number_cols := cols(M_{loaded})$ $number_cols = ▮$

$number_rows := rows(M_{loaded})$ $number_rows = ▮$

$i := 0, 1 .. (number_rows - 1)$

$j := 0, 1 .. (number_cols - 1)$

$M_{no_loadNorm} := \frac{M_{no_load} + 1}{max(M_{no_load}) + 1}$ $M_{loadedNorm} := \frac{M_{loaded} + 1}{max(M_{loaded}) + 1}$

$max(M_{no_loadNorm}) = ▮$ $max(M_{loadedNorm}) = ▮$

$mean(M_{no_loadNorm}) = ▮$ $mean(M_{loadedNorm}) = ▮$

$NormImg_{i,j} := \frac{M_{loaded_{i,j}} + 1}{M_{no_load_{i,j}} + 1}$ $N_{max} := max(NormImg)$ $N_{max} = ▮$

$N_{min} := min(NormImg)$ $N_{min} = ▮$

$mean(NormImg) = ▮$

Do not always use equalization

$M_{equalized} := equalize(M_{loaded})$

$WRITEBMP("w30_aw033_090_090\COLORMULT\Equalized.bmp") := M_{equalized}$

$$HC_{smoothing5} := \begin{pmatrix} 2 & 1 & 1 & 1 & 2 & 2 & 1 & 1 & 1 & 2 \\ 1 & 2 & 1 & 1 & 2 & 2 & 1 & 1 & 2 & 1 \\ 1 & 1 & 2 & 1 & 2 & 2 & 1 & 2 & 1 & 1 \\ 1 & 1 & 1 & 2 & 2 & 2 & 2 & 1 & 1 & 1 \\ 1 & 1 & 1 & 1 & 4 & 4 & 1 & 1 & 1 & 1 \\ 1 & 1 & 1 & 1 & 4 & 4 & 1 & 1 & 1 & 1 \\ 1 & 1 & 1 & 2 & 2 & 2 & 2 & 1 & 1 & 1 \\ 1 & 1 & 2 & 1 & 2 & 2 & 1 & 2 & 1 & 1 \\ 1 & 2 & 1 & 1 & 2 & 2 & 1 & 1 & 2 & 1 \\ 2 & 1 & 1 & 1 & 2 & 2 & 1 & 1 & 1 & 2 \end{pmatrix}$$

$i_limit := cols(HC_{smoothing5}) - 1 \quad i_limit =$ ▮

$j_limit := rows(HC_{smoothing5}) - 1 \quad j_limit =$ ▮

$$sumHC5 := \sum_{i=0}^{i_limit} \sum_{j=0}^{j_limit} HC_{smoothing5_{i,j}}$$

$sumHC5 =$ ▮

The above sum is the sum of the values of each matrix element
Then the smoothing matrix is divided by this so that the smoothing matrix doesn't increase or decrease the overall intensity of the image.

$$HK_{smoothing5} := \frac{1}{sumHC5} \cdot HC_{smoothing5}$$

Here NOT using equalized image, using loaded image

$$HM_{custom_smoo} := convol2d(M_{loaded}, HK_{smoothing5})$$

$$NormImg_{i,j} := \frac{HM_{custom_smoo_{i,j}} + 1}{M_{no_load_{i,j}} + 1}$$

$N_{max} := max(NormImg)$

$N_{min} := min(NormImg)$

$M_{NormImg} := NormImg \cdot 255$

$mean(NormImg) =$ ▮ $\quad N_{max} =$ ▮

$N_{min} =$ ▮

WRITEBMP("CustomSmoothed.bmp") := HM_{custom_smoo}

WRITEBMP("NormImg.bmp") := $M_{NormImg}$

$$S_{i,j} := \frac{NormImg_{i,j} - N_{max}}{N_{max} - N_{min}} + 1$$

max(S) = ▮

min(S) = ▮

$S_{255} := S \cdot 255$

Smoothed and normalized:

WRITEBMP("SmoothAndNorm.bmp") := S_{255}

Bimat := S_{255}

Bimat = ▮

$$Red := \begin{pmatrix} 255 \\ 0 \\ 0 \end{pmatrix} \qquad Green := \begin{pmatrix} 0 \\ 255 \\ 0 \end{pmatrix} \qquad Blue := \begin{pmatrix} 0 \\ 0 \\ 255 \end{pmatrix}$$

MAXH := 211

I := 0.. 255

$Q_I := 255$ $V_I := 255$

$$H_I := \left| I \cdot \frac{MAXH}{255} - MAXH \right|$$

HQV := augment3(H, Q, V)^T

rows(HQV) = ▮

cols(HQV) = ▮

$RGB^{\langle I \rangle} := hsv_to_rgb\left(HQV^{\langle I \rangle}\right)$

$x_I := I$ PAL := augment$\left(x, RGB^T\right)$

PAL =

Bimat_RGB := gray_to_rgb(Bimat, PAL)

WRITERGB("ColorMult.bmp") := Bimat_RGB

#End MathCad worksheet

APPENDIX D

Machining Parameters and Practical Tips for Machining The Transparent Composite

Band Saw

The recommended blade has a 32 teeth-per-inch pitch while the recommended blade speed is 125 feet per minute. Regular steel blades do work, but wear out somewhat quickly. It is important to note that when the blades become dull there is significant tearing of the composite along the cut. This necessitates extra machining passes.

Milling Machine:

The minimum specification for the milling bit is titanium nitride coated tungsten carbide (TiN – WC). Any lesser specification will wear out very quickly.
For cutting, a spindle speed of 1600-1800 rpm works well, while for milling holes a reduced spindle speed is recommended, 900 rpm works well. The maximum recommended feed rate is 1 inch per minute, at a maximum depth of 100 thousandths of an inch. This depth is only recommended as long as subsequent cuts are to be made. Any "finishing" cut should be at most 75 thousandths of an inch deep, preferably 50 thousandths or less. Higher feed rates will cause chipping, as will deeper cuts. If this occurs on the mating surface then the surface will have to be re-machined until no chipping is evident.

VITA

Marius Daniel Ellingsen was born May 19th, 1974, in Porsgrunn, Norway. He attended public schools in Norway, graduating Porsgrunn Videregående Skole high school in 1993. During his studies at Telemark College he transferred to the South Dakota School of Mines and Technology in Rapid City, SD, where he graduated with his B.Sc. in Mechanical Engineering in 2000. He started his M.Sc. under the supervision of Dr. Sanjeev K. Khanna that same year. In 2001 he transferred to the University of Missouri in Columbia, MO with Dr. Khanna who had obtained a faculty position at this university. Marius Ellingsen graduated his M.Sc. in 2002, and then enrolled in the Doctoral Program, still under the supervision of Dr. Khanna. He was named "Outstanding Graduate Student" in Mechanical and Aerospace Engineering in 2008.